

UNIVERSITY OF DUBLIN

DOCTORAL THESIS

---

# String breaking from Lattice QCD with $N_f=2+1$ dynamical fermions

---

*Author:*  
Vanessa Koch

*Academic advisor:*  
Dr. Michael Peardon

*A thesis submitted to  
the University of Dublin  
in fulfillment of  
the requirements for the degree of*

*Doctor of Philosophy*

School of Mathematics  
University of Dublin  
Trinity College

2019



**Trinity College Dublin**

Coláiste na Tríonóide, Baile Átha Cliath

The University of Dublin



## **Declaration of Authorship**

I declare that this thesis has not been submitted as an exercise for a degree at this or any other university and it is entirely my own work.

I agree to deposit this thesis in the University's open access institutional repository or allow the Library to do so on my behalf, subject to Irish Copyright Legislation and Trinity College Library conditions of use and acknowledgement.

Vanessa Koch

Dublin, January 24, 2019



*“Practical application is found by not looking for it, and one can say that the whole progress of civilization rests on that principle.”*

Jaques Hadamard



## Summary

In quantum chromodynamics (QCD), the static potential  $V(r)$  is defined as the energy of the ground state of the system containing a static quark and a static antiquark, separated by a distance  $r$ . As a consequence of confinement, the energy between the quark-antiquark pair is contained inside a color flux tube, the string. As soon as the energy is high enough, the gluonic string connecting the quarks breaks due to creation of a pair of light quarks, which recombine with the static quarks and form two static-light mesons. This so called string breaking provides an intuitive example of a strong decay and is one of the defining characteristics of a confining gauge theory with dynamical matter fields. Since it is a low energy phenomenon not accessible by perturbative QCD, it can only be examined by non-perturbative methods. We investigate string breaking using Lattice QCD, a well-established non-perturbative approach to solving QCD.

In the theory with dynamical quarks, string breaking is manifested as a quantum-mechanical mixing phenomenon. This means that the two states, the string state and the two meson state, are both needed to describe the potential. After the string is broken, the meson state dominates the new ground state of this system. In the neighborhood of the critical separation, the two states mix. If there is mixing, the ground state and first excited state are superpositions of the string state and the two meson state. The system undergoes an avoided level crossing, giving rise to an energy gap between the states.

So far, string breaking on the lattice has been observed in the  $N_f=2$  theory, but not for the  $N_f=2+1$  theory. In the latter case, when the strange quark is included in the sea, two separate thresholds are expected, one for the decay into two static-light mesons and one for the decay into two static-strange mesons.

In this work, the phenomenon is investigated with  $N_f=2+1$  flavors of non-perturbatively  $O(a)$ -improved dynamical Wilson fermions using an ensemble of gauge configurations generated through the Coordinated Lattice Simulations (CLS) effort. The ensemble has an estimated isotropic lattice spacing of  $a \approx 0.064\text{fm}$ , pion mass  $m_\pi = 280\text{MeV}$  and kaon mass  $m_K = 460\text{MeV}$ . We employ the stochastic LapH method in order to calculate correlation functions required for string breaking efficiently and perform a variational analysis to extract the ground state as well as the first and second excited state of the system containing two static quarks. A large set of off-axis distances is used in order to achieve the spatial

resolution needed to observe both mixing phenomena.

We see the effect of the strange quark, which results in a second mixing-phenomenon due to the formation of a strange-antistrange pair. Two avoided level crossings can be resolved clearly. We employ a simple model to define two distinct string breaking distances for the light and the strange mixing phenomenon.



## *Acknowledgements*

I wish to thank my supervisor Mike Peardon for his guidance, assistance and insight throughout the process of creating this thesis. My research would have been impossible without the aid and encouragement of him and Francesco Knechtli, who proposed the project in the first place and made it possible for me to continue working on it at the University of Wuppertal. He also provided invaluable help with cross checking and testing part of the code used for this work.

I am profoundly grateful to John Bulava and Ben Hörz. Not only for numerous illuminating discussions furthering the progress of this work, but especially for helping me find my way through the stochastic LapH codebase. I have learned a lot from Ben Hörz, who shared with me his programming knowledge and saved the day countless times with his support and positivity.

I extend my gratitude to Colin Morningstar for his hospitality during my short stay at Carnegie Mellon University in Pittsburg and some enlightening discussions at the early stages of this project.

I thank Graham Moir for useful advice in many instances and making me feel welcome during my first stays in Wuppertal.

I am grateful to Mike Peardon, Francesco Knechtli, John Bulava and Ben Hörz for valuable comments on an earlier version of this manuscript and I would especially like to thank Gunnar Bali and Alberto Ramos for the critical reading of a previous version.

Computations for this work were run at the Irish Centre for High-End Computing under project codes `tcpy068a` and `tcpy06b`, on the Seagull cluster maintained by the Research IT division in Trinity College Dublin and the Stromboli cluster at the University of Wuppertal. This work has received funding from the European Union's Horizon 2020 research and innovation programme under grant agreement Number 642069.



# Contents

<b>Declaration of Authorship</b>	<b>iii</b>
<b>Summary</b>	<b>v</b>
<b>Acknowledgements</b>	<b>iii</b>
<b>1 Introduction</b>	<b>1</b>
1.1 QCD: quarks, gluons and string breaking . . . . .	1
<b>2 Theoretical Background</b>	<b>5</b>
2.1 Lattice QCD . . . . .	5
2.1.1 Path integral . . . . .	5
2.1.2 Discrete Symmetries of the lattice theory and lattice action . . . . .	7
The fermionic part of the action . . . . .	9
The doubling problem and Wilson fermions . . . . .	9
The gluonic part of the action . . . . .	11
2.2 CLS ensembles . . . . .	12
Twisted mass reweighting . . . . .	14
Open boundary conditions . . . . .	15
<b>3 Methodology</b>	<b>17</b>
3.1 Correlation functions . . . . .	17
3.1.1 Symmetries . . . . .	20
3.2 Smearing . . . . .	21
3.2.1 Stout-link smearing . . . . .	21
3.2.2 HYP-smearing . . . . .	22
3.2.3 Distillation . . . . .	24
3.3 Stochastic LapH method . . . . .	26
Dilution . . . . .	27
3.4 Analysis techniques . . . . .	31
3.4.1 Extraction of energies . . . . .	31
3.4.2 Variational techniques and GEVP . . . . .	32

<b>4</b>	<b>String breaking</b>	<b>37</b>
4.1	A short history of string breaking . . . . .	37
4.2	Static quarks on the lattice . . . . .	39
4.2.1	Static propagator . . . . .	40
4.2.2	Renormalized static potential . . . . .	41
4.3	Symmetries of string breaking . . . . .	42
4.3.1	Interpolators . . . . .	43
4.4	First steps towards string breaking . . . . .	45
4.4.1	Static-light meson . . . . .	45
4.5	Correlation Matrix $C_{ij}$ . . . . .	47
4.5.1	Calculation of $C_{11}$ , Wilson-loop . . . . .	47
4.5.2	Calculation of $C_{22}$ . . . . .	48
4.5.3	Calculation of $C_{12}, C_{21}$ . . . . .	51
4.5.4	Including the strange quark . . . . .	51
<b>5</b>	<b>Numerical results for string breaking</b>	<b>53</b>
5.1	Ensemble details . . . . .	53
5.2	Static potential from Wilson loops . . . . .	54
5.3	Mixing analysis . . . . .	57
5.4	Model for the string breaking spectrum . . . . .	64
<b>6</b>	<b>Discussion and outlook</b>	<b>71</b>
	<b>Appendix</b>	<b>73</b>
A1	Gamma matrices . . . . .	73
A2	$t_{\min}$ -plots for all energy levels . . . . .	74

# Chapter 1

## Introduction

The major goal of physics is to find the "Theory of Everything", a hypothetical theory that should describe all physical aspects of the universe. This theory has to describe all elementary particles and fundamental forces between them. There is an ongoing effort to find candidates for such a theory [1]. The "Standard Model of particle physics" (SM) [2,3] emerged in the 1960s and 1970s and is a unification of three of the four known forces of nature: the weak, electromagnetic and the strong force. The SM describes all known fundamental interactions between elementary particles, except gravity. These interactions can be mathematically formulated by gauge theories and derive from one principle: the requirement for local gauge invariance.

The SM has continually provided experimental predictions and has met every experimental test so far [4]. With the discovery of the Higgs Boson in 2012 [5], the SM of particle physics was completed. It leaves some phenomena unexplained and does not include the theory of the gravitational force. This shows the need for an extension of the SM, but makes its complete overthrow unlikely.

Quantum chromodynamics (QCD) is the part of the SM describing the theory of strong interactions [3]. It details the interactions between quarks and gluons, which combine to form composite particles called hadrons. QCD exhibits very special characteristics, namely the phenomenon of confinement and dynamical chiral symmetry breaking [6]. The gauge group of QCD is the non-abelian symmetry group  $SU(3)$  and the name "Quantum chromodynamics" derives from the name for the charge in QCD, which is called color.

### 1.1 QCD: quarks, gluons and string breaking

In the SM, quarks are  $\text{spin-}\frac{1}{2}$  Dirac fermions with quark number 1, which is negative for antiquarks. The known six types of quarks, also called quark flavors, are listed in table 1.1. While the quark number of an isolated system is conserved, the different types of flavor can change via weak interactions. The heavy quarks are unstable and decay rapidly into

TABLE 1.1: Properties of quarks [3]

	Quark	Electric charge	Mass [MeV]
u	Up	$\frac{2}{3}$	1.5 - 4
d	Down	$-\frac{1}{3}$	4 - 8
c	Charm	$\frac{2}{3}$	1150 - 1350
s	Strange	$-\frac{1}{3}$	80 - 130
t	Top	$\frac{2}{3}$	169000 - 174000
b	Bottom	$-\frac{1}{3}$	4100 - 4400

up and down quarks and because of this, up and down quarks are the most common in nature. Strange, charm, bottom, and top quarks can only be produced in high energy collisions. Quarks, as well as gluons, possess a color charge which can take one of three values, colloquially called red, blue and green. An antiquark carries the corresponding anticolor while the gluon color charge is a mixture of two colors. Gluons are spin-1 massless vector gauge bosons and they mediate the strong force between quarks. A quark may emit or absorb a gluon, a gluon may emit or absorb a gluon, a gluon may turn into a pair of quark and anti-quark (and vice-versa), but also direct interaction between gluons is possible. The fact that the exchange particles of the strong force interact with each other is a special feature emerging due to the theory being non-abelian.

To date, quarks as well as gluons have never been observed isolated. The reason for this is that the quantum Yang–Mills theory for a non-abelian Lie group exhibits a property known as confinement. Because the gluon field is massless, one might expect the color force to be long range, but the fields are confining and the range of the strong force is effectively limited to a length scale of about 1fm. In the absence of confinement, one would expect to find massless gluons, but if they are confined, only color-neutral bound states of gluons can exist, so called glueballs [7]. Color-charged particles, such as quarks and gluons, can not be isolated and hence can not be observed directly. The analytic proof of this phenomenon is one of the seven Millennium Prize Problems defined by the Clay Mathematics Institute <sup>1</sup>. One important feature of a confining gauge theory with dynamical matter fields in the fundamental representation of the gauge group, and thus an important phenomenon to study in QCD, is the so called string breaking. String breaking describes the transition of the static quark-antiquark string into a static-light meson-antimeson system. It provides an intuitive example of a strong decay and is one of the defining characteristics of a confining gauge theory. When a quark-antiquark pair becomes separated, the color fields form a "string", or "color flux tube" between the quark and the antiquark. The energy of the system is confined inside the string binding the quarks and rises linearly until it becomes energetically more favorable to spontaneously create a quark-antiquark pair from the vacuum and thus break

<sup>1</sup>[www.claymath.org/sites/default/files/yangmills.pdf](http://www.claymath.org/sites/default/files/yangmills.pdf)

the string by forming new hadronic bound states.

Hadrons are composite particles built of quarks and antiquarks. In the SM, at least two types of hadrons can be classified. Mesons, made up of quark-antiquark pairs and baryons, made up of three quarks. Both states are color singlets. So called hybrid hadrons, which contain explicit valence gluon content, and exotic hadrons, which do not have the same quark content as ordinary hadrons, have also been theorized and candidates have been observed by multiple experiments, see for example [8–10].

Perturbation theory breaks down for distances close to the confinement length. Only at very short distances or high momenta, the effective strong coupling constant becomes small enough for quarks and gluons to be considered approximately asymptotically free, so that the interactions can be treated perturbatively. Since confinement is a low energy phenomenon, it is as such not accessible by perturbative QCD. It can only be examined by non-perturbative methods, for example numerical simulations, which show results compatible with confinement [11].

Because the low energy regime of QCD is not amenable to perturbative treatment, it is very difficult to predict or respectively postdict the hadron spectrum from first principles. Non-perturbative methods are needed to determine the low energy properties of QCD. The primary tool is lattice QCD, a well-established non-perturbative approach. Accordingly, one of the main goals of lattice QCD is to validate QCD as the correct theory of strong interactions by reproducing the experimentally measured spectrum of hadrons. Furthermore, it provides a framework for the investigation of other non-perturbative phenomena such as confinement.

In this thesis we study the phenomenon of string breaking using lattice QCD. The thesis is organized as follows. Chapter 2 is a brief introduction to the theoretical foundations of lattice QCD. The subsection on the CLS ensembles provides background about a set of gauge configurations that contains the ensemble used in this work. Chapter 3 focuses on the extraction of masses and energies of hadrons from Euclidean correlation functions. The stochastic LapH method is described, as well as solving the generalized eigenvalue problem, which can be used to extract excited states of the lattice QCD Hamiltonian.

In the beginning of Chapter 4, a short overview of string breaking in the literature is given, followed by a theoretical description of static quarks on the lattice and the symmetries of string breaking. The second part of chapter 4 is a detailed account of the full mixing analysis. In the final chapters, the numerical results are presented and discussed.





## Chapter 2

# Theoretical Background

### 2.1 Lattice QCD

In this section, some foundations and concepts of lattice QCD necessary to describe the following work are presented. It is not a thorough introduction or an in any way exhaustive review. Various sources were used to prepare this chapter, as well as chapter 3. For a more detailed introduction the reader is referred to the main sources [12–15].

Lattice QCD provides a well-established non-perturbative approach to solving QCD from first principles. There is ongoing progress of improving lattice techniques, especially for simulations with light dynamical fermions, see for example [16] and references therein.

Lattice gauge theory was introduced by Wilson in 1974, when he published a paper formulating gauge theories on a space-time lattice [17]. In general, lattice calculations are comprised of three main steps: the introduction of a finite space-time lattice as an UV regulator, the computation of the path integral of the discretized theory and finally the removal of the regulator in order to get the continuum result.

#### 2.1.1 Path integral

The starting point to putting a quantum field theory on the lattice is expressing the partition function of the Euclidian theory using the path integral formalism:

$$\mathcal{Z} = \int \mathcal{D}\Phi \exp(-S(\Phi)), \quad (2.1)$$

where  $S$  denotes the action and  $\Phi$  generically all fields of the theory. One typically introduces periodic boundary conditions in time for bosonic fields, while it is a natural choice to impose anti-periodic boundary conditions for fermionic fields, a thorough explanation is given in the appendix of [18].

Now it is possible to replace the continuous space-time by a  $4D$  Euclidian lattice which introduces a natural ultraviolet cut-off given by the inverse lattice spacing  $a^{-1}$ . There is more than one possible way to discretize space-time. One commonly used way is the isotropic hypercubic grid with lattice spacing  $a$  and size  $N_S^3 \times N_T$ . The degrees of freedom  $\Phi$  are now field variables living on the lattice. The Euclidian action  $S(\Phi)$  has to be discretized such that the continuum action is obtained for  $a \rightarrow 0$ . Restricting the integral to a finite spatial box with chosen boundary conditions provides an infrared cut-off by the inverse size of this box  $L^{-1}$ . By doing this, the previously infinite-dimensional path integral of the partition function becomes finite-dimensional, thus amenable to numerical simulations. The path integral still has to be performed over all field configurations. A suitable way to approximate the high-dimensional integral is given by Markov Chain Monte Carlo methods (MCMC) [19]. This makes the reason for using the Euclidian action apparent. In quantum mechanics, the path integral weight is given by  $\exp(iS_M)$ , where  $S_M$  is the action defined in Minkowski space-time. This would be unsuitable for applying Monte Carlo (MC) methods, because it is heavily oscillating. A Wick rotation to imaginary time  $t \rightarrow -i\tau$  leads to path integrals containing a positive weight, manageable using MC methods. The Euclidean action  $S$  is related to the Minkowski action  $S_M$  via  $S_M = iS$ . For QCD, a gauge theory with fermions, the partition function takes the form

$$\mathcal{Z} = \int \mathcal{D}[U, \psi, \bar{\psi}] e^{(-S_F[U, \psi, \bar{\psi}] - S_G[U])}, \quad (2.2)$$

where  $\psi$  are the quark fields,  $U$  are the gauge fields,  $S_F$  and  $S_G$  are the fermion and gauge action. The expectation values of observables are given by

$$\langle \mathcal{O} \rangle \equiv \frac{1}{\mathcal{Z}} \int \mathcal{D}[U, \psi, \bar{\psi}] \mathcal{O}[U, \psi, \bar{\psi}] e^{-S_F[U, \psi, \bar{\psi}] - S_G[U]}. \quad (2.3)$$

The generic observable  $\mathcal{O}$  is a functional of the fermion fields  $\psi, \bar{\psi}$  and the gauge fields  $U$ . Observables are calculated for each gauge field configuration, weighted with the exponent of the negative action and then integrated over all possible field configurations; configurations with minimal action contribute most to the path integral.

The integration over the fermion fields  $\psi$  and  $\bar{\psi}$  in the path integral can be performed analytically using rules for Gaussian integrals with Grassmann numbers. After integrating out the fermion fields in equation (2.3) one finds

$$\langle \mathcal{O} \rangle = \frac{1}{\mathcal{Z}} \int \mathcal{D}[U] \det[D[U]] \mathcal{O}[U] e^{-S_G[U]}. \quad (2.4)$$

The determinant depends on the gauge fields  $U$ . The observable  $\mathcal{O}[U]$  can depend on the

gauge field  $U$  explicitly, for example in case of purely gluonic observables, but also implicitly via the quark propagator  $D^{-1}[U]$  in the gauge background. The determinant gives rise to virtual fermion or "sea quark" effects. Ignoring this factor results in the so called quenched approximation. Even though the integral now only has to be taken over the gauge fields, this is still not feasible analytically but can be performed numerically. These expressions are usually approximated using Monte Carlo (MC) methods with importance sampling.

Another numerical challenge is the evaluation of the propagator  $D^{-1}[U]$ , the inverse of the large, sparse Dirac matrix, that appears in the fermionic part of the action. The calculation of all elements of the inverse is only possible on very small lattices. Therefore, one typically only computes the solution vectors  $u$  of the linear system of equations  $D[U]u = b$  for a handful of source vectors  $b$  using for example a variant of the conjugate gradient method. In some cases, it is necessary to evaluate quark propagators from all spatial sites on a time slice to all spatial sites on another time slice. This is the case for the string breaking calculation. It is then necessary to use methods that allow for all-to-all propagation, which is discussed in the next chapter.

By using the path integral formulation, it becomes possible to numerically evaluate correlation functions and afterwards use it to extract matrix elements of operators and thus the energy spectrum of the theory, for details see Chapter 3.

### 2.1.2 Discrete Symmetries of the lattice theory and lattice action

The path integral (2.4) has to be performed over all field configurations. To render it well-defined, it is regulated on a finite spacetime lattice given by

$$x \equiv x_\mu = n_\mu a, \quad n_\mu \in \{0, \dots, N_\mu - 1\}, \quad (2.5)$$

where  $a$  is the lattice spacing, which is the same for every direction. Using an isotropic lattice spacing is the most common case, although it is possible and for some calculations useful [20] or even necessary [21] to use an anisotropic lattice spacing.

The next step in the discretization of QCD is the lattice description of the field variables. The fermionic field is represented by anticommuting Grassmann variables defined at each site of the lattice. The spinors  $\psi(x), \bar{\psi}(x)$ , where now  $x = n_\mu a$ , carry the same color, Dirac and flavor indices as in the continuum.

It is possible to associate each link with a discrete version of the path ordered product

$$U(x, x + \hat{\mu}) \equiv U_\mu(x) = e^{iagA_\mu(x + \frac{\hat{\mu}}{2})}, \quad (2.6)$$

TABLE 2.1: The behavior of the gauge and fermion degrees of freedom under the discrete transformations  $\mathcal{P}, \mathcal{C}, \mathcal{T}$ . [12]

	$\mathcal{P}$	$\mathcal{C}$	$\mathcal{T}$
$U_4(\vec{x}, \tau)$	$U_4(-\vec{x}, \tau)$	$U_4^*(\vec{x}, \tau)$	$U_{-4}(\vec{x}, -\tau)$
$U_i(\vec{x}, \tau)$	$U_{-i}(-\vec{x}, \tau)$	$U_i^*(\vec{x}, \tau)$	$U_i(\vec{x}, -\tau)$
$\psi(\vec{x}, \tau)$	$\gamma_4\psi(-\vec{x}, \tau)$	$\mathcal{C}\bar{\psi}^T(\vec{x}, \tau)$	$\gamma_4\gamma_5\psi(\vec{x}, -\tau)$
$\bar{\psi}(\vec{x}, \tau)$	$\bar{\psi}(-\vec{x}, \tau)\gamma_4$	$-\psi^T(\vec{x}, \tau)\mathcal{C}^{-1}$	$\bar{\psi}(\vec{x}, -\tau)\gamma_5\gamma_4$

where the average field  $A_\mu$  is an algebra-valued lattice gauge field. It is defined at the midpoint of the link, and  $U$  is a  $3 \times 3$  unitary matrix with unit determinant. These are the fundamental variables which are integrated over in the path integral. The link matrices  $U$  are chosen to belong to the same representation of color  $SU(3)$  as the fermions, which are in the fundamental representation. Note that in the continuum, the gluon fields are elements of the Lie algebra, not the gauge group. These matrix valued variables are oriented. It is possible to define link variables pointing in negative direction, but they are not independent and related to the positively oriented links according to

$$U(x, x - \hat{\mu}) \equiv U_{-\mu}(x) = e^{-iagA_\mu(x - \frac{\hat{\mu}}{2})} = U^\dagger(x - \hat{\mu}, x) = U_\mu^\dagger(x - \hat{\mu}). \quad (2.7)$$

On the lattice, the rotation group of the continuum theory is reduced to a discrete group. On a hypercubic lattice only rotations in steps of  $90^\circ$  are possible, so the continuous rotation group is replaced by the discrete hypercubic group [22]. In this case, the allowed momenta are discrete and take the following values:

$$k = \frac{2\pi n}{N_s} \quad n = 0, 1, \dots, N_s. \quad (2.8)$$

Additionally, the lattice action is invariant under parity ( $\mathcal{P}$ ), charge conjugation ( $\mathcal{C}$ ) and time reversal ( $\mathcal{T}$ ). The behavior of the field variables under the discrete symmetries is provided in table 2.1. The gamma matrix conventions used in this work are given in Appendix A1.

The lattice action also has to be invariant under the local gauge symmetry. For a local gauge transformation  $\Omega(x)$ , where  $\Omega$  is an element of  $SU(3)$  on each lattice site, the fermion fields  $\psi(x)$  and gauge fields  $U$  transform according to

$$\psi(x) \rightarrow \psi'(x) = \Omega(x)\psi(x) \quad (2.9)$$

$$\bar{\psi}(x) \rightarrow \bar{\psi}'(x) = \bar{\psi}(x)\Omega^\dagger(x) \quad (2.10)$$

$$U_\mu(x) \rightarrow U_\mu(x)' = \Omega(x)U_\mu(x)\Omega^\dagger(x + \hat{\mu}). \quad (2.11)$$

### The fermionic part of the action

In the continuum, the fermionic action is given by:

$$S_F^c[\psi, \bar{\psi}] = \int d^4x \bar{\psi}(x)(\not{D} + m)\psi, \quad (2.12)$$

where  $D$  is the covariant derivative, the Feynman slash notation was used  $\not{D} = \gamma_\mu D^\mu$ . To discretize the action, not only the path integral needs to be discretized, but the derivatives also need to be replaced with a discretized version. Using the symmetrized difference, one finds for the free lattice fermion action

$$S_F^f[\psi, \bar{\psi}] = a^4 \sum_x \bar{\psi}(x) \left( \sum_{\mu=1}^4 \gamma_\mu \frac{\psi(x + \hat{\mu}) - \psi(x - \hat{\mu})}{2a} + m\psi(x) \right). \quad (2.13)$$

The discretized derivative is not gauge invariant. To see this, consider for instance the following term

$$\bar{\psi}(x)\psi(x + \hat{\mu}) \rightarrow \bar{\psi}'(x)\psi'(x + \hat{\mu}) = \bar{\psi}(x)\Omega^\dagger(x)\Omega(x + \hat{\mu})\psi(x + \hat{\mu}). \quad (2.14)$$

Using a gauge field  $U_\mu(x)$ , which transforms according to equation (2.11), a corresponding gauge invariant term  $\bar{\psi}(x)U_\mu(x)\psi(x + \hat{\mu})$  can be constructed

$$\begin{aligned} \bar{\psi}'(x)U_\mu(x)\psi'(x + \hat{\mu}) &= \bar{\psi}(x)\Omega^\dagger(x)U'_\mu(x)\Omega(x + \hat{\mu})\psi(x + \hat{\mu}) \\ &= \bar{\psi}(x)\Omega^\dagger(x)\Omega(x)U_\mu(x)\Omega^\dagger(x + \hat{\mu})\Omega(x + \hat{\mu})\psi(x + \hat{\mu}) \\ &= \bar{\psi}(x)U_\mu(x)\psi(x + \hat{\mu}) \end{aligned} \quad (2.15)$$

The gauge invariant, so called *naive fermion action* can now be defined as:

$$S_F^n[\psi, \bar{\psi}, U] = a^4 \sum_x \bar{\psi}(x) \left( \sum_{\mu=1}^4 \gamma_\mu \frac{U_\mu(x)\psi(x + \hat{\mu}) - U_{-\mu}(x)\psi(x - \hat{\mu})}{2a} + m\psi(x) \right). \quad (2.16)$$

### The doubling problem and Wilson fermions

A problem arising from the naive discretization of the Dirac action as described above is that in the continuum limit, it gives rise to  $2^d = 16$  flavors rather than one. The action for one flavor is bilinear in  $\bar{\psi}$  and  $\psi$ , so it can be rewritten in the following form

$$S_F^n[\psi, \bar{\psi}, U] = a^4 \sum_{x,y} \sum_{a,b,\alpha,\beta} \bar{\psi}(x)_a^\alpha D(x|y)_{ab}^{\alpha\beta} \psi(y)_b^\beta, \quad (2.17)$$

where  $a, b$  are color and  $\alpha, \beta$  are Dirac indices. The corresponding naive Dirac operator amounts to

$$D(x | y)_{ab}^{\alpha\beta} = \sum_{\mu=1}^4 (\gamma_{\mu})_{\alpha\beta} \frac{U_{\mu}^{ab}(x)\delta(x + \hat{\mu}, y) - U_{-\mu}^{ab}(x)\delta(x - \hat{\mu}, y)}{2a} + m\delta_{\alpha\beta}\delta_{ab}\delta_{x,y}. \quad (2.18)$$

The Fourier transform of the free Dirac operator

$$\tilde{D}(p | q) = \delta(p - q)\tilde{D}(p), \quad (2.19)$$

is diagonal in the momenta. Thus using the Fourier transform of the free lattice Dirac operator in momentum space

$$\tilde{D}(p) = m\mathbf{1} + \frac{i}{a} \sum_{\mu} \gamma_{\mu} \sin(p_{\mu}a), \quad (2.20)$$

the inverse of  $D(x | y)$  can be calculated. It is sufficient to work out the inverse of the  $4 \times 4$  matrix  $\tilde{D}(p)$  and then invert the Fourier transform, but it is actually more instructive to look at the momentum space propagator. In the case of massless fermions, it is given by [14]

$$\tilde{D}(p)^{-1} |_{m=0} = \frac{-ia^{-1} \sum_{\mu} \gamma_{\mu} \sin(p_{\mu}a)}{a^{-2} \sum_{\mu} \sin^2(p_{\mu}a)}. \quad (2.21)$$

For fixed momentum, this has the correct continuum limit. In the continuum, the massless fermion propagator has one pole at  $p = (0, 0, 0, 0)$  that corresponds to the fermion described by the Dirac operator. On the lattice, however, there are additional poles, every time all components are 0 or  $\pi/a$

$$p = (\pi/a, 0, 0, 0), (0, \pi/a, 0, 0), \dots, (\pi/a, \pi/a, \pi/a, \pi/a). \quad (2.22)$$

This amounts to 15 unwanted poles, so called fermion doublers. There are ways to remove the doublers, but there is always a sacrifice. The no-go theorem by Nielsen-Ninomiya [23] states that it is not possible to define a local, translationally invariant lattice action that preserves chiral symmetry and does not have doublers. Only by violating one of the presuppositions of the theorem is it possible to get rid of the doublers. One possible solution to removing the unwanted doublers was suggested by Wilson [17], the so called Wilson fermions. The idea is to add an extra term in the naive action (2.16) that decouples the doublers in the continuum limit. The Wilson action for QCD with  $N_f$  degenerate quark flavors

is given by

$$S_F^W[\psi, \bar{\psi}, U] = a^4 \sum_{f=1}^{N_f} \sum_x \bar{\psi}_f(x) \left( \sum_{\mu=1}^4 \gamma_\mu \frac{U_\mu(x)\psi_f(x + \hat{\mu}) - U_{-\mu}(x)\psi_f(x - \hat{\mu})}{2a} \right) \quad (2.23)$$

$$\begin{aligned} & - \frac{U_\mu(x)\psi_f(x + \hat{\mu}) - 2\psi_f(x) + U_{-\mu}(x)\psi_f(x - \hat{\mu})}{2a} + m\psi_f(x) \Big) \\ & = a^4 \sum_{f=1}^{N_f} \sum_x \bar{\psi}_f(x) (D_W + m)\psi_f(x), \end{aligned} \quad (2.24)$$

where  $D_W$  denotes the Wilson-Dirac operator. The extra term is proportional to the discretized Laplace operator. Since the additional Laplacian term does not anticommute with  $\gamma_5$ , this explicitly violates chiral symmetry, violating one characteristic of the theory, as is required by the Nielsen-Ninomiya theorem. But the term does commute with  $\gamma_5$ , so that the Wilson Dirac operator obeys  $\gamma_5$ -hermiticity, which implies

$$\gamma_5 D^W = (\gamma_5 D^W)^\dagger \quad (2.25)$$

is hermitian. The extra fifteen species get a mass proportional to  $2/a$ , as can be seen in momentum space. The free Dirac operator (2.20) in momentum space reads

$$\tilde{D}^W(p) = m\mathbf{1} + \frac{i}{a} \sum_\mu \gamma_\mu \sin(p_\mu a) + \mathbf{1} \frac{1}{a} \sum_\mu (1 - \cos(p_\mu a)). \quad (2.26)$$

For zero momentum the term vanishes. If  $p_\mu = \pi/a$  an extra term  $2/a$  is added to the operator so that the mass term of the doublers is given by  $m + \frac{2n}{a}$ , where  $n$  counts the number of components equal to  $\pi/a$ . The extra term goes to infinity in the continuum limit, the doublers become very heavy and are effectively removed from the spectrum. This means all unwanted poles are no longer present in the corresponding propagator  $\tilde{D}(p)^{-1}$ .

### The gluonic part of the action

The link variables are the quantities used for putting the gluon fields on the lattice and the gauge action has to be constructed in terms of them. In order to do this, gauge invariant objects built from the link variables are needed. It is possible to construct two types of gauge invariant objects according to the transformation properties of the fields (2.9) - (2.11).

A path-ordered product of  $k$  link variables

$$\mathcal{C}(U, x_0, x_1) = U_{\mu_0}(x_0)U_{\mu_1}(x_0 + \hat{\mu}_0) \dots U_{\mu_{k-1}}(x_1 - \hat{\mu}_{k-1}) \equiv \prod_{(x,\mu) \in \mathbf{C}_{x_0 x_1}} U_\mu(x), \quad (2.27)$$

is connecting  $x_0$  and  $x_1$  along some path  $\mathbf{C}_{x_0x_1}$ . It is the lattice version of the continuum gauge transporter and called Wilson-line. A Wilson-line is gauge-covariant, because the two transformation matrices  $\Omega(x)$  and  $\Omega^\dagger(x)$  cancel each other at every point  $x$ , only the matrices at the end and start point remain. A gauge invariant object can now be constructed with a fermion and an antifermion attached at the starting and end point

$$\mathcal{M}(x_0, x_1) = \bar{\psi}(x_0) \prod_{(x,\mu) \in \mathbf{C}_{x_0x_1}} U_\mu(x) \psi(x_1). \quad (2.28)$$

Another way to construct a gauge invariant quantity from the path-ordered product is closing the path by forming a loop and taking the trace. The loop is given by

$$\mathcal{L}[U] = \text{Tr} \left( \prod_{(x,\mu) \in \mathbf{L}} U_\mu(x) \right), \quad (2.29)$$

where the transformation matrices at the start and end point now cancel when the trace is taken. Those loops and products of link variables are the gauge invariant objects that can be used for constructing the gluon action. The action for the lattice is written in such a way that the limit  $a \rightarrow 0$  formally reproduces the original continuum action. However, the formulation is not unique and can differ in cut-off effects, depending on which loops or products of links are used. Complicated loops can be employed to construct improved actions, this way it is possible to reduce lattice artifacts and improve scaling towards the continuum.

The simplest example of a loop is the so called plaquette, a  $1 \times 1$  loop,

$$\mathcal{U}_{\mu\nu} = \text{Re Tr}(U_\mu(x) U_\nu(x + \hat{\mu}) U_\mu^\dagger(x + \hat{\nu}) U_\nu^\dagger(x)) . \quad (2.30)$$

Wilson's original form of the gauge action is a sum over all plaquettes, where each plaquette  $p$  is counted with one orientation

$$S_G[U] = \frac{6}{g_0^2} \sum_x \sum_{\mu < \nu} \text{Re Tr} \frac{1}{3} (1 - \mathcal{U}_{\mu\nu}) = \frac{2}{g_0^2} \sum_p \text{Tr}(1 - U(p)) , \quad (2.31)$$

where  $g_0$  is the bare gauge coupling.

## 2.2 CLS ensembles

This section outlines the most important characteristics of a set of gauge configurations generated by the Coordinated Lattice Simulations (CLS) effort [24]. One of the ensembles, the



$N_{200}$ , is used in this work.

The CLS ensembles have  $N_f = 2+1$  flavors of non-perturbatively improved Wilson fermions [25], where the action is given by

$$S[\psi, \bar{\psi}, U] = S_F^W[\psi, \bar{\psi}, U] + c_{sw} a^5 \sum_x \sum_{\mu < \nu} \bar{\psi}(x) \frac{1}{2} \sigma_{\mu\nu} \hat{F}_{\mu\nu}(x) \psi(x) \quad (2.32)$$

$c_{sw}$  is referred to as Sheikholeslami-Wohlert coefficient [26] and  $S_F^W$  is the Wilson action as given in equation (2.23). The simulations are performed using the tree-level  $O(a^2)$  improved Lüscher-Weisz gauge action [27] for the gluons

$$S_{G_{tw}}[U] = \frac{\beta}{6} \left( c_0 \sum_p \text{Tr}(1 - U(p)) + c_1 \sum_r \text{Tr}(1 - U(r)) \right), \quad (2.33)$$

with  $c_0 = \frac{5}{3}$ ,  $c_1 = -\frac{1}{12}$  and  $\beta = \frac{6}{g_0^2}$ . In addition to the sum over plaquettes  $p$  of the Wilson gauge action, the action includes a sum over  $1 \times 2$  rectangles  $r$ .

Twisted-mass reweighting is used to improve stability of the simulations and open boundary conditions are imposed on the gauge field in the temporal direction in order to avoid topological freezing [28]. The simulations are done on lattices of size  $N_S^3 \times N_T$ , with open boundary conditions imposed on time slice 0 and  $N_T$ . Ensemble details are given in table 2.2. In the identifying label, the letter denotes the geometry, the first digit the coupling and the final two label the quark mass combination. Using  $\frac{t_0}{a^2}$  extrapolated to the physical light quark masses, the estimated lattice spacings are  $a \approx 0.086\text{fm}$ ,  $a \approx 0.064\text{fm}$  and  $a \approx 0.05\text{fm}$  for  $\beta = 3.4, 3.55, 3.7$ , respectively [24].

The simulations were performed using the Hybrid Monte Carlo (HMC) algorithm [29], which is currently the most commonly used method used for simulations of full QCD on the lattice. It is called hybrid, because it unifies the Markov chain Monte Carlo algorithm with molecular dynamics (MD). The MD algorithm would be an exact algorithm if the equations of motion were solved exactly. However, integration errors occur because a numerical method is used to solve these equations. Hybrid algorithms which use area-preserving and reversible integrators, like the HMC algorithm, can be made exact by adding a Metropolis acceptance step at the end of the MD trajectory, which stochastically corrects for the errors.

id	$\beta$	$N_s$	$N_t$	$m_\pi$ [MeV]	$m_K$ [MeV]	$m_\pi L$
B105	3.40	32	64	280	460	3.9
H101	3.40	32	96	420	420	5.8
H102	3.40	32	96	350	440	4.9
H105	3.40	32	96	280	460	3.9
C101	3.40	48	96	220	470	4.7
D100	3.40	64	128	130	480	3.7
H200	3.55	32	96	420	420	4.4
<b>N200</b>	3.55	48	128	280	460	4.4
D200	3.55	64	128	200	480	4.2
N300	3.70	48	128	420	420	5.1
N301	3.70	48	128	410	410	4.9
J303	3.70	64	192	260	470	4.1

TABLE 2.2: List of  $N_f = 2 + 1$  ensembles [24]

### Twisted mass reweighting

Dynamical simulations with light quarks pose a variety of difficulties, one is the possibility of running into instabilities triggered by accidental near-zero modes of the Wilson Dirac operator. The operator is not protected against eigenvalues taking values below the quark mass, due to the breaking of chiral symmetry. In simulations based on the HMC algorithm, this effect can lead to barriers of infinite action during MD evolution. Introducing a small twisted-mass term into the action during the simulation gives a strict lower bound [30], but has to be compensated for by reweighting. In [31], it was shown that this procedure works as expected for QCD with  $N_f=2+1$  flavors of Wilson fermions and open boundary conditions in time. For the CLS simulations, the second version of the reweighting suggested in [30] was used. Instead of introducing the twisted mass term in the Hermitian Dirac operator  $Q = \gamma_5 D_W$  as originally proposed, it is introduced to the Schur complement  $\hat{Q} = Q_{ee} - Q_{eo} Q_{oo}^{-1} Q_{oe}$  of the even-odd preconditioning. This leads to a replacement of the determinant of the light quark pair

$$\det Q^2 = \det^2 Q_{oo} \det \hat{Q}^2 \rightarrow \det^2 Q_{oo} \det \frac{\hat{Q}^2 + \mu_0^2}{\hat{Q}^2 + 2\mu_0^2} \det (\hat{Q}^2 + \mu_0^2), \quad (2.34)$$

where  $\mu_0$  is the twisted mass. The reweighting factor is given by

$$W_0 = \det \frac{(\hat{Q}^2 + 2\mu_0^2) \hat{Q}^2}{(\hat{Q}^2 + \mu_0^2)^2}. \quad (2.35)$$

The twisted mass parameter  $\mu_0 > 0$  acts as an infrared regulator of the quark determinant and is usually set to a value of the order of the light quark mass [31]; taking the twisted mass to infinity amounts to decoupling of the sea quarks and thus the quenched approximation.

The heavier strange quark is simulated using the rational hybrid Monte Carlo RHMC algorithm [32]. The reason for using another algorithm for the one-flavor sector is that the determinant is used as a probability weight for HMC. Thus the determinant has to be real and non-negative.  $\gamma_5$  hermiticity of the Dirac operator implies that the determinant is real. Non-negativity is easy to show for the light quarks, assuming degeneracy  $D_u = D_d$ :

$$0 \leq \det[Q_u] \det[Q_d] = \det[Q] \det[Q] = \det[Q] \det[Q^\dagger] = \det[QQ^\dagger]. \quad (2.36)$$

In general, for an even number of mass-degenerate quarks, the determinant is raised to an even power and the combined weight factor is non-negative.  $\det[Q]$  is positive if the quark mass is large enough and this is the case for the strange quark. In order to include the strange quark, a method for HMC simulations with an odd number of dynamical fermions is needed. One possibility is using RHMC, where the square root of  $QQ^\dagger$  is approximated. To correct this approximation, the reweighting factor for the strange quark  $W_1$  is implicitly defined by

$$\det Q = \det Q_{\text{oo}} \det \sqrt{\hat{Q}^2} = \det Q_{\text{oo}} \det \left( A^{-1} \prod_{i=1}^{N_p} \frac{\hat{Q}^2 + \bar{\mu}_i^2}{\hat{Q}^2 + \bar{\nu}_i^2} \right) \times W_1. \quad (2.37)$$

The parameters  $A$  and  $\{\bar{\mu}_i, \bar{\nu}_i\}$  are given by Zolotarev's optimal approximation for the inverse square root of the Schur complement of the hermitian Dirac operator  $\hat{Q}$  [33].

Given the twisted mass and RHMC reweighting factors, primary observables can now be computed from expectation values in the theory with the modified action  $\langle \dots \rangle_W$  and the reweighting factor  $W = W_0 W_1$  needs to be included according to

$$\langle A \rangle = \frac{\langle AW \rangle_W}{\langle W \rangle_W}. \quad (2.38)$$

### Open boundary conditions

Simulations with small lattice spacings can get trapped in fixed topological charge sectors of field space which might lead to an incomplete sampling of the path integral and thus biased results. It was shown that the problem is ameliorated if open boundary conditions are imposed in the time direction [28]. With open boundary conditions, the topological charge can change smoothly along a MD trajectory by flowing in and out of the lattice through its boundaries.

While periodic boundary conditions are imposed on the fields in spatial directions, time runs from 0 to  $T$  inclusively, the terminal time-slices are called the boundaries of the lattice.

The Lüscher-Weisz gauge action (2.33) is now given by

$$S_{G_{lw}}[U] = \frac{\beta}{6} \left( c_0 \sum_p w(p) \text{Tr}(1 - U(p)) + c_1 \sum_r w(r) \text{Tr}(1 - U(r)) \right), \quad (2.39)$$

where the time coordinate  $x_0$  of the corners of all the plaquettes and rectangles must be in the range  $0 \leq x_0 \leq T$ . The weights  $w(p)$  and  $w(r)$  are equal to 1, except for spatial loops on the boundaries at time 0 and  $T$ , where the weights are equal to  $\frac{1}{2}c_G$ . The coefficient  $c_G$  is required for  $O(a)$  improvement for correlation functions close to or at the boundary [28], with  $c_G = 1$  ensuring on-shell improvement at tree-level of perturbation theory.

The Wilson action (2.23) for the fermion fields can be expressed as

$$S_F^W[\psi, \bar{\psi}, U] = a^4 \sum_{x_i} \sum_{x_0=a}^{T-a} \bar{\psi}(x) (D_W + m) \psi(x). \quad (2.40)$$

The quark and antiquark fields  $\psi(x)$  and  $\bar{\psi}(x)$  need to satisfy the following boundary conditions:

$$\begin{aligned} P_+ \psi(x)|_{x_0=0} = P_- \psi(x)|_{x_0=T} = 0, \quad P_{\pm} = \frac{1}{2}(1 \pm \gamma_4), \\ \bar{\psi}(x)P_-|_{x_0=0} = \bar{\psi}(x)P_+|_{x_0=T} = 0. \end{aligned} \quad (2.41)$$

Since the action  $S_F^W$  only depends on the quark fields at times  $0 < x_0 < T$ , it is allowed to set all components of the fields at time 0 and  $T$  to zero. The dynamical components of the quark fields are living in the inner part of the lattice. The path integral and correlation functions are now defined accordingly as before. The Wilson-Dirac operator stays  $\gamma_5$ -hermitian with these boundary conditions.

The downside to using open boundary conditions is that time translational invariance is lost. Sufficiently far away from the boundaries, local observables are expected to assume their vacuum expectation values up to exponentially small corrections with a decay rate equal to the lightest excitation that carries the quantum numbers of the vacuum [28]. Hence, the boundary effects are expected to decay close to the chiral limit as  $\exp(-2m_\pi x_0)$ , so the region close to the boundaries is large and as a consequence one can lose a lot of statistics. Additionally, large discretization errors are observed close to the boundary. This means that when employing open boundary conditions, it is very important to avoid unwanted boundary effects. What portion of the lattice needs to be neglected depends on the observable and the statistical precision of the data. In order to ensure this, we employ only the central half of the time slices in our calculations.

## Chapter 3

# Methodology

After the gauge field configurations have been generated, Wilson loops, hadron correlation functions and any other function of the gauge field are calculated on those configurations. These are the primary observables of the theory, which means all physical quantities are eventually obtained from them. In this chapter, the extraction of masses and energies of hadrons, so called hadron spectroscopy, is discussed. There are many approaches to calculating propagators, which are the building blocks of hadron correlation functions. Smearing techniques used in this work and the stochastic LapH method are described in subsections 3.2 and 3.3, respectively. In the simplest case, the extraction of masses can be done by fitting exponentials to the Euclidean correlator. This approach is especially feasible for extracting the ground state of an observable. In order to access higher lying states, more complicated methods are needed, such as the variational method, which are discussed in subsection 3.4.

### 3.1 Correlation functions

For the Wilson formulation of Lattice QCD as presented in section 2.1.2, it was proven that for the discretization of the Euclidean action, the physical Hilbert space in the Minkowski theory can be obtained in a constructive way [34, 35]. Since lattice calculations are performed in Euclidean space, it is important to know if the corresponding Minkowski theory is physical. In general, it is necessary to analytically continue the correlation functions to Minkowski space in order to yield physical quantities. However, the spectrum remains unchanged by analytic continuation and can be computed in either Minkowski or Euclidean space. Therefore, the spectrum can be calculated directly from Euclidean two point functions by analyzing the exponential fall-off of the Euclidean correlator [36].

A hadron spectroscopy calculation using Lattice QCD is usually performed in the following way [14, 15]. The first step is to find suitable interpolators  $\mathcal{O}$ , so that the corresponding Hilbert space operators  $O$  create the particle states one wants to analyze. The interpolators are functionals of the lattice fields, they are constructed using quark and gluon fields to form

gauge-invariant color singlets. They have to carry the quantum numbers of the states that one wants to extract.

After choosing the interpolators, the next step is the calculation of the Euclidean correlator. The correlation function contains information on every state that can be created by the operators used. It is defined by

$$\langle \mathcal{O}_i(t_f) \bar{\mathcal{O}}_j(t_0) \rangle_T = \frac{1}{\mathcal{Z}} \langle \Omega | e^{-(T-t_f)H} O_i e^{-(t_f-t_0)H} O_j^\dagger e^{-t_0 H} | \Omega \rangle, \quad (3.1)$$

where  $\mathcal{Z} = \langle \Omega | e^{-TH} | \Omega \rangle$  and  $H$  is the Hamilton operator of the system.  $\Omega$  encodes the chosen boundary conditions and has the quantum numbers of the vacuum. To evaluate the correlator on the lattice, an expression as a path integral over all possible field configurations, as given in equation (2.1), is needed. The corresponding relation is given by [14]

$$\frac{1}{\mathcal{Z}} \langle \Omega | e^{-(T-t_f)H} O_i e^{-(t_f-t_0)H} O_j^\dagger e^{-t_0 H} | \Omega \rangle = \frac{1}{\mathcal{Z}} \int \mathcal{D}[\Phi] \mathcal{O}_i[\Phi(t_f)] \bar{\mathcal{O}}_j[\Phi(t_0)] e^{-S_E[\Phi]}. \quad (3.2)$$

This displays how the operator language of quantum field theory on the left can be translated into functionals of fields, weighted with the Euclidian action  $S_E$ . As explained in chapter 1, the right hand side, and thus the correlator, can be numerically evaluated on the lattice using MC methods.

After insertion of a complete set of eigenstates of  $H$  to evaluate expression (3.1), one finds:

$$\begin{aligned} \langle \mathcal{O}_i(t_f) \bar{\mathcal{O}}_j(t_0) \rangle_T &= \frac{1}{\mathcal{Z}} \sum_n \langle \Omega | e^{-(T-t_f)H} O_i e^{-t_f H} | n \rangle \langle n | e^{t_0 H} O_j^\dagger e^{-t_0 H} | \Omega \rangle \\ &= \frac{1}{\mathcal{Z}} \sum_n e^{-(T-t_f)E_n} \langle \Omega | O_i | n \rangle e^{-t_f E_n} e^{t_0 E_n} \langle n | O_j^\dagger | \Omega \rangle e^{-t_0 E_n}. \end{aligned} \quad (3.3)$$

The correlator depends only on the energies normalized relative to the energy of the vacuum, which is arbitrary. Adding a constant term to the Hamiltonian does not change the expectation values, so only energy differences have physical meaning. If the energy of the vacuum is normalized to 0, the limit  $T \rightarrow \infty$  for periodic boundary conditions can be expressed as

$$\lim_{T \rightarrow \infty} \langle \mathcal{O}_i(t_f) \bar{\mathcal{O}}_j(t_0) \rangle_T = \langle \mathcal{O}_i(t_f) \bar{\mathcal{O}}_j(t_0) \rangle = \sum_n \langle 0 | O_i | n \rangle \langle n | O_j^\dagger | 0 \rangle e^{-E_n(t_f-t_0)} \quad , \quad n \geq 0. \quad (3.4)$$

This is a sum of exponentials where each term corresponds to an energy level. Even though it is impossible to go to asymptotic times on a finite lattice, the contributions of higher energy states are falling off exponentially in Euclidean time with a value governed by their energy difference to the ground state as an exponent. This means for large  $t = t_f - t_0$ ,

the excited states are strongly suppressed. Even though it is often achievable to reach a distance effectively asymptotic even for limited time extents, periodic boundary conditions can lead to thermal effects due to wrapping around the finite temporal extend, while for open boundary conditions contributions are added due to states with vacuum quantum numbers propagating off the temporal boundary [28]

$$\lim_{\substack{T \rightarrow \infty \\ t_0, T-t_f \rightarrow \infty}} \langle \mathcal{O}_i(t_f) \overline{\mathcal{O}}_j(t_0) \rangle_T = \langle \mathcal{O}_i(t_f) \overline{\mathcal{O}}_j(t_0) \rangle (1 + \mathcal{O}(e^{-E_0 t_{\text{bnd}}})) . \quad (3.5)$$

$E_0$  is the lightest state carrying vacuum quantum numbers and  $t_{\text{bnd}} = \min(t_0, T - t_f)$  is the minimal distance to the boundaries. While correlations functions feel the effect of the boundaries, the transfer matrix and thus the space of physical states are independent of the boundary conditions.

If  $O_j^\dagger$  is an operator which creates the state with the right quantum numbers from the vacuum and  $O_i$  the corresponding operator which annihilates this state at a later time  $t$ , then the ground state energy can be extracted from the exponential decay of the Euclidean correlator

$$C_{ij}(t) = \langle \mathcal{O}_i(t) \overline{\mathcal{O}}_j(0) \rangle = \sum_n \langle 0 | O_i | n \rangle \langle n | O_j^\dagger | 0 \rangle e^{-tE_n} . \quad (3.6)$$

The amplitudes are called overlap factors and determine the overlap of the interpolators with the physical states. If the correlator  $C_{ij}(t)$  is hermitian

$$\langle 0 | O_i | n \rangle = \langle n | O_i^\dagger | 0 \rangle^* \quad (3.7)$$

the overlap factors can be defined as

$$Z_i = \langle 0 | O_i | n \rangle \quad (3.8)$$

$$Z_i^* = \langle n | \overline{O}_i | 0 \rangle . \quad (3.9)$$

The correlator can be rewritten as

$$C_{ij}(t) = \sum_n Z_i Z_j^* e^{-tE_n} . \quad (3.10)$$

To analyze at which times the contributions of sub-leading exponentials become negligible, the effective mass can be defined as

$$am_{\text{eff}} = \ln \frac{C_{ij}(t)}{C_{ij}(t+1)} . \quad (3.11)$$

The mass  $m_{\text{eff}}$  becomes a constant at large time separations, once the correlator is dominated by the ground state and plateaus at  $E_0$ , but statistical errors grow with  $t$ . The onset as well as the length of the plateau depend on  $O$ . The hadron mass can be extracted from fits to data in this plateau region, as explained in section 3.4.

### 3.1.1 Symmetries

Eigenstates of the Hamiltonian are simultaneous eigenstates of operators that commute with the Hamiltonian, these operators generate a symmetry. The eigenstates can be identified by their symmetries. Since the lattice has a reduced set of symmetries in comparison to the continuum, it is essential to understand the properties of lattice states under symmetry transformations in order to identify the physical hadrons built by the chosen interpolators.

In the continuum and infinite volume limits, the spacetime symmetries of the QCD action are given by the Poincaré group  $P$  [37]. The spatial symmetries of the QCD Hamiltonian correspond to a subgroup of  $P$ :  $O(3) \times \mathcal{T}^3$ , the semi-direct product of the improper rotation group and the group of abelian translations. QCD observable states are classified according to their transformation properties under the irreducible transformations (irreps) of  $O(3)$ , which are conventionally named  $J^P$ , where  $J$  is the spin,  $P$  is parity. On a spatially isotropic lattice, the continuum symmetry is reduced to  $O_h \times \mathcal{T}_{\text{latt}}^3$  [38], the semi-direct product of  $O_h$ , the octahedral group with only a finite number of rotations and reflections and  $\mathcal{T}_{\text{latt}}^3$ , the abelian group of lattice translations. Lattice interpolators must transform according to the irreps of  $O_h$  in order to create eigenstates of the lattice Hamiltonian with well-defined quantum numbers. The states that transform according to the irreps of  $O_h$  are labeled  $\Lambda^P$ . There are ten single-cover lattice irreps:  $A_{1g}, A_{2g}, E_g, T_{1g}, T_{2g}$  and  $A_{1u}, A_{2u}, E_u, T_{1u}, T_{2u}$ . The g (gerade) and u (ungerade) label the behaviour under spatial inversion. While for mesons the single cover of  $O_h$  is considered, the double cover of the group  $O_h^D$  is used to describe baryons [39]. For hadrons with non-zero momentum, the symmetry is further reduced and the group theory becomes more involved [40, 41].

The interpolators are, as mentioned before, constructed using quark and gluon fields. For instance, the simplest meson interpolators are color-singlet local fermion bilinears [42]

$$O_M \equiv \bar{\psi}_\alpha(x) \Gamma_{\alpha\beta} \psi_\beta(x), \quad (3.12)$$

where  $\Gamma$  is a gamma matrix, which has to be chosen according to the transformation properties of the state, i.e. the quantum numbers, one is interested in. These simple local operators allow access only to a small set of  $J^P$ , in order to consider higher or exotic spin states or produce multiple operators within a given symmetry channel on the lattice, one must consider the use of spatially extended, nonlocal operators, see for example [43, 44]. In general,



the connection between quantum numbers in the continuum and quantum numbers on the lattice must be assessed carefully.

The reduction of the symmetry on the lattice manifests itself in the possible distribution of continuum states of the same  $J^P$ , but different  $J_Z$ , across different lattice irreps. There is no one-to-one mapping [45]. The link to the continuum symmetry group and thus the classification of states by their continuum quantum numbers can be made by subducing the representations of  $O(3)$  into  $O_h$ . The single-valued irreps correspond to bosonic and the double-valued irreps correspond to fermionic states. The simplest case is the subduction of  $J = 0, 1$ , they subduce into the  $A_1$  and  $T_1$  irrep, respectively. Only spins 0 and 1 are described by a single octahedral irreducible representation, while other spins have to be described by two or more [38, 42]. The interpolators and symmetries that are important for string breaking, are discussed in section 4.3.

Usually the interpolating operators have to be optimized, because any operator with the correct quantum numbers contributes to a physical state. Maximizing the overlap for these operators with the ground state can be achieved by quark and gluon smearing. Different methods are described in the next subsection.

## 3.2 Smearing

The goal is to find interpolators which improve the groundstate overlap. One commonly used technique to achieve this is quark and gauge field smearing. Quark field smearing, for example Wuppertal-smearing [46], can reduce the contamination by excited states, but it is important to use the smeared gauge fields when smearing the quark fields [47]. Link smearing, for example Stout- [48], or hypercubic (HYP) smearing [49], also reduces the statistical errors in the correlators, the details of the smearing techniques used in this project are given below.

### 3.2.1 Stout-link smearing

For states containing gluons, a crucial ingredient in constructing operators which couple more strongly to the states of interest and less strongly to the higher-lying contaminating states is link smearing. The algorithm most often used in gluonic operator construction is APE smearing [50], which amounts to replacing each thin spatial link  $U_j(x)$  by a weighted sum of its four neighboring (spatial) staples, projected back into  $SU(3)$ . Such a fuzzing step can be iterated to obtain the final so called fat link variables. The projection into  $SU(3)$  is an important part of the smearing and not unique. It must be defined in a way that preserves

all symmetry properties of the link variables. The problem with such an abrupt way to stay inside the gauge group is the lack of differentiability. It prevents the application of MC updating techniques, such as HMC, because they need to know the response of the action to a small change in a link variable. A link smearing method which is analytic everywhere in the finite complex plane and thus differentiable, was proposed and tested in [48], the so called stout smearing. It utilizes the exponential function to remain within  $SU(3)$ , so that no projection back into the group is required. According to [48] the smearing is iteratively defined by an algorithm in which the links  $U_\mu^{(n)}(x)$  at step  $n$  are mapped into links  $U_\mu^{(n+1)}(x)$  using

$$U_\mu^{(n+1)}(x) = \exp\left(iQ_\mu^{(n)}(x)\right) U_\mu^{(n)}(x). \quad (3.13)$$

The matrix  $Q_\mu(x)$  given by

$$\begin{aligned} Q_\mu(x) &= \frac{i}{2} \left( \Omega_\mu^\dagger(x) - \Omega_\mu(x) \right) - \frac{i}{2N} \text{Tr} \left( \Omega_\mu^\dagger(x) - \Omega_\mu(x) \right), \\ \Omega_\mu(x) &= C_\mu(x) U_\mu^\dagger(x), \quad (\text{no summation over } \mu) \end{aligned} \quad (3.14)$$

is Hermitian, traceless and an element of the Lie algebra.  $C_\mu(x)$  represents a weighted sum of the perpendicular staples which reach from lattice site  $x$  to a neighboring site  $x + \hat{\mu}$ :

$$\begin{aligned} C_\mu(x) &= \sum_{\nu \neq \mu} \rho_{\mu\nu} \left( U_\nu(x) U_\mu(x + \hat{\nu}) U_\nu^\dagger(x + \hat{\mu}) \right. \\ &\quad \left. + U_\nu^\dagger(x - \hat{\nu}) U_\mu(x - \hat{\nu}) U_\nu(x - \hat{\nu} + \hat{\mu}) \right), \end{aligned} \quad (3.15)$$

where  $\hat{\mu}, \hat{\nu}$  are unit vectors in directions  $\mu, \nu$ , respectively and the weights  $\rho_{\mu\nu}$  are tunable real parameters. It is important to note, that because  $e^{iQ_\mu(x)}$  is an element of  $SU(3)$ , the same is true for  $U_\mu^{(n+1)}(x)$  in equation (3.13), eliminating the demand for projecting back into the gauge group. The stout links retain symmetry transformation properties identical to those of the original links, given an appropriate choice of the weights  $\rho_{\mu\nu}$ .

### 3.2.2 HYP-smearing

The HYP fat link [49] mixes gauge links within hypercubes attached to the original link only, so that the smearing eliminates UV-fluctuations, but remains localized. One level of HYP smearing consists of three levels of modified APE smearing. The links entering the staples are projected back into the gauge group  $SU(3)$ . The links can be constructed in three steps, the construction can then be iterated:

1. The first step is the design of decorated links  $\bar{V}_{\mu;\rho\nu}(x)$  using the original thin links with a modified projected APE blocking

$$\bar{V}_{\mu;\rho\nu}(x) = \text{Proj}_{SU(3)}[(1 - \alpha_3)U_\mu(x) + \frac{\alpha_3}{2} \sum_{\pm\eta \neq \rho, \nu, \mu} U_\eta(x)U_\mu(x + \hat{\eta})U_\eta(x + \hat{\mu})^\dagger], \quad (3.16)$$

where  $U_\mu(x)$  is the original link. Only the two staples orthogonal to  $\mu$ ,  $\nu$  and  $\rho$  are being used.

2. The second step is the construction of higher level decorated links  $\tilde{V}_{\mu;\nu}(x)$  from links decorated according to step 1,  $\bar{V}_{\mu;\rho\nu}(x)$  as

$$\tilde{V}_{\mu;\nu}(x) = \text{Proj}_{SU(3)}[(1 - \alpha_2)U_\mu(x) + \frac{\alpha_2}{4} \sum_{\pm\rho \neq \nu, \mu} \bar{V}_{\rho;\nu\mu}(x)\bar{V}_{\mu;\rho\nu}(x + \hat{\rho})\bar{V}_{\rho;\nu\mu}(x + \hat{\mu})^\dagger], \quad (3.17)$$

where the indices  $\rho\nu$  indicate that the fat link  $\bar{V}_{\mu;\rho\nu}(x)$  in direction  $\mu$  is not decorated with staples extending in the  $\rho$  or  $\nu$  directions.

3. The final step provides the fat HYP link  $V_\mu(x)$  via

$$V_\mu(x) = \text{Proj}_{SU(3)}[(1 - \alpha_1)U_\mu(x) + \frac{\alpha_1}{6} \sum_{\pm\nu \neq \mu} \tilde{V}_{\nu;\mu}(x)\tilde{V}_{\mu;\nu}(x + \hat{\nu})\tilde{V}_{\nu;\mu}(x + \hat{\mu})^\dagger]. \quad (3.18)$$

The index  $\nu$  in  $\tilde{V}_{\mu;\nu}(x)$  expresses that the fat link at location  $x$  and direction  $\mu$  is not decorated with staples extending in direction  $\nu$ .

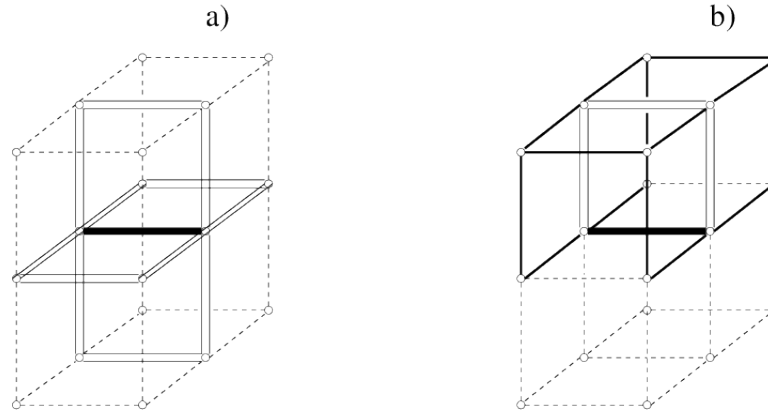


FIGURE 3.1: Construction mechanism of HYP-smearing shown in 3d [49]. a) shows fat link built from four double-lined staples, b) shows how the double-lined staples are constructed from two staples which stay inside the hypercube attached to the original link.

The parameters  $\alpha_1$ ,  $\alpha_2$  and  $\alpha_3$  can be optimized to achieve the smoothest blocked link configuration. The 3d schematic construction is displayed in figure 3.1. It was shown [51], that

for the static potential extracted using Wilson loops, the statistical precision of the potential measured with HYP links improves by about an order of magnitude.

### 3.2.3 Distillation

As mentioned above, using smeared quark fields is a well-established way to reduce high frequency modes and thus especially important if one wants to extract low-lying energies. A special quark-field smearing algorithm is distillation [52]. It applies a low-rank operator to define smooth fields that are to be used in hadron creation operators. The dimension of the resulting subspace of smooth fields is so small, that all elements of the reduced quark propagator can be computed exactly in moderately sized lattices. These all-to-all propagators are necessary to calculate definite momentum multi-hadron correlation functions as well as disconnected Wick contractions of correlation functions, which appear in the string breaking calculation. In these cases estimates of the quark propagators from all spatial sites to all spatial sites are needed.

It is desirable for the smeared fields  $\tilde{\psi}$  to have the same single time-slice-symmetry properties as the original fields  $\psi$ , which is satisfied by every smearing scheme defined in powers of the covariant Laplacian acting on the quark field. The three-dimensional lattice Laplacian is given by:

$$\tilde{\Delta}^{ab}(x, y; U) = \sum_{k=1}^3 \left\{ \tilde{U}_k^{ab}(x) \delta(y, x + \hat{k}) + \tilde{U}_k^{ba}(y)^* \delta(y, x - \hat{k}) - 2\delta(x, y) \delta^{ab} \right\}, \quad (3.19)$$

where  $x, y$  are lattice sites,  $a, b$  are color indices and  $\tilde{U}_k^{ab}(x)$  are the gauge fields, constructed using stout smeared gauge links [48]. Now, it is possible to define a simple smearing operator

$$\tilde{\psi} = \left( 1 + \frac{\sigma \tilde{\Delta}}{n_\sigma} \right)^{n_\sigma} \psi. \quad (3.20)$$

$\sigma$  and  $n_\sigma$  are tunable parameters that can be used to change projection properties onto the states under investigation. If one defines the quark-field smearing kernel as

$$K = \left( 1 + \frac{\sigma \tilde{\Delta}}{n_\sigma} \right)^{n_\sigma}, \quad (3.21)$$

it can be rewritten in terms of the eigenvalues  $\lambda$ , with  $\lambda > 0$ , and eigenvectors  $v$  of the Laplacian:

$$K_{ab}(x, y) = \delta_{x_4, y_4} \sum_k \omega_k v_a^k(x) v_b^k(y)^*, \quad (3.22)$$

where  $\omega_k$  are real and positive weights:

$$\omega_k = \left( 1 - \frac{\sigma \lambda^{(k)}(t)}{n_\sigma} \right)^{n_\sigma}. \quad (3.23)$$

For large  $n_\sigma$ , this tends to

$$\lim_{n_\sigma \rightarrow \infty} \omega_k = \exp\left(-\sigma \lambda^{(k)}\right). \quad (3.24)$$

The effect of these smearing weights is the suppression of contributions from the higher eigenmodes; only a small number of the lowest modes contribute substantially. Assuming that the lowest modes contain the physical information, a smearing operator can be constructed by forming an eigenvector representation, only taking the lowest modes into account. The simplest function to facilitate this is the Heaviside-function, the corresponding smearing kernel is:

$$S_{ab}(x, y) = \Theta(\sigma^2 + \tilde{\Delta}). \quad (3.25)$$

Since we only want to use spatial smearing, the smearing kernel is diagonal in time:

$S_{ab}(\mathbf{x}, t; \mathbf{y}, t_0) \propto \delta_{t, t_0}$ . It is also important to note that the kernel is independent of spin.

Let  $V_M$  define the matrix of rank  $M$  containing all eigenvectors, where  $M = N_t N_s^3 N_c$  on a lattice with  $N_t$  time slices,  $N_s$  sites for each spatial direction and  $N_c$  quark colors. The quark-smearing operator is chosen to be of rank  $N = N_v N_t$ , much smaller than  $M$ , where  $N_v$  are the lowest lying eigenvalues on each time slice. The class of these operators is called distillation operators [52] and the smearing-technique is called Laplacian-Heaviside-smearing (LapH) [53]. The LapH-smearing truncates the sum in equation (3.22)

$$S_{ab}(x, y) = \delta_{x_4, y_4} \sum_k^{N_v} v_a^k(x) v_b^k(y)^*. \quad (3.26)$$

The eigenvectors are orthogonal

$$\sum_{a, x} v_a^k(x) v_a^j(x)^* = \delta_{jk}, \quad (3.27)$$

and sorted by eigenvalue

$$\sum_{b, y} \tilde{\Delta}(x, y) v_b^k(y) = -\lambda^k(t) v_a^k(x), \quad \lambda^k(t) \leq \lambda^{k+1}(t) \dots \quad (3.28)$$

In matrix notation, the distillation operator or smearing matrix can be written as

$$S = VV^\dagger, \quad \text{with} \quad V^\dagger V = 1. \quad (3.29)$$

It is a product of an  $M \times N$  Matrix  $V$  and its hermitian conjugate and is the projection operator into the smaller LapH subspace.

A quark propagator in the distillation subspace  $\mathcal{D}(\mathbf{y}, t; \mathbf{x}, t_0)$  can now be written as the following product of matrices after applying the distillation operator to each quark field

$$\mathcal{D}(\mathbf{y}, t; \mathbf{x}, t_0) = S\Omega^{-1}S = V(V^\dagger\Omega^{-1}V)V^\dagger, \quad (3.30)$$

where  $\Omega^{-1} = D^{-1}\gamma_4$ . Here  $D$  is the Dirac matrix, this is conventional to ensure hermiticity for baryonic correlation matrices. Instead of computing and storing all elements of  $\Omega^{-1}$ , it suffices to find the smaller matrix  $V^\dagger\Omega^{-1}V$ .

If  $N_d = 4$  denotes the number of Dirac spin components, define

$$y_{c\beta}^{(k,\alpha)}(x) = V(c, x; k) \delta_{\alpha\beta}, \quad (3.31)$$

where  $\alpha, \beta$  are spin indices,  $c$  indicates color and  $k$  refers to the column of  $V$ , which is the  $k$ -th eigenvector of the Laplacian. Solving the linear system  $\Omega b = y^{(k,\alpha)}$  for  $b$  and all  $k, \alpha$  one finds  $\Omega^{-1}V^{(k)}$ . So in order to find the smaller matrix  $V^\dagger\Omega^{-1}V$ ,  $N_v N_t N_d$  such inversions have to be performed for each quark mass and gauge configuration in the ensemble, where  $N_d$  denotes the number of Dirac components. The number  $N_v$  of required eigenvectors for a fixed  $\sigma^2$  cutoff scales with the volume of the lattice [53] and thus the number of inversions needed is still too high to be feasible for bigger lattices.

One solution to this problem is the stochastic estimation of the quark propagator. The smearing scheme facilitates this in a convenient way, which is shown in the next section. Even though distillation can be used on its own to find all-to-all propagators on small lattices, it is often combined with other methods to reduce computational cost.

### 3.3 Stochastic LapH method

If one wants to evaluate hadron correlation functions, one of the biggest problems is the inversion of the Dirac-matrix that appears in the fermionic action. Computing all elements is most of the times impossible. For propagators from one source point to all other points, there are methods to reduce computational cost. As mentioned above, for multi hadron states and disconnected diagrams propagators from all spatial sites to all spatial sites have to be computed, which makes the situation more complicated. One way to handle the problem is to stochastically estimate the inverse of this large matrix using random noise vectors and combine this approach with Distillation to facilitate all-to-all propagation and ameliorate the volume scaling [53].

Since the path integrals are being evaluated using a Monte Carlo based method, the statistical errors for the hadron correlators are bound by the statistical fluctuations arising from sampling the gauge-field. This means that the propagators only have to be estimated to a comparable accuracy, exact treatment is not necessary and can even be wasteful. The propagator can also be approximated using the Monte Carlo Method.

Random noise vectors  $\eta$  can be used for stochastically estimating the inverse of the large Dirac matrix. The vectors  $\eta$  satisfy the following properties

$$\begin{aligned} E(\eta_i) &= 0 \\ E(\eta_i \eta_j^*) &= \delta_{ij}, \end{aligned} \quad (3.32)$$

where  $E()$  denotes the expectation value over the random noise sources. For each noise vector, the following system of linear equations can be solved:

$$\Omega X^r = \eta^r \quad (3.33)$$

for  $X^r$ , where  $r$  labels the noise vectors  $r = 1, 2, \dots, N_R$ . Then  $X^r = \Omega^{-1} \eta^r$  and the expectation value is given by

$$E(X_i \eta_j^*) = E\left(\sum_k \Omega_{ik}^{-1} \eta_k \eta_j^*\right) = \sum_k \Omega_{ik}^{-1} E(\eta_k \eta_j^*) = \sum_k \Omega_{ik}^{-1} \delta_{kj} = \Omega_{ij}^{-1}. \quad (3.34)$$

The left-hand-side can be estimated using the Monte Carlo method, which provides an estimate of  $\Omega_{ij}^{-1}$  given by

$$\Omega_{ij}^{-1} \approx N_R^{-1} \sum_{r=1}^{N_R} X_i^r \eta_j^{r*}. \quad (3.35)$$

The problem with this expression is that the variances of the stochastic estimates are usually much too large and hence, the noisy estimates need variance reduction techniques to separate signal from noise. This is possible through dilution of the noise vectors [54,55].

### Dilution

For every noise vector, one can define:

$$\eta_j^r = \sum_{b=1}^N \eta_j^{r[b]}, \quad \eta_j^{r[b]} = \eta_j^r \delta_{jb}, \quad \text{where } j \text{ is not summed over.} \quad (3.36)$$

$\eta^{r[b]}$  is an N-component vector where all components are zero except the  $b^{\text{th}}$  component.

A dilution scheme amounts to the application of a complete set of projection operators  $P^{(b)}$ , which ensure exact zeros for many of the  $E(\eta_i \eta_j^*)$  elements instead of estimates that are only statistically zero. This reduces the variance dramatically. The dilution projectors  $P^{(b)}$  are products of time dilution, spin dilution, and LapH eigenvector dilution projectors. The diluted sources are defined as

$$\eta^{r[b]} = P^{(b)} \eta^r, \quad (3.37)$$

where the matrices  $P^{(b)}$  satisfy

$$P^{(a)} P^{(b)} = \delta_{ab} P^{(a)}, \quad \sum_{a=1}^{N_a} P^{(a)} = 1, \quad P^{(a)\dagger} = P^{(a)}. \quad (3.38)$$

$X^{r[b]}$  is the solution of

$$\Omega X^{r[b]} = \eta^{r[b]}. \quad (3.39)$$

Now the Monte Carlo estimate of  $\Omega_{ij}^{-1}$  given in equation (3.35) can be rewritten as

$$\Omega_{ij}^{-1} \approx \frac{1}{N_R} \sum_{r=1}^{N_R} \sum_{b=1}^{N_b} X_i^{r[b]} \eta_j^{r[b]*}. \quad (3.40)$$

Although the expectation value is the same, the variance of  $\sum_a \eta_k^{[a]} \eta_j^{[a]*}$  is smaller than the variance of  $\eta_k \eta_j^*$ . The effectiveness of the variance reduction depends on the projectors chosen. The use of  $Z_N$  noise ensures zero variance in the estimates of diagonal elements  $E(\eta_i \eta_i^*)$  [56].

It is now possible to introduce the noise on the entire lattice [57], but distillation offers a more effective way. Noise vectors  $\rho$  are being introduced only in the smaller LapH-subspace, which have spin, time and eigenmode as their indices. The Dilution projectors are matrices in the subspace and each component of  $\rho$  is a random  $Z_N$  variable with  $E(\rho) = 0$  and  $E(\rho \rho^\dagger) = I_d$ . Note that  $\rho \rho^\dagger$  is an outer product.  $I_d$  is the identity matrix. A quark line as in equation (3.30) can now be written down in the following way

$$\begin{aligned} \mathcal{D} &= S \Omega^{-1} S, \\ &= S \Omega^{-1} V V^\dagger \\ &= \sum_b S \Omega^{-1} V P^{(b)} P^{(b)\dagger} V^\dagger \\ &= \sum_b S \Omega^{-1} V P^{(b)} E(\rho \rho^\dagger) P^{(b)\dagger} V^\dagger \\ &= \sum_b E \left( S \Omega^{-1} V P^{(b)} \rho (V P^{(b)} \rho)^\dagger \right). \end{aligned} \quad (3.41)$$



The estimate of a quark line on a given gauge configuration therefore reads

$$\mathcal{D}_{uv}^{(ij)}(\mathbf{y}, t; \mathbf{x}, t_0) \approx \frac{1}{N_R} \delta_{ij} \sum_{r=1}^{N_R} \sum_{b=1}^{N_b} \varphi_u^{r[b]}(\mathbf{y}, t) \varrho_v^{r[b]*}(\mathbf{x}, t_0). \quad (3.42)$$

A quark line is a matrix in space, time, spin and color space. The subscripts  $u, v$  are compound indices indicating color and spin,  $i, j$  denote the flavor of the source and sink field.  $N_R$  and  $N_b$  are the number of independent stochastic noise sources and the number of dilution projectors corresponding to the chosen dilution scheme, respectively. The smeared-diluted quark source and quark sink vectors are defined as

$$\varrho^{r[b]}(\mathbf{x}, t) = (VP^{(b)}\rho^r)(\mathbf{x}, t), \quad \varphi^{r[b]}(\mathbf{x}, t) = [S\Omega^{-1}VP^{(b)}\rho^r](\mathbf{x}, t). \quad (3.43)$$

It is now apparent that a quark line factorizes into an outer product of a source vector and a sink vector. This allows for separate construction of the source and sink hadrons. Source and sink operators can be correlated after all elements of  $\varphi^{[b]}(\rho)$  have been computed and stored once. For an unbiased estimation, it is necessary that each quark line in a hadron correlator has independent noise. For a meson correlator, this means at least two independent noises per configuration.

As mentioned above, the dilution projectors  $P^{(b)}$  used for this work are direct products of time dilution, spin dilution and LapH eigenvector dilution projectors. So  $b = (b_T, b_S, b_L)$  is a triplet of indices, where  $b_T$  is the time projector index,  $b_S$  is the spin projector index and  $b_L$  is the LapH eigenvector projector index. The noise-dilution projectors have the form

$$P_{t\alpha n; t'\alpha'n'}^{(b)} = P_{t;t'}^{(b_T)} P_{\alpha;\alpha'}^{(b_S)} P_{n;n'}^{(b_L)}, \quad (3.44)$$

where  $t, t'$  refer to time slices,  $\alpha, \alpha'$  are Dirac spin indices, and  $n, n'$  are LapH eigenvector indices. We use projectors which are diagonal with some or all of the diagonal elements set to unity and all other elements vanishing.  $N$  denotes the dimension of the space of the dilution type of interest.

$$\begin{aligned} P_{ij}^{(b)} &= \delta_{ij}, & b &= 0, & \text{(no dilution)} \\ P_{ij}^{(b)} &= \delta_{ij} \delta_{bi}, & b &= 0, \dots, N-1 & \text{(full dilution)} \\ P_{ij}^{(b)} &= \delta_{ij} \delta_{b, i \bmod J} & b &= 0, \dots, J-1, & \text{(interlace-}J\text{)} \end{aligned}$$

where  $i, j = 0, \dots, N-1$ . A triplet  $(T, S, L)$  specifies a dilution scheme, where  $T, S$  and  $L$  denote time, spin, and LapH eigenvector dilution, respectively. F stands for full dilution and IJ for interlace- $J$ . For example, full time and spin dilution with interlace-8 LapH eigenvector dilution is denoted by (TF, SF, LI8). If full dilution (TF, SF, LF) is used, the exact propagator

could be computed with using one noise source only. This so called homeopathic limit corresponds to distillation.

It is important to note that full spin dilution is needed, as the intended quantum numbers are only recovered up to stochastic mixing. The interlacing of eigenvectors on the other hand is very beneficial, it helps to ameliorate the volume scaling of the computational cost of inversions. Using eigenvector dilution, the required number of inversions is no longer proportional to  $N_v$  and correspondingly the volume.

In [53], different dilution schemes have been tested using different spatial lattice sizes and pion masses. It was found that (TF, SF, LI8) produces variances near that of the gauge noise limit for correlators  $\mathcal{D}(\mathbf{y}, t_F; \mathbf{x}, t_0)$  with  $t_F \neq t_0$ . For these, inversions are usually computed for a handful of source times only using full time dilution, as correlation functions extracted using nearby source times tend to be highly correlated. The interlacing in time enables the evaluation of correlators which involve propagators that originate and terminate on the same time slice  $t_F = t_0$ , where full dilution in time would not be feasible. The dilution scheme has to be chosen and tested for each ensemble individually to ensure that the variances reach the gauge noise limit.

Using the stochastic LapH method, the number of inversions is equal to  $N_\rho N_P$ , where  $N_\rho$  is the number of noises used and  $N_P$  is the number of dilution projectors. The two key features of the method are the use of noise dilution projectors that interlace in time and the introduction of noise in the LapH subspace instead of the entire lattice. Even though the number of eigenvectors required to span the LapH subspace rises with the Volume, the number of inversions of the Dirac matrix can be kept almost constant if eigenvectors are interlaced.

Another advantage of stochastic LapH lies in the complete factorization of hadron sources and sinks, which facilitates the construction of correlation functions a posteriori. For the calculation of the string breaking diagrams, this is no longer true. The usual workflow is broken because we do not stochastically estimate the static quark propagators. However, the method still allows for an effective calculation of the required correlation matrix elements, which is described in detail in chapter 4.5.

## 3.4 Analysis techniques

### 3.4.1 Extraction of energies

The observables in this work are correlation functions  $C_{ij}(t)$  evaluated as path integrals on the lattice using MC methods. These are, as mentioned above, primary observables. On all  $N_{\text{cfg}}$  configurations, they have a unique value  $C_{ij}^c(t)$ , where  $c = 1, \dots, N_{\text{cfg}}$ . Assuming measurement on  $N_{\text{cfg}}$  statistically independent gauge configurations, a stochastic MC estimate for the average of a collection of  $d = 1, \dots, N_d$  primary observables, with measured values  $a_d^c$  is given by

$$\langle A_d \rangle \equiv \frac{1}{N_{\text{cfg}}} \sum_c^{N_{\text{cfg}}} a_d^c. \quad (3.45)$$

If  $a_d^c$  and  $a_e^c$  are data corresponding to observables  $A_d$  and  $A_e$ , the product  $\langle A_d A_e \rangle$  is given by  $a_d^c a_e^c$ . It is also a primary observable, this is true even for stochastically estimated observables, if the random sources are included as additional fields in the ensemble of fields generated [58]. An estimate of the n-point function  $\langle A_{d_1} \dots A_{d_n} \rangle$  can thus be obtained by calculating the average of  $a_{d_1}^c \dots a_{d_n}^c$ .

The extraction of the effective mass as given in equation (3.11) is useful for a first estimate of the ground state and to show the plateau region, where a fit is performed. Effective masses as well as other functions of primary observables, so called derived observables, can be extracted using best-fit procedures [15], as for example  $\chi^2$  minimization. To do this for MC data, the correlated  $\chi^2$  statistic is needed. Let  $f_a$ ,  $a = 1, \dots, m$ , be the model predictions and  $\langle F_a \rangle$  the MC data. If the model functions depend only on the parameters and not on the data itself, the best-fit estimates of the parameters from statistical estimates of the data are given by the values of  $f_a$  that minimize

$$\chi^2 = \sum_{a,b=1}^m (f_a - \langle F_a \rangle) \Sigma_{ab}^{-1} (f_b - \langle F_b \rangle) \quad (3.46)$$

$$\Sigma_{ab} = \frac{\langle F_a F_b \rangle - \langle F_a \rangle \langle F_b \rangle}{N_{\text{cfg}}^2}, \quad (3.47)$$

where  $\Sigma_{ab}$  is the MC estimate of the covariance matrix between the  $m$  observables. The covariance between the data is needed to properly treat the correlation between observables that are measured on the same ensemble of gauge configurations. The entries in this matrix are again estimated from Monte Carlo data.

The estimate for this large matrix is often hard to determine in practice and especially if the sample size is not sufficiently large, statistical fluctuations can lead to small eigenvalues

destabilizing the fit [59, 60]. By definition, the covariance matrix is a positive semi-definite symmetric matrix. For real data, it might have close to zero eigenvalues as a symptom of statistical instability. One solution to this problem is to apply a singular value decomposition (SVD) to the covariance matrix and remove very small eigenvalues before the inversion is computed [15]. For each singular value that is removed, the effective value of  $m$  is reduced.

In theory, it is possible to take the spectral decomposition of the correlation function in terms of eigenstates, as given in equation (3.10), and perform a fit to the full correlation matrix directly in order to extract the lowest lying eigenstates. Since the covariance matrix is of a high dimension, proportional to the number of time slices and the dimension of the correlation matrix, instabilities can occur, as mentioned above. Furthermore, in order to extract excited states, a fit of the data to a sum of exponentials with unknown exponents and coefficients has to be performed. It is a known problem [61, 62] that this fit may be very badly conditioned. Small changes in the data can cause large changes in the best-fit parameters. In order to circumvent these issues, a variational analysis can be performed.

### 3.4.2 Variational techniques and GEVP

The study of excited states on the lattice is intricate, because the excited states in correlation functions are exponentially suppressed in comparison to the ground state, as can be seen in equation (3.4). For the systematic and efficient extraction of excited states, the variational method is very effective. The main idea is to use a basis of several different interpolators and exploit the different overlaps onto the states of interest to extract the eigenvalues by solving the generalized eigenvalue problem (GEVP) [63–65]. The starting point is the matrix of cross correlations defined on an infinite-time lattice given in equation (3.6)

$$C_{ij}(t) = \langle \mathcal{O}_i(t) \bar{\mathcal{O}}_j(0) \rangle = \sum_{n=1}^{\infty} \langle 0 | \mathcal{O}_i | n \rangle \langle n | \mathcal{O}_j^\dagger | 0 \rangle e^{-E_n t}, \quad (3.48)$$

where a set of  $N$  basis interpolators  $\mathcal{O}_i$ ,  $i = 1, \dots, N$  is needed. Note that non degenerate energy-levels are assumed. As mentioned above, the interpolators must have the quantum numbers of the state to be examined. They can for instance be built from different Dirac structures or using different smearings.

The GEVP is defined by

$$C(t) v_n(t, t_0) = \lambda_n(t, t_0) C(t_0) v_n(t, t_0), \quad n = 1, \dots, N, \quad t > t_0, \quad (3.49)$$

where  $\lambda_n$  and  $v_n$  are the eigenvalues and orthonormal eigenvectors of the correlation matrix,

respectively. The matrix is of dimension  $N_{\text{op}} \times N_{\text{op}}$ , where  $N_{\text{op}}$  is the number of operators. The GEVP is solved by

$$\lambda_n(t, t_0) = \exp(-E_n(t - t_0)), \quad (3.50)$$

so that the energies of interest can now be determined [65]

$$E_n = \lim_{t \rightarrow \infty} E_n^{\text{eff}}(t, t_0) \quad (3.51)$$

$$E_n^{\text{eff}}(t, t_0) = \frac{1}{a} \ln \frac{\lambda_n(t, t_0)}{\lambda_n(t + a, t_0)}. \quad (3.52)$$

For large times, the contribution of states  $n > N$  is small and for fixed  $t_0$ , the corrections are given by

$$E_n^{\text{eff}}(t, t_0) = E_n + \epsilon(t, t_0) \quad (3.53)$$

$$\epsilon(t, t_0) = \mathcal{O}(e^{-\Delta E_n t}), \quad \Delta E_n = \min_{m \neq n} |E_m - E_n|. \quad (3.54)$$

The energy gap  $\Delta E_n$  is given by the distance to the nearest neighboring energy in the spectrum. So it is possible to obtain excited levels with corrections that vanish in the limit of large  $t$ , keeping  $t_0$  fixed. If the next energy level lies close to the one examined, corrections can be large. So one has to go to larger values of  $t$ , which is usually impractical, because the noise-to-signal ratio increases with  $t$ .

Since this situation occurs in the case of string breaking, special attention has to be paid. Fortunately, it was found that in practice [66, 67] the corrections appeared to be very small despite the above formula. In [63], it was pointed out, that the situation

$$t_0 \geq \frac{t}{2}, \quad (3.55)$$

is especially useful. It can be shown that under this precondition, the corrections are given by

$$\epsilon(t, t_0) = \mathcal{O}(e^{-\Delta E_{m,n} t}), \quad \Delta E_{m,n} = E_m - E_n, \quad (3.56)$$

where  $\Delta E_{m,n}$  is governed by the first energy value  $E_m$ ,  $m = N_{\text{op}} + 1$  lying above the  $N_{\text{op}}$  lowest states of interest. This large gap can solve the problem for close energy levels and also speed up the general convergence.

Performing the GEVP on every time-slice may introduce ambiguities between closely spaced levels at different times. In order to control this, we instead solve the GEVP for a fixed pair of a reference time separation  $t_0$  and another separation  $t_d$  at which the correlation matrix is diagonalized. Optimal interpolators, designed to have maximal overlap with a single

eigenstate, can be defined as

$$\hat{C}_{ij} = (v_i(t_0, t_d), C(t)v_j(t_0, t_d)), \quad (3.57)$$

where the parentheses denote an inner product over GEVP indices. The diagonalization is performed on the mean, because otherwise ambiguities might be introduced due to closely spaced levels on different bootstrap samples. The problem of ambiguities is avoided, but using the fixed GEVP, a potential source of systematic error is introduced resulting from the fact that the off-diagonal elements of  $C_{ij}$  are not exactly zero. In order to assess and control this, the GEVP is done using different pairs  $(t, t_0)$ , as well as by including different operators in the GEVP. Usually, the systematic effects due to varying the fitting range  $[t_{\min}, t_{\max}]$ , in particular  $t_{\min}$ , are the largest. To ensure stability of the results, we use sliding window plots, where the fitted mass is plotted as a function of  $t_{\min}$ . A plateau region indicates that the mass is stable as a function of  $t_{\min}$ . The plateaus also need to be stable for different  $t_{\max}$  and the chosen  $[t_{\min}, t_{\max}]$  needs to have a suitable correlated  $\chi^2$  per degrees of freedom (Dof).

The diagonal elements of the rotated correlation matrix are given by single exponentials up to corrections. Hence, it is possible to obtain the spectrum from a two-parameter correlated fit to a single-exponential ansatz. All fits to correlated data in this work minimize a correlated  $\chi^2$ . As a means of propagating statistical errors and getting robust estimates of uncertainties, we use bootstrap resampling [68, 69]. The bootstrap error estimation is used for all fits and also to estimate the covariance matrix. The estimate of the covariance matrix is kept fixed on each bootstrap sample.  $N_b = 800$  Bootstrap resamples of the correlation functions, which are reweighted according to equation (2.38), are employed and the uncertainty quoted for numerical values is given by  $1\sigma$  Bootstrap error bars.

In the case of the string breaking spectrum, we are interested in the difference between the energies of the ground, first and second excited state and twice the energy of the static-light meson. This offers the possibility of using ratio fits in order to extract the energies. If correlations between weakly-interacting two static-light meson and single static-light meson correlation functions are taken into account, this allows for a more precise extraction of the energy difference. We find that there are beneficial correlations present, not only for the states including two static-light as well as containing two static-strange meson correlations. It is important to do the Bootstrap resampling in exactly the same way for all primary observables to preserve these correlations and obtain correct error estimates. In order to do

ratio fits similar to what was done in [70], we define the ratio

$$R_n(t) = \frac{\hat{C}_n(t)}{C_B^2(t)}, \quad (3.58)$$

where  $C_B(t)$  is the correlation function of the static-light meson and  $\hat{C}_n(t)$  is the n-th diagonal element of the rotated correlation matrix

$$\hat{C}_n(t) = (v_n(t_0, t_d), C(t)v_n(t_0, t_d)). \quad (3.59)$$

When performing the fixed GEVP, the generalized eigenvectors  $v_n$  are determined for one combination  $(t_0, t_d)$  only. The ratio  $R(t)$  is constructed on each bootstrap sample and an energy difference  $\Delta E_n$  is extracted directly using single-exponential fits of the form  $R_n(t) = A \exp(-\Delta E_n t)$ . The fitted energies typically vary little as diagonalization times  $(t_0, t_d)$  or operator basis are varied. The energy  $E_n$  can be retrieved via

$$aE_n = a\Delta E_n + a2E_{m_B} \quad (3.60)$$

with  $E_{m_B}$  the mass of the static-light meson. Note that the excited state contamination in ratio fits may be non-monotonic.





## Chapter 4

# String breaking

The first part of this chapter gives a short review of string breaking in the literature and the second part introduces static quarks on the lattice. In section 4.3 the symmetries of string breaking on the lattice are discussed. The rest of this chapter focuses on the string breaking mixing analysis with a detailed description of the mixing matrix in section 4.5.

### 4.1 A short history of string breaking

Consider the potential between a static quark  $Q$  at spatial position  $\mathbf{x}$  and a static antiquark  $\bar{Q}$  at position  $\mathbf{y}$ , separated by a distance  $r = |\mathbf{y} - \mathbf{x}|$ . The static potential  $V(r)$  is defined as the energy of the ground state of this system [14]. As a consequence of confinement, the energy between the quark-antiquark pair is contained inside a color flux tube, the so called string.

$$Q(\mathbf{x}, t) \cdot \text{—————} \cdot \bar{Q}(\mathbf{y}, t)$$

FIGURE 4.1: Pictorial representation of the string between a quark and an antiquark.

As will be shown in section 4.5, the temporal correlation function of this string is given by the Wilson loop  $W$ , which thus serves as an observable for the static potential via

$$\langle W(t, r) \rangle \propto e^{-V_Q \bar{Q} t}. \quad (4.1)$$

If no pair creation from the vacuum is allowed, a functional form of the static potential is well described by the Cornell parametrization [71]

$$\hat{V}(r) = \frac{B}{r} + \sigma r + A, \quad (4.2)$$

where  $A$  is a constant and the second term is the so called Coulomb term with strength  $B$ , the third contribution is a linearly rising term, where  $\sigma$  is the so called string tension. This model is only applicable for intermediate distances.

A linearly rising term in the potential indicates that the energy between the static quark and static antiquark keeps rising as they are being pulled apart. This suggests that the two static quarks are confined within a strongly bound meson state. This is only true as long as no pair creation from the vacuum is allowed. In the full theory with dynamical quarks in the fundamental representation, processes of pair creation become important. It is expected that as soon as the energy is high enough, the gluonic string connecting the quarks breaks due to creation of a pair of light quarks  $q\bar{q}$ , which combine with the static quarks into two static-light mesons  $B = q\bar{Q}$  and  $\bar{B} = \bar{q}Q$ . This is the case as when  $[V(r) - 2E_{m_B}] > 0$ , where  $E_{m_B}$  is the energy of a static-light meson.

To explore string breaking on the lattice, the Wilson loop was used as an observable. The breaking of the string should manifest itself by rendering the potential constant above a certain threshold. The potential exhibits screening after the string is broken and saturates towards  $2E_{m_B}$ . But this phenomenon could not be observed, even if the potential was calculated for distances bigger than the estimated string breaking distance, see for example [72,73]. There are several reasons for this. One problem is the weak signal to noise ratio for distances greater than 1fm as well as the fundamental problem of lattice size. To observe where the string breaks, the lattice should have a size  $L > 2r_b$ , where  $L$  is the lattice extent and  $r_b$  the string breaking distance. The most important reason for the lack of evidence for string breaking using Wilson loops is that the Wilson line operator has a very small overlap with the ground state after the string is broken.

An analysis of the problem suggested that string breaking is a mixing phenomenon. This means that the two states, the string described by a Wilson line  $|Q\bar{Q}\rangle$  and the two meson state  $|B\bar{B}\rangle$ , are both needed to describe the potential. After the string is broken, the meson state is the new ground state of this system. In the neighborhood of the critical separation, the two states mix. Without mixing there would occur a plain level crossing of the two states. If there is mixing, the ground state  $|1\rangle$  and first excited state  $|2\rangle$  are superpositions of the string state  $|Q\bar{Q}\rangle$  and the two meson state  $|B\bar{B}\rangle$ . The system undergoes an avoided level crossing, giving rise to an energy gap  $\Delta E$  between the states  $|1\rangle$  and  $|2\rangle$ .

A model for  $SU(n)$  string breaking on the lattice in terms of strong coupling ideas was formulated in [74], it showed string breaking as a mixing phenomenon between the string and the two meson state. It was predicted that the width of the mixing region is sensitive to the mass of the sea quarks, for a lighter quark mass the energy gap becomes larger and the mixing region broadened. First experiments on the lattice were conducted using the three dimensional [75] and four dimensional [66,67]  $SU(2)$  Higgs model, because of the cost of

full QCD calculations. The  $SU(2)$  Higgs model has a confinement region that is very similar to QCD, a linearly rising potential of static color charges and eventual screening through pair creation. For this model clear evidence of string breaking was found. In [76] the static potential was analyzed for QCD with  $N_f=2$  quark flavors with the sea quark mass slightly below the mass of the strange quark and for one lattice spacing. In this case again clear evidence was found for string breaking.

To examine the ground state and first excited state of the static potential as a mixing phenomenon, their energies are determined by a variational technique from a correlation matrix. If the interpolators  $\mathcal{O}_W$  and  $\mathcal{O}_{B\bar{B}}$  correspond to the string state and the state consisting of two static-light mesons respectively, the matrix is schematically given by

$$\begin{aligned}
 C(t) &= \begin{pmatrix} C_{Q\bar{Q}} = \langle \mathcal{O}_W(t) \bar{\mathcal{O}}_W(0) \rangle & C_{B\bar{Q}} = \langle \mathcal{O}_{B\bar{B}}(t) \bar{\mathcal{O}}_W(0) \rangle \\ C_{Q\bar{B}} = \langle \mathcal{O}_W(t) \bar{\mathcal{O}}_{B\bar{B}}(0) \rangle & C_{B\bar{B}} = \langle \mathcal{O}_{B\bar{B}}(t) \bar{\mathcal{O}}_{B\bar{B}}(0) \rangle \end{pmatrix} \\
 &= \begin{pmatrix} \square & \sqrt{N_f} \times \begin{array}{c} \text{wavy} \\ \square \end{array} \\ \sqrt{N_f} \times \begin{array}{c} \square \\ \text{wavy} \end{array} & N_f \times \begin{array}{c} \text{wavy} \\ \square \end{array} + \begin{array}{c} \text{wavy} \\ \text{wavy} \end{array} \end{pmatrix}. \tag{4.3}
 \end{aligned}$$

The diagonal entries correspond to the string and the two meson state. There are  $N_f$  numbers of mass degenerate sea quark flavors. The wiggly lines correspond to light quark propagators. Mixing occurs when the physical energy eigenstates are not unit vectors in the original operator basis, it is shown explicitly by non vanishing off-diagonal elements. The elements of this matrix, as well as the inclusion of the strange quark, are discussed in more detail below.

## 4.2 Static quarks on the lattice

Heavy quark effective theory (HQET) is an effective formulation of QCD describing the physics of heavy quarks. It starts from the static approximation describing the theory as  $m_b \rightarrow \infty$ , where  $m_b$  is the heavy quark mass, corrections  $O(1/m_b)$  are computed using a  $1/m_b$  expansion [77,78]. The action of the static quark is written in terms of the quark  $\Psi_h$  and antiquark fields  $\bar{\Psi}_h$  satisfying the following properties under projection

$$\begin{aligned}
 P_+ \Psi_h &= \Psi_h, & \bar{\Psi}_h P_+ &= \bar{\Psi}_h \\
 P_- \bar{\Psi}_h &= \bar{\Psi}_h, & \bar{\Psi}_h P_- &= \bar{\Psi}_h,
 \end{aligned} \tag{4.4}$$

with projectors

$$P_{\pm} = \frac{1 \pm \gamma_4}{2}. \quad (4.5)$$

We are using the Dirac-Pauli representation for the gamma matrices, see Appendix A1, in which  $P_+$  and  $P_-$  are diagonal. In this case  $\Psi_h$  and  $\bar{\Psi}_h$  are four component fields with two components vanishing.

The leading order term of HQET is called static quark theory, where one assumes that the heavy quark is infinitely heavy. The static Lagrangian is given by

$$\mathcal{L}^{stat} = \mathcal{L}_h^{stat} + \mathcal{L}_{\bar{h}}^{stat} \quad (4.6)$$

$$\mathcal{L}_h^{stat} = \frac{1}{1 + a\delta m} \bar{\Psi}_h (m + D_4) \Psi_h,$$

$$\mathcal{L}_{\bar{h}}^{stat} = \frac{1}{1 + a\delta m} \bar{\Psi}_{\bar{h}} (m - D_4) \Psi_{\bar{h}}, \quad (4.7)$$

The static term provides a limit of the theory which is renormalizable.

### 4.2.1 Static propagator

The static propagator  $D_Q^{-1}$  we use is a modification of the static propagator derived by Eichten and Hill [79]. In [80] it was proven that using actions with HYP-smearred links improves the signal-to-noise ratio at large Euclidean times. The generalized action for the quark fields, derived in [80] has the following form

$$S_h^W = a^4 \frac{1}{1 + a\delta m_W} \sum_x \bar{\Psi}_h(x) (D_0^W + \delta m_W) \Psi_h(x), \quad (4.8)$$

with the covariant derivative

$$D_0^W \Psi_h(x) = \frac{1}{a} \left[ \Psi_h(x) - W^\dagger(x - a\hat{0}, 0) \Psi_h(x - a\hat{0}) \right], \quad (4.9)$$

where  $W(x, 0)$  is a gauge parallel transporter with the gauge transformation properties of the link  $U(x, 0)$  and  $\delta m_W$  cancels the divergence in the self-energy of the static quark. Analogous expressions can be written down for the antiquark fields. The static Eichten-Hill action

is retrieved for  $W(x, 0) = U(x, 0)$ . The corresponding quark propagator  $D_Q^{-1}(y, x)$  and anti-quark propagator  $D_{\bar{Q}}^{-1}(y, x)$  are given by

$$\begin{aligned} D_Q^{-1}(y, x) &= \theta(x_4 - y_4) \delta(\mathbf{x} - \mathbf{y}) (1 + a \delta m_W)^{-(x_4 - y_4)/a} \mathcal{P}^W(x, y)^\dagger P_+ , \\ D_{\bar{Q}}^{-1}(y, x) &= \theta(y_4 - x_4) \delta(\mathbf{x} - \mathbf{y}) (1 + a \delta m_W)^{-(y_4 - x_4)/a} \mathcal{P}^W(x, y) P_- , \\ \mathcal{P}^W(x, x) &= 1, \\ \mathcal{P}^W(x, x + R\hat{\mu}) &= W(x, \mu) W(x + a\hat{\mu}, \mu) \dots W(x + a(R-1)\hat{\mu}, \mu) \\ &\text{for } R > 0. \end{aligned} \tag{4.10}$$

$\delta m_W$  is set to 0 in this calculation, which results in an energy-shift for all energy-eigenvalues. Since the dependence of the correlation function on  $\delta m_W$  is known, it could be reinserted at any point.

The static propagator and anti-propagator are given by a time-like Wilson line projected onto upper or lower spin, the spatial position of the static quark or antiquark is fixed. We use HYP-smearred time-like Wilson lines. This amounts to a redefinition of the static action. In [80] statistically improved actions are proposed including the HYP-action which is used in our calculations

$$S_h^{\text{HYP2}} : W^{\text{HYP}}(x, 0) = V_{\text{HYP}}(x, 0), \tag{4.11}$$

where  $V_{\text{HYP}}(x, 0)$  is the HYP fat link as described in section 3.2.2 with HYP2 parameters

$$\alpha_1 = 1.0 \quad \alpha_2 = 1.0 \quad \alpha_3 = 0.5. \tag{4.12}$$

### 4.2.2 Renormalized static potential

The static theory with a Lagrangian of the form (4.6) gives rise to the power divergence in the static quark self-energy. The term  $\bar{\Psi} D_4 \Psi$  has the same quantum numbers as the lower dimensional mass operator  $\bar{\Psi} \Psi$  which leads to mixing of the two operators under renormalization with a linearly divergent coefficient [81, 82]. Differences between two energy levels however do not depend on  $\delta m_W$  and have a well defined continuum limit, because the divergences cancel each other. The divergences arising from the time-like Wilson lines affect the correlation function of the Wilson loop and the static-light meson. Because the Wilson loop has an exponential coefficient proportional to  $2t$  and the static-light meson proportional to  $t$ , the quantity

$$\Delta E = a[V(r) - 2E_{m_B}] \tag{4.13}$$

is free of divergences originating from self-energy contributions and defines the renormalized static potential.

Differences between potentials, where the self energy is already eliminated, have been shown [83] to have  $O(a^2)$  leading lattice artifacts. Using  $V(\infty) = 2E_{m_B}$  as before, this leads to

$$V(r) - 2E_{m_B} = V(r)^{\text{continuum}} - 2E_{m_B}^{\text{continuum}} + O(a^2). \quad (4.14)$$

This is true due to the fact that HQET is  $O(a)$ -improved without adding additional operators to the Lagrangian [84]. In a theory with dynamical fermions the statement holds only if the fermions are also  $O(a)$  improved, which is the case for the CLS ensembles.

### 4.3 Symmetries of string breaking

Two symmetries are present in continuum HQET, which are not symmetries in finite mass QCD. These are preserved on the lattice [84]. The static action (4.8) is invariant under  $SU(2)$  rotations

$$\Psi_h \rightarrow \exp(i\alpha_k \epsilon_{ijk} \sigma_{ij}) \Psi_h, \quad \bar{\Psi}_h \rightarrow \bar{\Psi}_h \exp(-i\alpha_k \epsilon_{ijk} \sigma_{ij}), \quad (4.15)$$

where  $\sigma_{jk}$  are the Pauli matrices and  $\alpha_i$  is an arbitrary real transformation parameter. This symmetry is called heavy quark spin symmetry, it means in the static limit there are no interactions involving the heavy quark spin. Mesons that only differ in the spin of their heavy quark are degenerate.

Furthermore, static quarks can only travel in time, they cannot propagate in space. This leads to the local conservation of heavy quark flavor number. The action is invariant under a transformations of this form

$$\Psi_h \rightarrow \exp(i\eta(x)) \Psi_h, \quad \bar{\Psi}_h \rightarrow \bar{\Psi}_h \exp(-i\eta(x)), \quad (4.16)$$

for any local phase  $\eta(x)$ . This symmetry leads to the proportionality of the static quark propagator to a lattice delta function in space.

As mentioned above, on a spatially isotropic lattice, the continuum symmetry is reduced to  $O_h \times \mathcal{T}_{latt}^3$ . The states transforming irreducibly under the irreps of  $O_h$  are labeled  $\Lambda^P$ . The observables we are interested in contain static quarks, their spatial positions are fixed, so the positions of the static quarks become additional quantum numbers of the system. The symmetry for  $r > 0$  is further broken down depending on  $r$ . For on-axis distances, the relevant

symmetry group for string breaking on the lattice is the cylindrical subgroup  $D_h$ . Since we are only interested in states with total spin  $S = 0, 1$  we use the continuum notation. The irreducible representations of the continuum group are identified by the spin along the axis  $L_z$ , where  $L_z = 0, 1, 2$  are usually named  $\Sigma, \Pi, \Delta$ .

In the static limit, the total angular momentum and parity of the light degrees of freedom become conserved quantities. Therefore, it is common [85,86] to label static-light mesons by parity  $\mathcal{P}$  and total angular momentum of the light degrees of freedom  $j$  with  $j = |l \pm 1/2|$ , where  $l$  denotes angular momentum and  $\pm 1/2$  the spin of the light quark. The total angular momentum of the static-light meson is either  $J = j + 1/2$  or  $J = j - 1/2$ , where both states have degenerate mass. Charge conjugation is not a good quantum number, since static-light mesons are made from non-identical quarks. For a system containing a heavy quark and anti quark, parity alone is not good quantum number, because it interchanges their positions. The combination of parity and charge conjugation  $\mathcal{CP}$  however is a good quantum number, we label it with a superscript  $g$  for  $\mathcal{CP} = +$ , or  $u$  for  $\mathcal{CP} = -$ . The spin 0 representations get an additional label, which describes  $\mathcal{R}$  parity, the behavior under reflections on a plane containing the endpoints, which is labeled  $\pm$ .

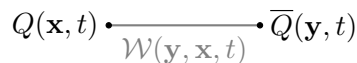
### 4.3.1 Interpolators

To investigate string breaking using a correlation matrix containing the interpolators for a Wilson loop as well as for the two static-light meson state, it is essential that the two states have the same symmetries and thus carry the same quantum numbers.

The four static quark and antiquark creation and annihilation operators, as described in section 4.2, can be obtained from two four-component spinors, which we name  $\bar{Q} = \bar{\Psi}\gamma_4$  and  $Q = \Psi$ . We consider a system containing a heavy quark  $Q(\mathbf{x}, t)$  at point  $(\mathbf{x}, t)$  and a heavy anti-quark  $\bar{Q}(\mathbf{y}, t)$  at point  $(\mathbf{y}, t)$  in the static approximation. They are separated by a distance  $r$ ,  $\mathbf{x}$  and  $\mathbf{y}$  are conserved quantum numbers. The interpolator  $\mathcal{O}_W$  corresponding to the string is given by

$$\mathcal{O}_W = \bar{Q}(\mathbf{y}, t)\Gamma\mathcal{W}(\mathbf{y}, \mathbf{x}, t)Q(\mathbf{x}, t), \quad (4.17)$$

where  $\Gamma$  is an operator that determines the spin structure.



$$Q(\mathbf{x}, t) \cdot \xrightarrow{\mathcal{W}(\mathbf{y}, \mathbf{x}, t)} \cdot \bar{Q}(\mathbf{y}, t)$$

FIGURE 4.2: pictorial representation of a Wilson line

$\mathcal{W}(\mathbf{y}, \mathbf{x}, t)$  is a Wilson-line, the path-ordered product of spatial, in our case HYP-smearred links connecting  $\mathbf{x}$  and  $\mathbf{y}$  along some path  $\mathbf{C}_{x,y}$  with all link variables restricted to time argument  $t$ . The combination (4.17) is gauge covariant and defined by

$$\mathcal{W}(\mathbf{y}, \mathbf{x}; t) = \prod_{(\mathbf{k}, i) \in \mathbf{C}_{\mathbf{x}, \mathbf{y}}} U_i(\mathbf{k}, t). \quad (4.18)$$

There are two possible situations, either the spins of the two quarks couple symmetrically or anti-symmetrically, corresponding to a total spin of  $S = 1$  and  $S = 0$  respectively.  $\Gamma = \gamma_i \cdot \mathbf{r}/r$  represents the symmetric combination, where  $\mathbf{r}$  is a three-vector. The antisymmetric combination is given by  $\Gamma = \gamma_5$  [76]. We use the symmetric spin state. The corresponding creation and annihilation operators are given by

$$\begin{aligned} \mathcal{O}_W(\mathbf{y}, \mathbf{x}, t) &= \bar{Q}(\mathbf{y}, t) \frac{\gamma \cdot \mathbf{r}}{r} \mathcal{W}(\mathbf{y}, \mathbf{x}, t) Q(\mathbf{x}, t) \\ \bar{\mathcal{O}}_W(\mathbf{y}, \mathbf{x}, t) &= -\bar{Q}(\mathbf{x}, t) \frac{\gamma \cdot \mathbf{r}}{r} \mathcal{W}(\mathbf{x}, \mathbf{y}, t) Q(\mathbf{y}, t) \quad . \end{aligned} \quad (4.19)$$

It lies within the ground state representation of the corresponding symmetry group  $\Sigma_g^+$ , if it is combined with a symmetric gluonic string  $\mathcal{W}(\mathbf{y}, \mathbf{x}; t)$ . The antisymmetric combination  $\gamma_5$  lies within  $\Sigma_u^-$ . In the static limit, the quarks spins decouple and thus the two states yield degenerate energy levels, the symmetric and antisymmetric interpolators lead to the same expression for the Wilson loop. Note that since the string state does not contain any light quarks, trivially it has isospin  $I = 0$ .

The lightest static-light meson has light quark quantum numbers  $J^P = \frac{1}{2}^-$  [87, 88]. In combination with the static quark this yields mass degenerate pseudoscalar and vector states. Two of these states can be combined to have  $\mathcal{CP} = +$  and lie within the  $\Sigma_g^+$  representation. Consider mass-degenerate flavors of light quarks  $q_i, i = 1, \dots, N_f$ . The smeared light quark fields are defined as  $q_{a\alpha}^i(\mathbf{x}, t) = \tilde{\psi}_{a\alpha}^{(i)}$ , the antiquark fields as  $\bar{q}_{a\alpha}^i(\mathbf{x}, t) = \tilde{\psi}_{a\alpha}^{(i)} \gamma_4$ , where  $a$  is a color index,  $\alpha$  is a Dirac spin component and  $i$  is a quark flavor.  $\tilde{\psi}$  are LapH-smearred quark fields. All indices not immediately important for the calculation are omitted. Using for example the symmetric string state together with the pseudoscalar state for the static-light meson, the interpolators for a static-light meson and a two static-light meson state are given by

$$\begin{aligned} \mathcal{O}_B(\mathbf{x}, t) &= \frac{1}{\sqrt{N_f}} \sum_i \bar{Q}(\mathbf{x}, t) \gamma_5 q^i(\mathbf{x}, t) \\ \mathcal{O}_{BB}(\mathbf{x}, \mathbf{y}, t) &= \frac{1}{\sqrt{N_f}} \sum_i \bar{Q}(\mathbf{y}, t) \gamma_5 q^i(\mathbf{y}, t) \bar{q}^i(\mathbf{x}, t) \gamma_4 \gamma_5 Q(\mathbf{x}, t), \end{aligned} \quad (4.20)$$



where the sum is taken over degenerate quark flavors. For the two static-light meson state, the sum amounts to a projection onto the isospin  $I = 0$  channel.

This choice for the string and two static-light meson state yields trial states falling into  $\Sigma_g^+$ . As already noted in [76], choosing to start from the  $\Sigma_u^-$  sector leads to identical correlation functions as it should be in the static mass limit. The same is true for the choice of combining two vector states in the symmetric sector.

## 4.4 First steps towards string breaking

An estimate of the string breaking distance  $r_b$  can be calculated utilizing  $E_{m_b}$ , the mass of the static-light meson, and the static potential  $V(r)$  calculated from Wilson loops only.  $E_{m_b}$  is also needed to obtain a renormalized potential as given in equation (4.14). These are the first steps towards a full mixing analysis.

### 4.4.1 Static-light meson

Using the interpolators

$$\begin{aligned}\mathcal{O}_B(\mathbf{x}, t) &= \frac{1}{\sqrt{N_f}} \sum_i \bar{Q}(\mathbf{x}, t) \gamma_5 q^i(\mathbf{x}, t) \\ \bar{\mathcal{O}}_B(\mathbf{x}, t) &= \frac{1}{\sqrt{N_f}} \sum_i \bar{q}^i(\mathbf{x}, t) \gamma_4 \gamma_5 Q(\mathbf{x}, t),\end{aligned}\tag{4.21}$$

the correlation function for a static-light meson reads

$$\begin{aligned}C(t) &= \sum_{\mathbf{x}} \left\langle \left[ \mathcal{O}_B(\mathbf{x}, t) \bar{\mathcal{O}}_B(\mathbf{x}, 0) \right] \right\rangle \\ &= \frac{1}{N_f} \sum_{i, \mathbf{x}} \left\langle \left[ \bar{Q}(\mathbf{x}, t) \gamma_5 q^i(\mathbf{x}, t) \bar{q}^i(\mathbf{x}, 0) \gamma_4 \gamma_5 Q(\mathbf{x}, 0) \right] \right\rangle.\end{aligned}\tag{4.22}$$

Due to the use of all-to-all propagators, the correlator can be calculated for all spatial sites  $\mathbf{x}$  simultaneously to improve statistics by fully exploiting translational invariance. After Wick contraction one finds

$$\begin{aligned}C(t) &\stackrel{Wick}{=} \sum_{\mathbf{x}} \left\langle \text{Tr}_{c,d} \left( -\gamma_5 \underbrace{\mathcal{D}(\mathbf{x}, t; \mathbf{x}; 0)}_{\text{light propagator}} \gamma_5 \underbrace{\mathcal{P}(0, t) P_-}_{\text{static propagator}} \right) \right\rangle \\ &= \sum_{\mathbf{x}} \left\langle \text{Tr}_{c,d} \left( -\mathcal{D}(\mathbf{x}, t; \mathbf{x}; 0) \gamma_4 \mathcal{P}(0, t) P_+ \right) \right\rangle,\end{aligned}\tag{4.23}$$

where the trace is taken over color and Dirac indices.  $\mathcal{P}(0, t)$  is a timelike Wilson-line of HYP-smearred links from  $(x, t)$  to  $(x, 0)$ , the projector  $P_{\pm}$  is given by equation (4.5). As mentioned above, this is a modification of the Eichten-Hill static propagator. For the gamma matrices the following relations were used:

$$\begin{aligned} \gamma_5^2 &= \mathbf{1} & (\gamma_5)^\dagger &= \gamma_5 & \gamma_5 P_+ &= P_- \gamma_5 \\ \gamma_4^2 &= \mathbf{1} & (\gamma_4)^\dagger &= \gamma_4 \end{aligned} \quad (4.24)$$

The light quark line is stochastically estimated as given in equation (3.42), where  $\sum_{\mathbf{x}, r, b}$  is a shorthand for summation over all spatial sites as well as over  $N_R$  and  $N_b$ , the sets of independent stochastic noise sources and the number of dilution projectors respectively. The correlation function written in terms of source and sink is given by

$$\begin{aligned} C(t) &= \frac{1}{N_R} \sum_{\mathbf{x}, r, b} \left\langle \text{Tr}_{c,d} \left( - \underbrace{[S\Omega^{-1}VP^{(b)}\rho^r]}_{\text{sink}}(\mathbf{x}, t) \underbrace{(VP^{(b)}\rho^r)^\dagger}_{\text{source}}(\mathbf{x}, t) \gamma_4 \mathcal{P}(0, t) P_+ \right) \right\rangle \\ &= \frac{1}{N_R} \sum_{\mathbf{x}, r, b} \left\langle \text{Tr}_{c,d} \left( -\varphi^{r[b]}(\mathbf{x}, t) \varrho^{r[b]\dagger}(\mathbf{x}, 0) (\gamma_4 \mathcal{P}(0, t) P_+) \right) \right\rangle \\ &= \frac{1}{N_R} \sum_{\mathbf{x}, r, b} \left\langle -\varrho^{r[b]*}(\mathbf{x}, 0) \cdot (\mathcal{P}(0, t) P_+ \varphi^{r[b]})(\mathbf{x}, t) \right\rangle. \end{aligned} \quad (4.25)$$

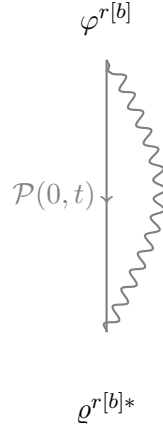


FIGURE 4.3: Pictorial representation of the static-light meson.

Now we have to compute just a scalar product of source and sink vector in spin and color indices with an inserted timelike Wilson-line, projected onto upper spin components. For the static-strange quark, the calculation is analogous.

As already pointed out, using static quarks that are not stochastically estimated means that we can not contract the source and sink a posteriori, as is usually possible with stochastic LapH. It is still possible to reuse quark sinks, once computed and stored, in different diagrams or for completely different calculations. Furthermore, the outer product structure allows for an effective evaluation using dot products for the relevant diagrams for string breaking, similar to the above diagram of the static-light meson.

## 4.5 Correlation Matrix $C_{ij}$

As the next step towards performing the full mixing analysis, the correlation matrix  $C_{ij}$  as given in equation (4.3) has to be evaluated, which means the correlators for the different diagrams have to be calculated. The following sections provide all necessary details for each diagram. The chosen creation and annihilation operators used to form the correlation functions lead to a hermitian mixing matrix and yield positive correlators for the diagonal elements.

### 4.5.1 Calculation of $C_{11}$ , Wilson-loop

As promised, it is shown now that the time correlation function of the string state yields a Wilson loop. For the correlation function reads

$$\begin{aligned} C_{11}(r, t) &= \sum_{\mathbf{x}} \left\langle \mathcal{O}_W(\mathbf{x}, \mathbf{y}, t) \overline{\mathcal{O}}_W(\mathbf{x}, \mathbf{y}, 0) \right\rangle \\ &= \sum_{\mathbf{x}} \left\langle -\overline{Q}(\mathbf{y}, t) \frac{\boldsymbol{\gamma} \cdot \mathbf{r}}{r} \mathcal{W}(\mathbf{y}, \mathbf{x}, t) Q(\mathbf{x}, t) \overline{Q}(\mathbf{x}, 0) \frac{\boldsymbol{\gamma} \cdot \mathbf{r}}{r} \mathcal{W}(\mathbf{x}, \mathbf{y}, 0) Q(\mathbf{y}, 0) \right\rangle \end{aligned} \quad (4.26)$$

The correlator can be calculated for all spatial sites  $\mathbf{x}$  simultaneously, where we keep  $\mathbf{r} = \mathbf{x} - \mathbf{y}$  fixed. After Wick contraction it becomes apparent that element  $C(1,1)$  of the correlation matrix is a Wilson loop

$$\begin{aligned} C_{11}(r, t) &\stackrel{Wick}{=} \sum_{\mathbf{x}} \left\langle \text{Tr}_{c,d} \left( \frac{\boldsymbol{\gamma} \cdot \mathbf{r}}{r} \mathcal{W}(\mathbf{y}, \mathbf{x}, t) \mathcal{P}_x(t, 0) P_+ \frac{\boldsymbol{\gamma} \cdot \mathbf{r}}{r} \mathcal{W}(\mathbf{x}, \mathbf{y}, 0) \mathcal{P}_y(0, t) P_- \right) \right\rangle \\ &= \sum_{\mathbf{x}} \left\langle \text{Tr}_{c,d} \left( \gamma_i \mathcal{W}(\mathbf{y}, \mathbf{x}, t) \mathcal{P}_x(t, 0) P_+ \gamma_j \mathcal{W}(\mathbf{x}, \mathbf{y}, 0) \mathcal{P}_y(0, t) P_- \right) \right\rangle \\ &= 2 \sum_{\mathbf{x}} \left\langle \text{Tr}_c \left( \mathcal{W}(\mathbf{y}, \mathbf{x}, t) \mathcal{P}_x(t, 0) \mathcal{W}(\mathbf{x}, \mathbf{y}, 0) \mathcal{P}_y(0, t) \right) \right\rangle, \end{aligned} \quad (4.27)$$

The trace is taken over color only in the last line, which can be derived by using the identity  $\text{Tr}(P_+ \gamma_i P_- \gamma_j) = \delta_{ij} \text{tr}(P^2) = 2\delta_{ij}$ .

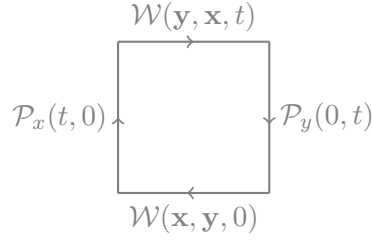


FIGURE 4.4: pictorial representation of the Wilson loop

### 4.5.2 Calculation of $C_{22}$

The interpolators for the state consisting of two static-light mesons are

$$\begin{aligned}\mathcal{O}_{B\bar{B}}(\mathbf{x}, \mathbf{y}, t) &= \frac{1}{\sqrt{N_f}} \sum_{i, \mathbf{x}} \bar{Q}(\mathbf{y}, t) \gamma_5 q^i(\mathbf{y}, t) \bar{q}^i(\mathbf{x}, t) \gamma_4 \gamma_5 Q(\mathbf{x}, t) \\ \bar{\mathcal{O}}_{B\bar{B}}(\mathbf{x}, \mathbf{y}, t) &= \frac{1}{\sqrt{N_f}} \sum_{i, \mathbf{x}} \bar{Q}(\mathbf{x}, t) \gamma_5 q^i(\mathbf{x}, t) \bar{q}^i(\mathbf{y}, t) \gamma_4 \gamma_5 Q(\mathbf{y}, t).\end{aligned}\quad (4.28)$$

The correlation function for the matrix element  $C_{22}(t)$  containing two static-light mesons reads

$$\begin{aligned}C_{22}(r, t) &= \sum_{\mathbf{x}} \langle \mathcal{O}_{B\bar{B}}(\mathbf{x}, \mathbf{y}, t) \bar{\mathcal{O}}_{B\bar{B}}(\mathbf{x}, \mathbf{y}, 0) \rangle \\ &= \frac{1}{N_f} \sum_{i, j, \mathbf{x}} -\langle \gamma_5 q^i(\mathbf{y}, t) \bar{q}^i(\mathbf{x}, t) \gamma_4 \gamma_5 Q(\mathbf{x}, t) \bar{Q}(\mathbf{x}, 0) \gamma_5 q^j(\mathbf{x}, 0) \bar{q}^j(\mathbf{y}, 0) \gamma_4 \gamma_5 Q(\mathbf{y}, 0) \bar{Q}(\mathbf{y}, t) \rangle.\end{aligned}\quad (4.29)$$

After Wick-contraction we find

$$C_{22}(r, t) \stackrel{Wick}{=} N_f \sum_{\mathbf{x}} \left\langle -\text{Tr}_{c,d} \left( \gamma_5 \mathcal{D}(\mathbf{y}, t; \mathbf{x}; t) \gamma_4 \gamma_5 \mathcal{P}_x(t, 0) P_+ \gamma_5 \mathcal{D}(\mathbf{x}, 0; \mathbf{y}; 0) \gamma_4 \gamma_5 \mathcal{P}_y(0, t) P_- \right) \right\rangle \quad (4.30)$$

$$+ \delta_{ij} \left\langle \text{Tr}_{c,d} \left[ \gamma_5 \mathcal{D}(\mathbf{y}, t; \mathbf{y}; 0) \gamma_4 \gamma_5 \mathcal{P}^y(0, t) P_- \right] \text{Tr}_{c,d} \left[ \gamma_5 \mathcal{D}(\mathbf{x}, 0; \mathbf{x}; t) \gamma_4 \gamma_5 \mathcal{P}^x(t, 0) P_+ \right] \right\rangle$$

$$= N_f \sum_{\mathbf{x}} \left\langle \text{Tr}_{c,d} \left[ P_+ \mathcal{D}(\mathbf{y}, t; \mathbf{x}; t) \mathcal{P}^x(t, 0) P_- \mathcal{D}(\mathbf{x}, 0; \mathbf{y}; 0) \mathcal{P}^y(0, t) \right] \right\rangle \quad (4.31)$$

$$- \delta_{ij} \left\langle \text{Tr}_{c,d} \left[ P_+ \mathcal{D}(\mathbf{y}, t; \mathbf{y}; 0) \mathcal{P}^y(0, t) \right] \text{Tr}_{c,d} \left[ P_- \mathcal{D}(\mathbf{x}, 0; \mathbf{x}; t) \mathcal{P}^x(t, 0) \right] \right\rangle$$

The trace is taken over color and Dirac indices. Relations (4.24) were used, as well as

$$\gamma_4 P_+ = P_+ \quad \gamma_4 P_- = -P_- \quad (4.32)$$

The connected part reads

$$\begin{aligned} C_{22}^{conn}(r, t) &= \frac{N_f}{N_R} \sum_{\mathbf{x}, r, b} \langle \text{Tr}_{c,d} \left[ P_+ \underbrace{[S\Omega^{-1}VP^{(a)}\rho^r](\mathbf{y}, t)}_{\text{sink}} \underbrace{(VP^{(a)}\rho^r)^\dagger(\mathbf{x}, t)}_{\text{source}} \mathcal{P}^x(t, 0) \times \right. \\ &\quad \left. P_- \underbrace{[S\Omega^{-1}VP^{(b)}\rho^r](\mathbf{x}, 0)}_{\text{sink}} \underbrace{(VP^{(b)}\rho^r)^\dagger(\mathbf{y}, 0)}_{\text{source}} \mathcal{P}^y(0, t) \right] \rangle \\ &= \frac{N_f}{N_R} \sum_{\mathbf{x}, r, b} \langle \text{Tr}_{c,d} \left[ P_+ \varphi^{r[a]}(\mathbf{y}, t) \varrho^{r[a]\dagger}(\mathbf{x}, t) \mathcal{P}^x(t, 0) P_- \varphi^{r[b]}(\mathbf{x}, 0) \varrho^{r[b]\dagger}(\mathbf{y}, 0) \mathcal{P}^y(0, t) \right] \rangle \\ &= \frac{N_f}{N_R} \sum_{\mathbf{x}, r, b} \langle [\varrho^{r[a]*}(\mathbf{x}, t) \cdot (\mathcal{P}^x(t, 0) P_- \varphi^{r[b]}(\mathbf{x}, 0)) \quad \varrho^{r[b]*}(\mathbf{y}, 0) \cdot (\mathcal{P}^y(0, t) P_+ \varphi^{r[a]}(\mathbf{y}, t))] \rangle \end{aligned} \quad (4.33)$$

Similar to the static-light meson case, we find scalar products with insertions of Wilson lines, projected onto lower or upper spin components.

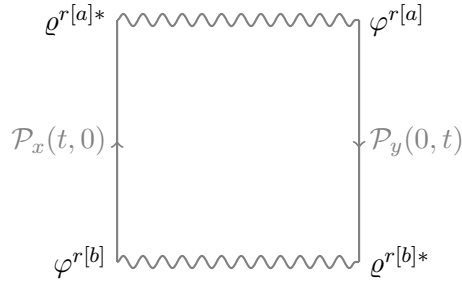


FIGURE 4.5: pictorial representation of the connected part of the correlation function  $C_{22}(r,t)$

Now turn to the disconnected part of the correlator, which only contributes for  $i = j$ . We skip diagonal noise combinations to get an unbiased estimate, for equal flavor indices

$$\begin{aligned}
C_{22}^{dis}(r, t) &= \frac{1}{N_R(N_R - 1)} \sum_{\substack{\mathbf{x}, b_1, b_2 \\ r_1 \neq r_2}} - \langle \text{Tr}_{c,d} \left[ P_+ \underbrace{[S\Omega^{-1}VP^{(b_1)}\rho^{r_1}](\mathbf{y}, t)}_{\text{sink}} \underbrace{(VP^{(b_1)}\rho^{r_1})^\dagger(\mathbf{y}, 0)}_{\text{source}} \mathcal{P}^y(0, t) \right] \right. \\
&\quad \times \left. \text{Tr}_{c,d} \left[ P_- \underbrace{[S\Omega^{-1}VP^{(b_2)}\rho^{r_2}](\mathbf{x}, 0)}_{\text{sink}} \underbrace{(VP^{(b_2)}\rho^{r_2})^\dagger(\mathbf{x}, t)}_{\text{source}} \mathcal{P}^x(t, 0) \right] \right\rangle \\
&= \frac{1}{N_R(N_R - 1)} \sum_{\substack{\mathbf{x}, b_1, b_2 \\ r_1 \neq r_2}} - \langle \text{Tr}_{c,d} \left[ \varrho^{r_1[b_1]^\dagger}(\mathbf{y}, t) \mathcal{P}^y(0, t) P_+ \varphi^{r_1[b_1]}(\mathbf{y}, 0) \right] \right. \\
&\quad \times \left. \text{Tr}_{c,d} \left[ \varrho^{r_2[b_2]^\dagger}(\mathbf{x}, 0) \mathcal{P}^x(t, 0) P_- \varphi^{r_2[b_2]}(\mathbf{x}, t) \right] \right\rangle \\
&= \frac{1}{N_R(N_R - 1)} \sum_{\substack{\mathbf{x}, b_1, b_2 \\ r_1 \neq r_2}} - \langle \left[ \varrho^{r_1[b_1]^*}(\mathbf{y}, t) \cdot \mathcal{P}^y(0, t) P_+ \varphi^{r_1[b_1]}(\mathbf{y}, 0) \right] \right. \\
&\quad \times \left. \left[ \varrho^{r_2[b_2]^*}(\mathbf{x}, 0) \cdot \mathcal{P}^x(t, 0) P_- \varphi^{r_2[b_2]}(\mathbf{x}, t) \right] \right\rangle
\end{aligned} \tag{4.34}$$

The disconnected part can be expressed in a more advantageous way for coding purposes:

$$\begin{aligned}
C_{22}^{dis}(r, t) &= \frac{1}{N_R(N_R - 1)} \sum_{\substack{\mathbf{x}, b_1, b_2 \\ r_1 \neq r_2}} \langle \left[ \varrho^{r_1[b_1]^*}(\mathbf{y}, t) \cdot \mathcal{P}^y(0, t) P_+ \varphi^{r_1[b_1]}(\mathbf{y}, 0) \right] \right. \\
&\quad \times \left. \left[ \varrho^{r_2[b_2]^*}(\mathbf{x}, t) \cdot \mathcal{P}^x(0, t) P_+ \varphi^{r_2[b_2]}(\mathbf{x}, 0) \right]^\dagger \right\rangle
\end{aligned} \tag{4.35}$$

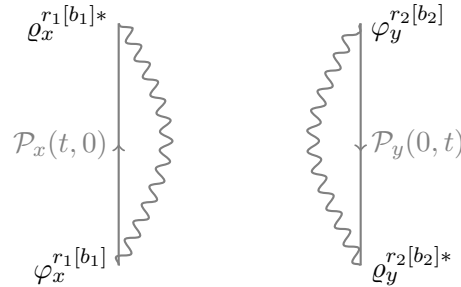


FIGURE 4.6: pictorial representation of the disconnected part for  $i=j$  of the correlation function  $C_{22}(\mathbf{r}, t)$

### 4.5.3 Calculation of $C_{12}, C_{21}$

The correlator in the off diagonal matrix elements can be found along the same lines as shown in detail for matrix element  $C_{22}(r, t)$ . The interpolators are given by a combination of a meson creation/annihilation operator and a string annihilation/creation operator.

$$\begin{aligned}
C_{12}(r, t) &= \sum_{\mathbf{x}} \langle \mathcal{O}_{B\bar{B}}(\mathbf{x}, \mathbf{y}, t) \bar{\mathcal{O}}_W(\mathbf{x}, \mathbf{y}, 0) \rangle \quad (4.36) \\
&= \frac{1}{\sqrt{N_f}} \sum_{i, \mathbf{x}} \langle -[\bar{Q}(\mathbf{y}, t) \gamma_5 q^i(\mathbf{y}, t) \bar{q}^i(\mathbf{x}, t) \gamma_4 \gamma_5 Q(\mathbf{x}, t)] [\bar{Q}(\mathbf{x}, 0) \frac{\boldsymbol{\gamma} \cdot \mathbf{r}}{r} \mathcal{W}(\mathbf{x}, \mathbf{y}, 0) Q(\mathbf{y}, 0)] \rangle \\
&= \sqrt{N_f} \sum_{i, \mathbf{x}} \langle \text{Tr}_{c,d} \left( P_- \frac{\boldsymbol{\gamma} \cdot \mathbf{r}}{r} \mathcal{D}(\mathbf{y}, t; \mathbf{x}; t) \mathcal{P}^x(t, 0) \mathcal{W}(\mathbf{x}, \mathbf{y}, 0) \mathcal{P}^y(0, t) \right) \rangle \\
&= \sqrt{N_f} \sum_{i, \mathbf{x}, b} \langle \varrho^{r[b]*}(\mathbf{x}, t) \cdot \left( \mathcal{P}^x(t, 0) \mathcal{W}(\mathbf{x}, \mathbf{y}, 0) \mathcal{P}^y(0, t) P_- \frac{\boldsymbol{\gamma} \cdot \mathbf{r}}{r} \varphi^{r[b]}(\mathbf{y}, t) \right) \rangle.
\end{aligned}$$

For the other off-diagonal element  $C_{21}(r, t)$  the spacetime points have to be changed accordingly, otherwise the calculation is identical. There is no need to compute both elements since

$$C_{12}(t) = \langle \mathcal{O}_{B\bar{B}} \bar{\mathcal{O}}_W \rangle = \langle \mathcal{O}_W \bar{\mathcal{O}}_{B\bar{B}} \rangle = C_{21}(t), \quad (4.37)$$

this leads to a hermitian mixing matrix.

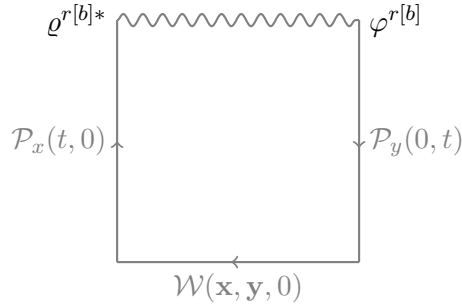


FIGURE 4.7: Pictorial representation of the off-diagonal element

### 4.5.4 Including the strange quark

If there is a strange quark included in the sea, the correlation matrix has to be enlarged accordingly. The strange quark is being treated similar to the other light degrees of freedom, but one has to keep in mind that there is just one strange quark, whereas the up-and down quarks are mass degenerate.

$$\begin{aligned}
C(r, t) = & \begin{pmatrix} C_{Q\bar{Q}} = \langle \mathcal{O}_W \bar{\mathcal{O}}_W \rangle & C_{B\bar{Q}} = \langle \mathcal{O}_{B\bar{B}} \bar{\mathcal{O}}_W \rangle & C_{B_s\bar{Q}} = \langle \mathcal{O}_{B_s\bar{B}_s} \bar{\mathcal{O}}_W \rangle \\ C_{Q\bar{B}} = \langle \mathcal{O}_W \bar{\mathcal{O}}_{B\bar{B}} \rangle & C_{B\bar{B}} = \langle \mathcal{O}_{B\bar{B}} \bar{\mathcal{O}}_{B\bar{B}} \rangle & C_{B\bar{B}_s} = \langle \mathcal{O}_{B\bar{B}} \bar{\mathcal{O}}_{B_s\bar{B}_s} \rangle \\ C_{B\bar{Q}} = \langle \mathcal{O}_{B\bar{B}} \bar{\mathcal{O}}_W \rangle & C_{B_s\bar{B}} = \langle \mathcal{O}_{B_s\bar{B}_s} \bar{\mathcal{O}}_{B\bar{B}} \rangle & C_{B_s\bar{B}_s} = \langle \mathcal{O}_{B_s\bar{B}_s} \bar{\mathcal{O}}_{B_s\bar{B}_s} \rangle \end{pmatrix} \\
& (4.38) \\
= & \begin{pmatrix} \square & \sqrt{2} \times \square & \square \\ \sqrt{2} \times \square & 2 \times \square + \begin{matrix} \text{wavy} \\ \text{line} \end{matrix} & \sqrt{2} \times \square \\ \square & \sqrt{2} \times \square & \square + \begin{matrix} \text{wavy} \\ \text{line} \end{matrix} \end{pmatrix}
\end{aligned}$$

The diagonal entries correspond to the string, the two static-light and static-strange meson state. The up and down quark are mass degenerate sea quark flavors. The wiggly lines correspond to light quark propagators. The correlation matrix can be further extended by including different levels of smearing.

Possible effects of including the strange quark have been discussed in [76]. The effect of the third quark flavor on the string breaking distance and mixing region is not a priori clear. There will be two separate thresholds corresponding to the decay of the string into a pair of static-light mesons and static-strange mesons, respectively. In general, the string breaking distance is expected to decrease with the sea quark mass and a lighter mass is expected to result in a larger gap as well as a broadened mixing region.

String breaking for  $N_f = 2 + 1$  flavors has not yet been investigated on the lattice. The numerical results of our study of the mixing phenomenon including the strange quark are discussed in the next chapter.



## Chapter 5

# Numerical results for string breaking

### 5.1 Ensemble details

In this chapter, we present the numerical results of our string breaking investigation using the stochastic LapH method. The set of ensembles in table 2.2 with  $N_f = 2 + 1$  flavors generated by the CLS effort [24, 89] provides an ideal playground to study the phenomenon. In this work, we employ one of the ensembles, the N200, for an exploratory study.

The measurements are done on a subset of evenly-spaced configurations of the N200 ensemble with  $N_f = 2 + 1$  flavors of non-perturbatively  $O(a)$ -improved Wilson fermions. The lattice-size is  $N_t \times N_s^3 = 128 \times 48^3$  with an estimated isotropic lattice spacing of  $a \approx 0.064$  fm and pion and kaon mass of  $m_\pi = 280$  MeV and  $m_K = 460$  MeV respectively [24]. Open temporal boundary conditions are imposed on the gauge field in the temporal direction, whose imprint on bulk observables is expected to decrease exponentially [90]. Within the stochastic LapH method, the covariant Laplace operator on each time slice of the lattice is used to define the smearing of the quark fields in interpolators and hence the correlation matrix is hermitian. Boundary effects in the Laplace operator effectively change the smearing and could lead to a non-hermitian correlation matrix. Figure 5.1 shows the smallest and largest eigenvalue retained in our smearing scheme on 26 evenly-spaced configurations of the N200. We employ sources and sinks far away from the temporal boundary in order to keep the smearing constant. Furthermore, we perform measurements on the central half of the lattice only. The specific parameters used for LapH smearing are given in table 5.1. They are chosen in a way that they result in a similar physical smearing to previous studies [53].

id	$N_{ev}$	$n_\rho \times \rho$	line type	dilution scheme	$N_r$ light/strange	source time
N200	192	$36 \times 0.1$	fixed	(TF,SE,LI8)	5 / 2	32,52
			relative	(TI8,SE,LI8)	2 / 1	-

TABLE 5.1: Number of eigenvectors, stout-smearing parameters, dilution schemes, number of noise sources, and source times employed in this work

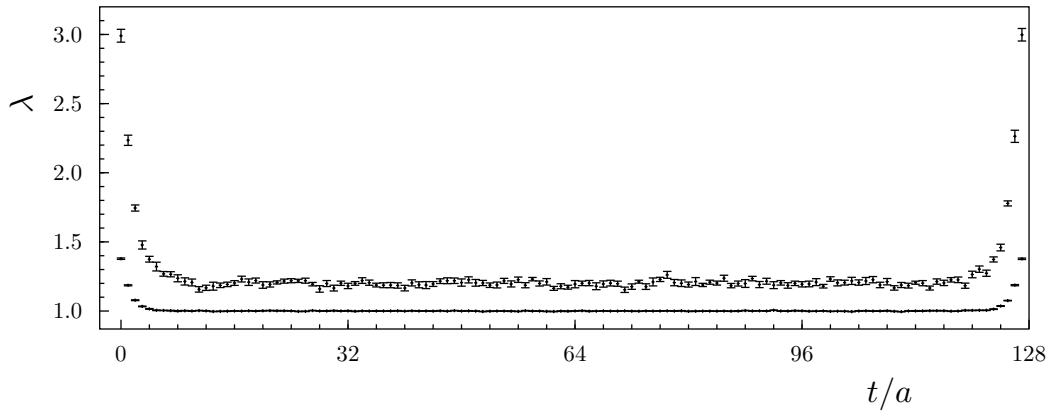


FIGURE 5.1: Smallest and largest retained eigenvalue of the three-dimensional covariant Laplacian on individual time slices of the lattice, normalized with respect to their plateau value. The normalized smallest eigenvalue is displaced vertically by 0.2 for visibility. Plot from [91].

The inversions were performed using the DFL\_SAP\_GCR solver [92–94] implemented in openQCD<sup>1</sup> embedded in the Chroma-based [95] stochastic LapH codebase. The code used for the calculation of the diagrams of the mixing matrix was implemented using the stochastic LapH codebase.

## 5.2 Static potential from Wilson loops

As the first important step towards string breaking on the N200 [96], we calculate an estimate of the string breaking distance using the energy of the static-light quark and the static potential from Wilson loops. We employ rectangular on-axis Wilson-loops  $W(t, r)$  to serve as an observable for the static potential. Here we map out the static potential using on-axis distances only.

Following the method presented in [97], as a first step, all gauge-links, including temporal links, are smeared using HYP2 parameters [49, 80]

$$\alpha_1 = 1.0 \quad \alpha_2 = 1.0 \quad \alpha_3 = 0.5. \quad (5.1)$$

This amounts to a change in the static action, as detailed in section 3.2.2. Afterwards, we construct a variational basis using 15 and 20 levels of HYP smeared spatial links with parameters

$$\alpha_2 = 0.6 \quad \alpha_3 = 0.3. \quad (5.2)$$

<sup>1</sup><http://luscher.web.cern.ch/luscher/openQCD/>

Using two different levels of smearing renders a  $2 \times 2$  correlation matrix. After solving the GEVP, the ground state, which corresponds to the static potential  $V(r)$ , can be extracted. The potential  $V(r)$  is renormalized by subtracting twice the energy of a static-light meson in order to obtain an estimate of the string breaking distance.

The analysis of the correlation functions of the static-light and static-strange meson is not only interesting with respect to the renormalization of the potential. The stochastic LapH method has not been used before for correlation functions involving static quarks. It is important to show that the method allows for accurate determinations of temporal correlations involving static quarks, as can be seen in Figure 5.2, showing the  $t_{\min}$ -plots for the static-light and static-strange mesons. The individual points are obtained through a correlated fit of the reweighted correlation function to a single exponential within the interval  $[t_{\min}, t_{\max} = 30a]$  using Bootstrap error estimation.  $N_b = 800$  samples are employed and the uncertainty quoted is given by  $1\sigma$  Bootstrap errors. The covariance matrix was estimated on the original data and is kept 'frozen' on all samples. The fitted mass is calculated as a function of  $t_{\min}$ . Our results for the static-light and static-strange energies show a good precision with a relative uncertainty of 0.5% and 0.2%, respectively. We find

$$m_B = 0.330(2)a \quad (5.3)$$

$$m_{B_s} = 0.3434(9)a.$$

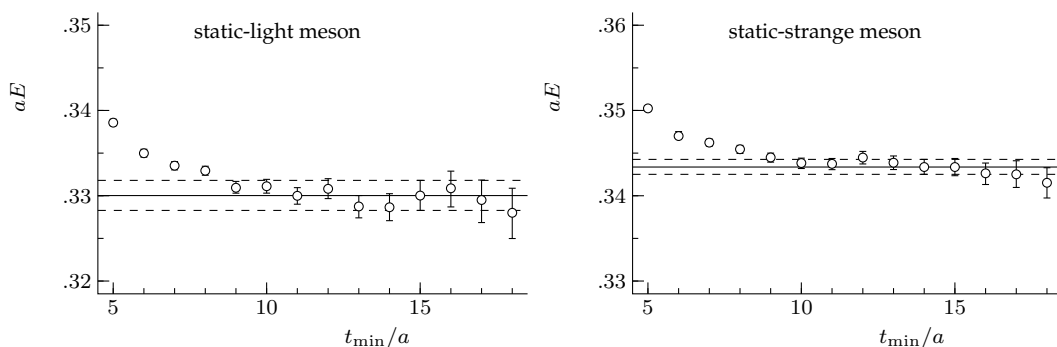


FIGURE 5.2:  $t_{\min}$ -plot for the static-light and static-strange meson on 104 configurations of N200. The solid horizontal line indicates the plateau average and the gray dashed lines its statistical uncertainty.

As a first step towards the full analysis, we analyzed the potential using 100 configurations of N200 [96]. Assuming string breaking to occur around  $[V(r) - 2E_{stat}] > 0$ , we found  $r_b \approx 19a$  as the value for the expected string breaking distance.

If we have a look at the potential using all 1664 Wilson loops calculated for the full mixing

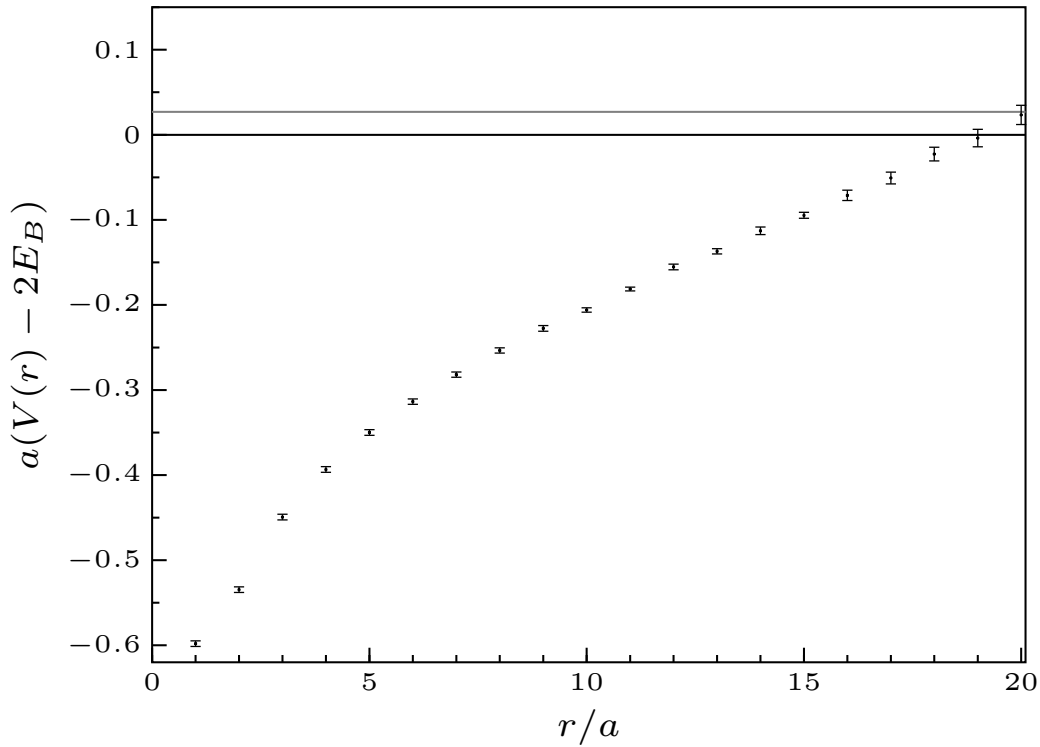


FIGURE 5.3: Static potential from Wilson loops on 1664 configurations of N200. The grey line corresponds to twice the static-strange meson mass, the error is too small to be visible. The error of the static-light meson mass is automatically taken into account by using the ratio given in equation (3.58)

analysis, this value is confirmed. This step of the analysis is not only important in order to check if the ensemble is suitable for string breaking, but enables us to choose an appropriate window for enhancing the spatial resolution. We utilize a set of off-axis distances between  $17a$  and  $21.8a$  to make sure that we are able to map out the first as well as the second expected avoided level crossing.

As detailed in Chapter 4.1, the Wilson loop does not have good overlap with the ground state after string breaking. This is the reason why in figure 5.3, the static potential is only shown for distances before string breaking and in the expected breaking region. We do not see a flattening of the potential. A look at a  $t_{\min}$ -plot for a distance beyond which the string is supposedly broken, shows no sign of relaxation towards the ground state before the signal to noise ratio becomes small. This demonstrates the need for the mixing analysis using the full correlation matrix including the two static-light meson state in order to reliably obtain the static potential for all distances.

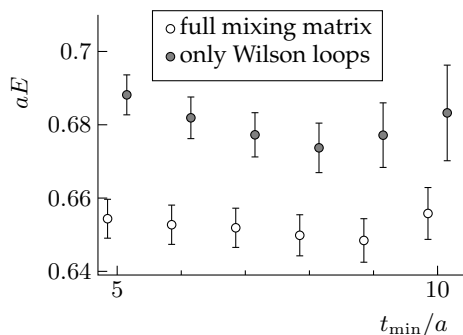


FIGURE 5.4: The  $t_{\min}$ -plot for the Wilson loop at separation  $20a$  shows no relaxation to the ground state.

### 5.3 Mixing analysis

The correlation matrix employed for the analysis is a  $4 \times 4$  matrix. It is an extension of the matrix given in equation (5.1), including 15 and 20 levels of spatial HYP smearing. The diagrams involving light and strange quark propagators are measured on a set of 104 evenly spaced configurations of the N200. It was found in [76] that the limiting factor of the statistical resolution is the precision of the Wilson loop data. A preliminary analysis of smaller sets of our data corroborated this finding. Because of this, the Wilson loops are determined on a much larger set of configurations. The diagrams containing only static quarks were measured on 1664 configurations. In order to consistently take account of correlations between different matrix elements, the Wilson loop correlators are rebinned into 104 bins, containing 16 configurations each, such that the center of the bin is aligned with one of the 104 configurations.

For each distance  $r = |\mathbf{y} - \mathbf{x}|$ , we average over distinct permutations of components  $(r_1, r_2, r_3)$  in order to increase statistics by exploiting the cubic symmetry of the lattice. For instance for distance  $r = 1$ , we take the average of vectors  $\mathbf{r} = (001), (010), (100)$ . We do not observe any dependence on the direction in the data. Depending on the number of permutations for a vector, this leads to a difference in statistics for classes of distances.

For the off-axis distances in Wilson loops, it was shown in [98] that it has a large impact how the path of links connecting the off-axis heavy quark pair is chosen. It was argued that in order to isolate the ground state potential for off-axis paths, it is important to choose a path-symmetrized operator over a non-symmetrized one. If two points  $\mathbf{x}$  and  $\mathbf{y}$  are separated by  $n_x, n_y, n_z$  sites in the three spatial directions, respectively, the non-symmetrized operators in that study are defined by first going in direction  $x$ , then in direction  $y$  and last in direction  $z$ , or permutations of  $xyz$  that are not averaged. These operators are susceptible to excited

state contamination. In order to ameliorate ground state overlap, path-symmetrized operators could be chosen. However, we follow a different approach to achieve a good ground state overlap by using paths that stick to the direct connection, the straight line between quark and antiquark, as closely as possible. This can be achieved by a procedure known as the Bresenham algorithm [99] in computer graphics, which is described for Wilson loops in [100]. By sticking to the closest path, the overlap between creation operator and the physical string state is vastly enhanced. In [100], the closest path was symmetrized as well, but since we use HYP smearing for the spatial links connecting the static quarks, we get good ground state overlap without utilizing explicit symmetrization.

For every distance  $r = |\mathbf{y} - \mathbf{x}|$ , a separate variational analysis has to be performed in order to extract the ground state as well as the first and second excited state. We perform a fixed GEVP, as described in section 3.4.2, for every distance  $r$ . The analysis is based on a Jupyter notebook<sup>2</sup> adapted from [70]. The notebook provides an interface to view systematics related to choices of fitting procedure, fitting ranges and GEVP parameters. It enables extensive comparison of  $t_{\min}$ -plots for different  $(t_0/a, t_d/a)$  combinations as well as GEVP operator sets for a systematic consistency check.

We use ratio fits (3.58) in order to extract the energy levels. The fit ranges are chosen in a way that the systematic errors due to the GEVP parameters and fit ranges are smaller than the statistical ones. We find that the systematic effects due to varying the fitting range  $[t_{\min}/a, t_{\max}/a]$ , especially  $t_{\min}/a$ , are the largest.  $t_{\min}$ -plots are used to control the  $t_{\min}/a$  dependence. The plots display the fitted mass plotted as a function of  $t_{\min}/a$ . We require the plateaus to be stable for different  $t_{\max}/a$  and the chosen  $[t_{\min}/a, t_{\max}/a]$  needs to have a suitable correlated  $\chi^2/Dof \lesssim 2$ .

As mentioned above, we are introducing a potential source of systematic uncertainties by using a fixed GEVP. To investigate the effect, we compare the chosen combination of parameters for the fixed GEVP with the full GEVP as given in equation (3.49). For comparison, we choose one distance smaller and larger than the string breaking distance, as well as one distance inside the mixing region. The plots show very good agreement between the two methods.

---

<sup>2</sup><https://github.com/ebatz/jupan>

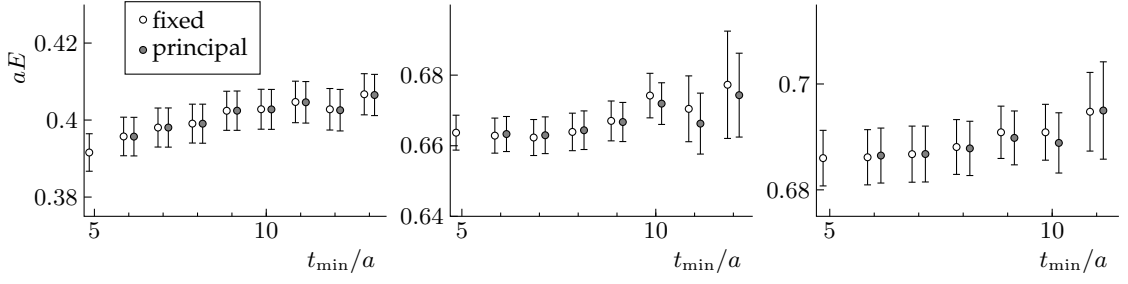


FIGURE 5.5: Comparison of fixed GEVP with  $t_0/a = 5, t_d/a = 10$  to principal GEVP for distance  $r/a = 8$

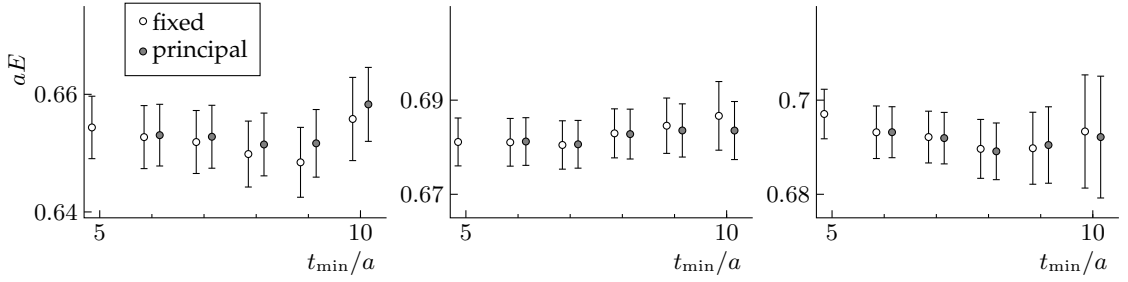


FIGURE 5.6: Comparison of fixed GEVP  $t_0/a = 5, t_d/a = 10$  to principal GEVP for distance  $r/a = 20$

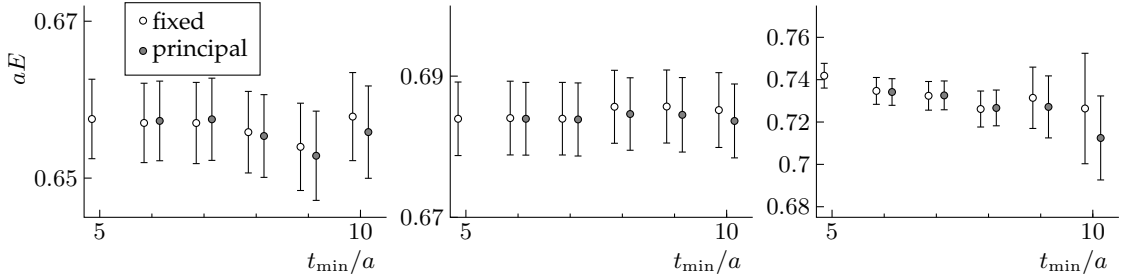


FIGURE 5.7: Comparison of fixed GEVP  $t_0/a = 5, t_d/a = 10$  to principal GEVP for distance  $r/a = 22$

Now we turn to the full mixing analysis for all on-axis and off-axis distances. For all distances, we use the fixed GEVP with  $t_0/a = 5, t_d/a = 10$ . We determine if this GEVP is stable against varying  $t_0/a, t_d/a$  and changing the operator sets in order to determine a good fit range  $[t_{\min}/a, t_{\max}/a]$ . The fit range is different for every distance. Table 5.2 gives an overview of employed distances, the chosen values for  $[t_{\min}/a, t_{\max}/a]$ ,  $\chi^2/Dof$  and the results for all three energy levels. The corresponding  $t_{\min}$ -plots for all distances can be found in Appendix A2. In figure 5.8, the result for the static potential normalized with respect to twice the static-light meson mass is shown. The first and second excited state for the two smallest distances do not exhibit a plateau, so there are no extracted energies for these states. Figure 5.8 shows the avoided level crossing between the ground state and the first

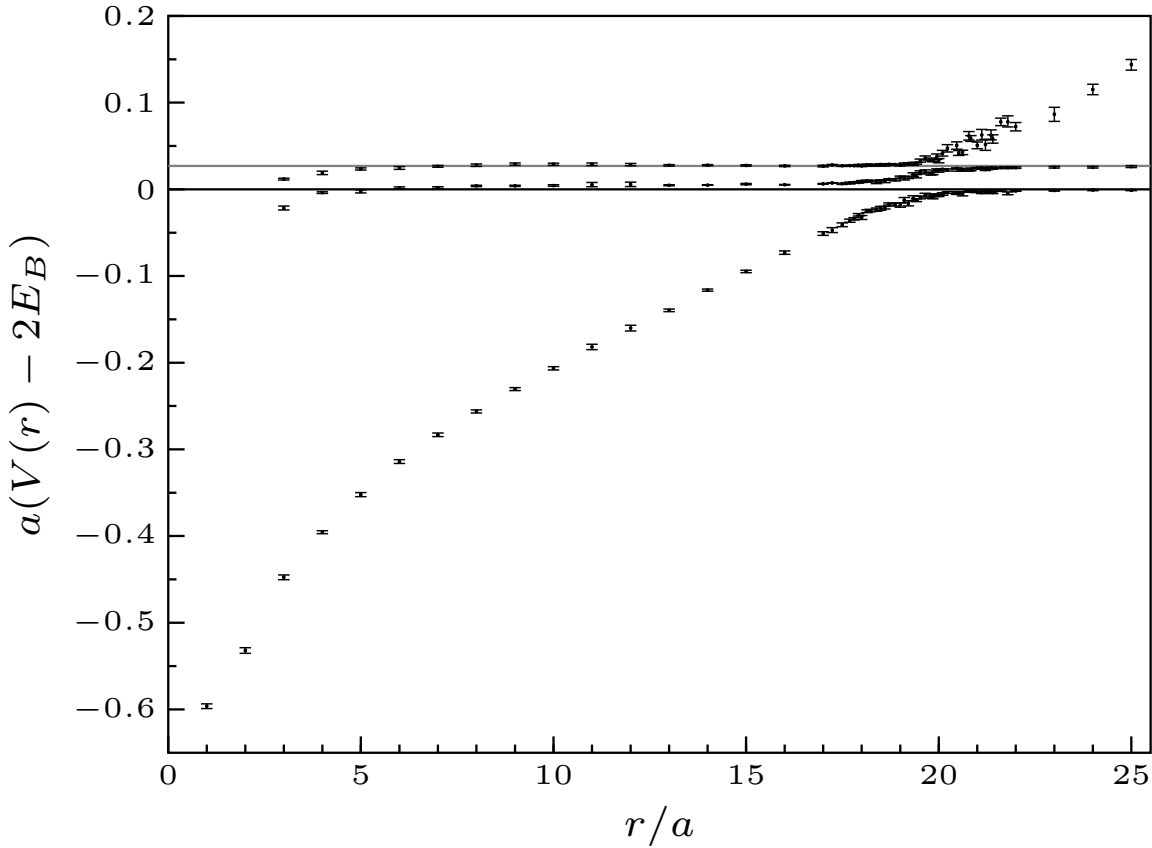


FIGURE 5.8: Static potential determined using the full mixing matrix. The grey line corresponds to twice the static-strange mass, its error is too small to be visible. The error of the static-light meson mass is automatically taken into account by using the ratio given in equation (3.58).

excited state clearly. The expected second avoided crossing due to the formation of two static-strange mesons is evident for the first time from lattice calculations. The off-axis distances allow for a good resolution. For distances beyond string breaking, the ground state tends towards the mass of two noninteracting static-light mesons. This behaviour cannot be observed if the potential is calculated from Wilson loops only.

Apart from the string breaking region, the plot exhibits interesting features for small and intermediate distances. The first level lies slightly above  $2E_B$  for intermediate distances smaller than the string breaking distance. For the second extracted energy level, we observe agreement with  $2E_{B_s} - 2E_B$  at intermediate distances and beyond string breaking, as expected. For small distances, there is a deviation from the non interacting energy of two static-strange mesons. This deviation from the non interacting energy  $2E_B$  of two static-light mesons at small distances can be observed for the first level as well. These deviations could be indications of interactions between the two static-light or two static-strange mesons, respectively. However, the behaviour at small distances could also occur due to the fact that



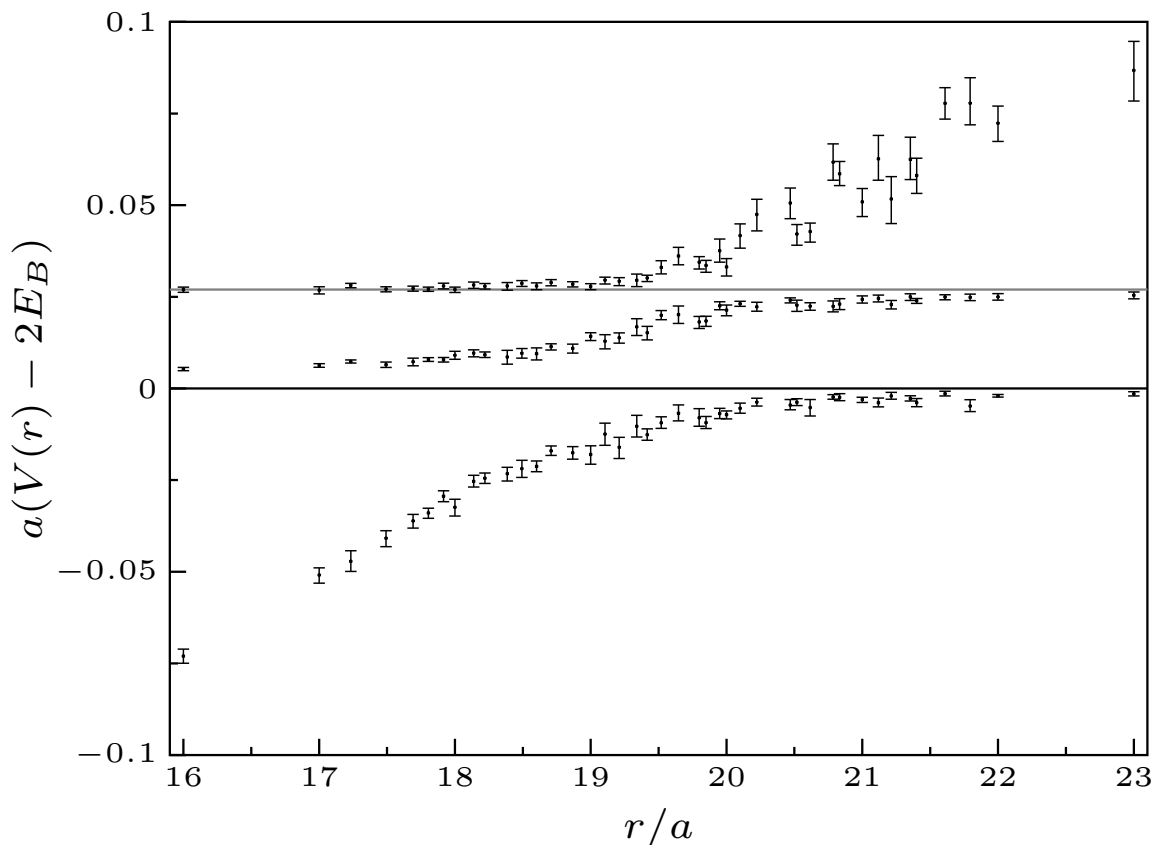


FIGURE 5.9: Static potential, same as figure 5.8, but zoomed into the string breaking region. The grey line indicates twice the static-strange meson mass. The error of the static-light meson mass is automatically taken into account by using the ratio given in equation (3.58)

our operator basis is not large enough. If there is another state with the same quantum numbers lying below the energies, no reliable extraction of the states is possible. For instance, a string plus two pion state  $Q\bar{Q}\pi\pi$  has the same quantum numbers. The energy of this state is given by the energy of the ground state plus twice the pion mass and for our ensemble the corresponding energy lies below the two static-light energy up to  $r/a \approx 11$ .

Figure 5.9 shows the string breaking region in more detail. It is apparent that the region extends over several lattice spacings. Both avoided crossings are visible, the energy gap between the ground state and first level is larger than the gap between the first and the second level. Qualitatively, the region of the first mixing appears to be broader, but it is not possible to determine the difference between the first string breaking distance  $r_c$  and the second string breaking distance  $r_{c_s}$  by eye.

$r/a$	$\mathbf{r}/a$	$(r/a)^2$	$t_{\max}/a$	$t_{\min}/a$	$\chi^2$	$aE_0, aE_1, aE_2$	$r/a$	$\mathbf{r}/a$	$(r/a)^2$	$t_{\max}/a$	$t_{\min}/a$	$\chi^2$	$aE_0, aE_1, aE_2$
1.0	(0 0 1)	1	25	13	1.798	0.0638(26)	17.0	(0 0 17)	289	20	7	0.81	0.609(4)
						-					6	1.002	0.6663(35)
						-					7	0.47	0.687(4)
2.0	(0 0 2)	4	27	14	1.787	0.1281(17)	17.234	(8 8 13)	297	23	8	0.81	0.613(4)
						-					5	0.796	0.6674(35)
						-					6	1.237	0.688(4)
3.0	(0 0 3)	9	25	13	1.791	0.2126(26)	17.493	(0 9 15)	306	20	8	1.526	0.619(4)
				9	0.765	0.638(4)					7	1.246	0.6665(35)
				6	1.819	0.672(4)					6	1.068	0.687(4)
4.0	(0 0 4)	16	23	10	2.383	0.2644(30)	17.692	(0 12 13)	313	20	7	0.57	0.624(4)
				7	1.127	0.656(4)					7	0.897	0.6673(35)
				8	1.051	0.679(4)					6	1.196	0.687(4)
5.0	(0 0 5)	25	27	12	2.271	0.3080(27)	17.804	(0 11 14)	317	22	6	0.956	0.626(4)
				8	0.681	0.658(4)					6	1.065	0.6679(35)
				7	1.236	0.684(4)					5	1.108	0.687(4)
6.0	(0 0 6)	36	25	11	2.373	0.3460(30)	17.916	(5 10 14)	321	20	6	1.081	0.631(4)
				7	1.237	0.662(4)					6	0.702	0.6679(35)
				8	1.411	0.685(4)					6	0.984	0.688(4)
7.0	(0 0 7)	49	21	11	2.019	0.3769(31)	18.0	(0 0 18)	324	18	7	0.693	0.628(4)
				7	2.478	0.662(4)					7	0.773	0.669(4)
				6	0.629	0.687(4)					6	0.663	0.687(4)
8.0	(0 0 8)	64	20	10	1.964	0.4038(32)	18.138	(8 11 12)	329	19	6	0.546	0.635(4)
				6	1.361	0.6639(35)					6	0.862	0.670(4)
				7	0.986	0.688(4)					6	0.997	0.688(4)
9.0	(0 0 9)	81	21	10	1.814	0.4296(33)	18.221	(6 10 14)	332	18	6	1.278	0.636(4)
				6	1.864	0.6641(35)					6	0.632	0.6693(35)
				7	1.055	0.689(4)					6	0.881	0.688(4)
10.0	(0 0 10)	100	25	10	1.247	0.4535(35)	18.385	(0 13 13)	338	20	7	0.765	0.637(4)
				7	1.91	0.6643(35)					8	1.597	0.669(4)
				7	1.163	0.689(4)					7	1.486	0.688(4)
11.0	(0 0 11)	121	20	12	1.095	0.478(4)	18.493	(5 11 14)	342	20	8	0.332	0.638(4)
				9	2.129	0.665(4)					7	0.903	0.670(4)
				8	1.774	0.689(4)					6	0.537	0.689(4)
12.0	(0 0 12)	144	25	12	0.68	0.500(5)	18.601	(0 11 15)	346	18	7	1.89	0.639(4)
				9	1.397	0.666(4)					8	1.089	0.670(4)
				8	1.367	0.689(4)					7	1.882	0.688(4)
13.0	(0 0 13)	169	20	8	1.663	0.520(4)	18.708	(5 10 15)	350	20	6	1.467	0.643(4)
				6	1.871	0.6647(35)					6	0.543	0.6714(35)
				6	1.297	0.688(4)					6	1.687	0.689(4)
14.0	(0 0 14)	196	22	6	1.7	0.544(4)	18.868	(0 10 16)	356	20	8	0.856	0.642(4)
				5	1.395	0.6650(35)					7	1.04	0.671(4)
				6	0.628	0.688(4)					6	1.529	0.688(4)
15.0	(0 0 15)	225	18	6	0.634	0.565(4)	19.0	(0 0 19)	361	20	8	0.799	0.642(5)
				7	1.209	0.666(4)					6	0.438	0.674(4)
				6	0.599	0.688(4)					6	0.607	0.688(4)
16.0	(0 0 16)	256	20	7	0.594	0.587(4)	19.105	(0 13 14)	365	20	9	1.107	0.648(5)
				6	0.653	0.665(4)					8	1.415	0.673(4)
				6	0.756	0.687(4)					6	1.016	0.690(4)

$r/a$	$\mathbf{r}/a$	$(r/a)^2$	$t_{\max}/a$	$t_{\min}/a$	$\chi^2$	$aE_0, aE_1, aE_2$	$r/a$	$\mathbf{r}/a$	$(r/a)^2$	$t_{\max}/a$	$t_{\min}/a$	$\chi^2$	$aE_0, aE_1, aE_2$
19.209	(0 12 15)	369	20	9	0.916	0.644(5)	21.0	(0 0 21)	441	20	7	1.225	0.657(4)
				7	1.085	0.674(4)					7	0.893	0.684(4)
				7	1.2	0.689(4)					7	1.587	0.711(5)
19.339	(7 10 15)	374	20	9	1.338	0.650(4)	21.119	(9 13 14)	446	20	8	0.963	0.6561(35)
				8	0.422	0.677(4)					7	1.717	0.685(4)
				7	1.46	0.690(4)					8	0.486	0.723(7)
19.416	(0 11 16)	377	20	8	0.756	0.647(4)	21.213	(0 15 15)	450	17	7	1.288	0.6580(35)
				8	0.738	0.675(4)					7	1.503	0.683(4)
				6	1.61	0.690(4)					8	0.99	0.712(7)
19.519	(8 11 14)	381	18	8	0.902	0.651(4)	21.354	(8 14 14)	456	17	7	2.066	0.6573(35)
				7	0.446	0.680(4)					7	1.501	0.685(4)
				6	1.387	0.693(4)					8	0.67	0.723(7)
19.647	(11 11 12)	386	20	8	1.049	0.653(4)	21.401	(0 13 17)	458	18	8	0.354	0.656(4)
				8	0.644	0.680(4)					6	1.1	0.684(4)
				6	0.68	0.696(4)					8	0.853	0.718(6)
19.799	(0 14 14)	392	18	8	1.344	0.652(4)	21.61	(11 11 15)	467	17	7	0.711	0.6586(35)
				7	1.188	0.678(4)					6	1.298	0.685(4)
				7	0.494	0.694(4)					7	0.422	0.738(5)
19.849	(0 13 15)	394	18	8	1.162	0.651(4)	21.794	(9 13 15)	475	18	9	1.458	0.655(4)
				7	1.348	0.678(4)					7	2.741	0.685(4)
				7	0.701	0.694(4)					8	0.764	0.738(7)
19.95	(9 11 14)	398	20	8	1.256	0.6532(35)	22.0	(0 0 22)	484	20	6	1.926	0.6580(35)
				7	0.468	0.683(4)					7	0.816	0.685(4)
				7	0.977	0.698(4)					7	1.261	0.732(6)
20.0	(0 0 20)	400	20	7	1.83	0.653(4)	23.0	(0 0 23)	529	18	7	1.721	0.659(4)
				7	0.977	0.681(4)					7	1.038	0.685(4)
				7	0.753	0.693(4)					8	1.791	0.747(9)
20.1	(8 12 14)	404	20	8	0.941	0.6546(35)	24.0	(0 0 24)	576	18	7	1.989	0.659(4)
				6	0.61	0.683(4)					7	0.453	0.685(4)
				7	1.804	0.702(4)					7	1.596	0.775(7)
20.224	(11 12 12)	409	20	7	0.828	0.6563(35)	25.0	(0 0 25)	625	20	6	1.643	0.659(4)
				7	0.66	0.682(4)					8	0.401	0.6863(35)
				7	0.615	0.707(5)					7	1.074	0.804(7)
20.469	(9 13 13)	419	20	8	0.546	0.6555(34)	TABLE 5.2: Table of all distances, fitting parameters and three extracted energy levels						
				6	1.492	0.684(4)							
				7	0.983	0.711(5)							
20.518	(0 14 15)	421	18	7	1.305	0.6563(35)							
				8	0.73	0.683(4)							
				7	0.707	0.702(4)							
20.616	(0 13 16)	425	17	9	0.951	0.655(4)							
				7	0.759	0.682(4)							
				7	0.801	0.703(4)							
20.785	(12 12 12)	432	20	6	0.722	0.658(4)							
				8	0.738	0.682(4)							
				7	1.377	0.722(6)							
20.833	(11 12 13)	434	17	7	1.016	0.6576(35)							
				8	0.713	0.683(4)							
				6	0.646	0.719(4)							

The quantification of string breaking involving three levels is more complex in comparison to the two-level situation. For  $N_f = 2$  string breaking, the string breaking distance  $r_c$  can be defined as the distance where the energy gap  $\Delta E$  between the two states becomes minimal, see [76]. For the  $N_f = 2 + 1$  mixing scenario, a more complex model is necessary to define the two string breaking distances  $r_c$  and  $r_{c_s}$ .

In the next section we try to quantify the  $N_f = 2 + 1$  mixing phenomenon by employing a simple Hamiltonian model.

## 5.4 Model for the string breaking spectrum

We describe the string breaking data by a simple model that is an extension of the model for the  $n_f = 2$  given in [15]. Consider a three state system with a Hamiltonian given by:

$$H(r) = \begin{pmatrix} \hat{V}(r) & g_1 & g_2 \\ g_1 & E_1 & 0 \\ g_2 & 0 & E_2 \end{pmatrix}. \quad (5.4)$$

The diagonal elements are a function  $V(r)$  describing the unbroken string and  $E_1, E_2$ , the energies of a noninteracting pair of static-light and static-strange mesons, respectively.  $g_1$  and  $g_2$  are two coupling constants describing the strength of the mixing between the diagonal elements. The mixing between static-light and static-strange mesons is assumed to be negligible and is therefore set to zero. A suitable choice for the function representing the string state is the Cornell potential, given in equation (4.2). Since we are interested in modeling the string breaking region and not the potential at small distances, we use only the linear part of  $\hat{V}_l(r) = \sigma r + V_0$  to fit our data and include only data points for distances larger than  $r/a = 11$ .

The eigenstates of the Hamiltonian  $H$  are mixtures between the unbroken string and the two static-light and two static-strange meson state. The eigenvalues of  $H$  correspond to the three extracted energy levels. After diagonalizing  $H$ <sup>3</sup>, we fit the model to the data.

As mentioned in section 3.4, problems arise for correlated fits, when the number of configurations  $N_{\text{Cfg}}$  is equal to or not much larger than the number of data points  $N_d$  one wants to fit [59, 60], resulting in the appearance of very small eigenvalues in the covariance matrix that dominate the inverse used in constructing the correlated  $\chi^2$ . The small eigenvalues can

<sup>3</sup>The eigenvalues and eigenvectors of a hermitian  $3 \times 3$  Matrix are known analytically [101]

increase the correlation in the sample and also bias the fit parameters. In our case, the situation is even worse, because we measured on 104 configurations, but would like to fit around 140 data points, depending on how many distances we include. In this case there are  $N_d - N$  zero eigenvalues.

One possible way to ameliorate the situation is the use of singular value decomposition, as described in section 3.4. We introduce an SVD cut  $c$  in a way that no eigenvalue smaller than  $c$  times the largest eigenvalue is retained, in order to get a reasonable correlated  $\chi^2$  and obtain a stable fit. We choose  $c = 10^{-3}$ . With this choice, we get  $\chi^2/Dof = 1.8$ , where it is important to note that now the number of degrees of freedom is reduced by one for each singular value removed.

We find for our fit parameters:

$$\begin{aligned}
 aE_1 &= 0.0262(4) \\
 aE_2 &= 0.0012(2) \\
 ag_1 &= 0.0079(3) \\
 ag_2 &= 0.0146(3) \\
 a^2\sigma &= 0.0232(2) \\
 aV_0 &= -0.437(3).
 \end{aligned}
 \tag{5.5}$$

Figure 5.10 shows the data as well as the result of the model fit. Figure 5.11 is the same plot, magnifying the string breaking region. The fits are performed on every bootstrap sample, the errors are  $1\sigma$  bootstrap errors. The errorband, displaying the bootstrap errors, is barely visible in both plots.

In our model, the mixing between light and strange mesons is set to zero and it assumes a three state system, even though it is possible that the physical eigenstates receive contributions from higher lying states and in the model. Nevertheless, the plots in figures 5.10 and 5.11 show that our data is described very well by the fit parameters.

While the eigenvalues  $\lambda_1, \lambda_2, \lambda_3$  of our Hamiltonian  $H$  model are the energy levels of the string breaking data, the eigenvectors  $v_1, v_2, v_3$  contain information about the overlaps. In order to investigate the overlap of the string-like, two static-light and static-strange meson-like interpolators onto the ground state, we plot the components of eigenvector  $v_1$ , shown in figure 5.12.

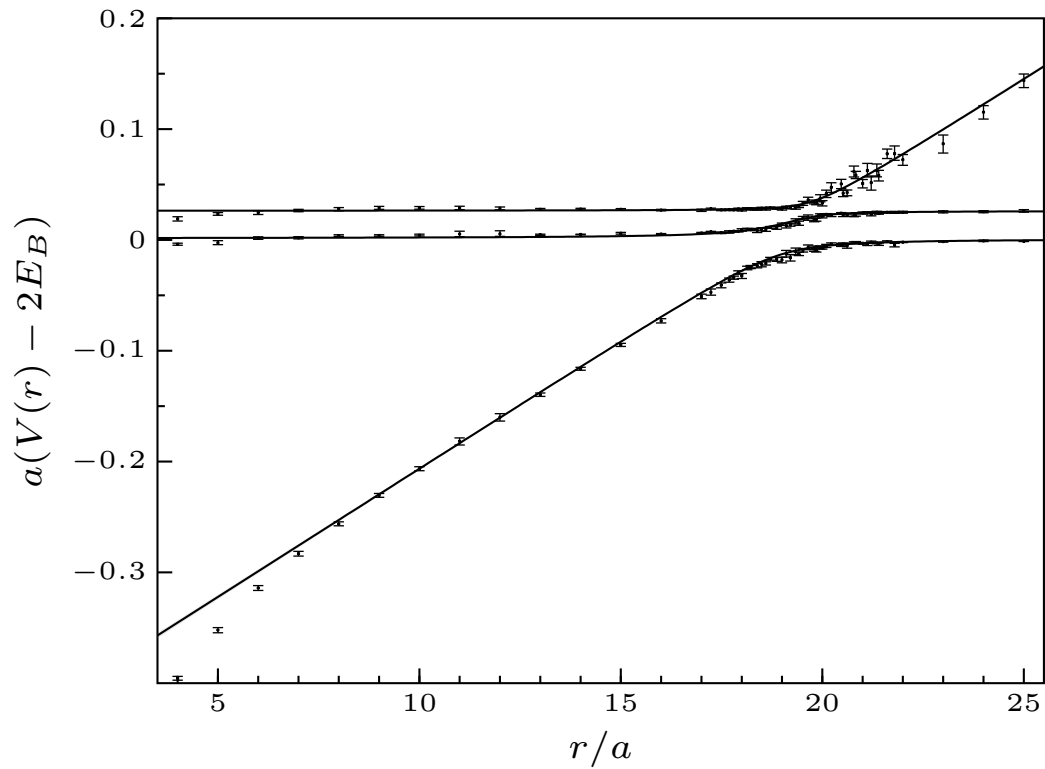


FIGURE 5.10: Six parameter fit to the string breaking data. The errorband is not visible.

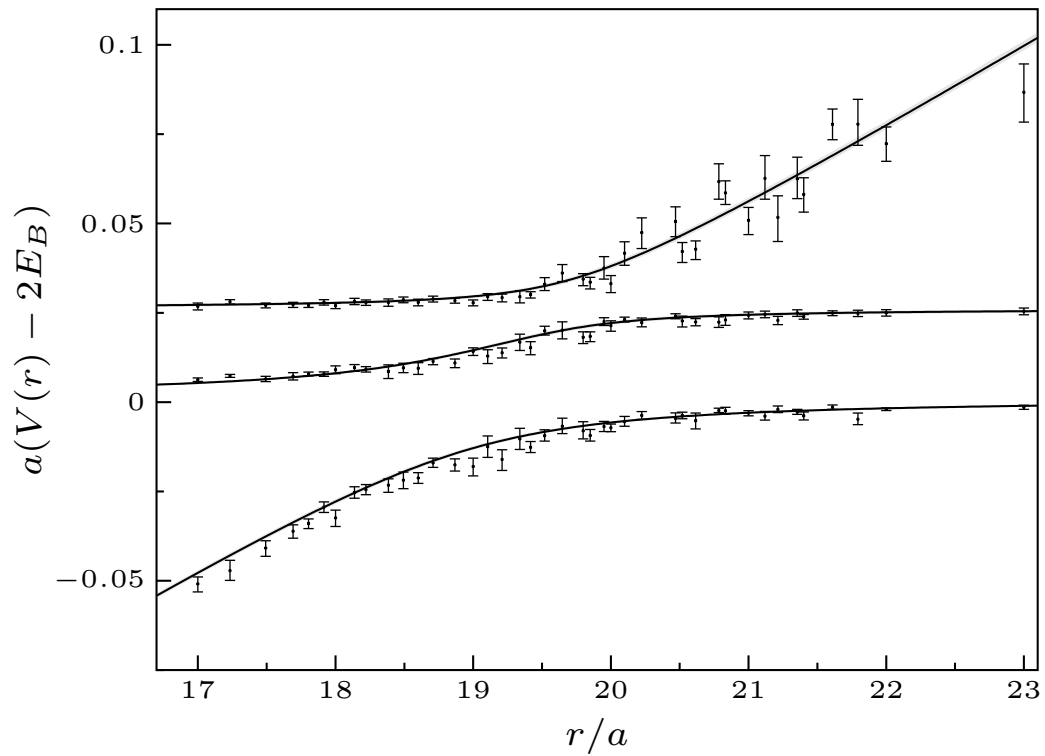


FIGURE 5.11: Same as figure 5.10, but zoomed into the string breaking region. The errorband is barely visible.

As expected, for distances smaller than the string breaking distance, the Wilson loop has large overlap with the ground state while for distances beyond string breaking, the two static-light meson state has large overlap onto the ground state. In the mixing region, both operators have a significant overlap with the ground state, the static-strange meson operator does not contribute considerably to the ground state and shows only a small overlap in the mixing region.

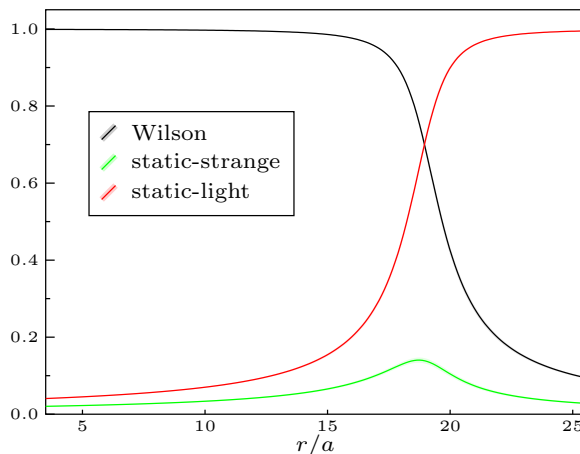


FIGURE 5.12: Overlap of interpolators onto ground state. The errorband indicating  $1\sigma$  bootstrap errors is not visible.

We can use the overlap to define the string breaking distance  $r_c$  as the point where the Wilson loop and the static-light meson operator have equal overlap onto the ground state, i.e. the mixing is most pronounced. Using this definition, we find for the string breaking distance

$$r_c = 18.952(40)a \approx 1.218(14)\text{fm}. \quad (5.6)$$

The quoted errors for the physical units take into account the uncertainty of  $a = 0.06426(74)\text{fm}$ . The scale setting for the CLS ensembles is thoroughly discussed in [89]. A corresponding definition can be employed to define the second string breaking distance  $r_{c_s}$  from the overlap of the interpolators onto the second excited state, shown in figure 5.13. The intersection between the Wilson and the two static-strange type operator is given by

$$r_{c_s} = 19.685(36)a \approx 1.265(15)\text{fm}. \quad (5.7)$$

We can now calculate the energy gap  $\Delta E_1$  between the ground and first excited state at the string breaking distance  $r_c$ , as well as the energy gap  $\Delta E_2$  between the first and second excited state for distance  $r_{c_s}$ . We find  $\Delta E_1 = 84(1)\text{MeV}$  and  $\Delta E_2 = 42(2)\text{MeV}$ , respectively. The energy  $\Delta E_1$  induced by the mixing of the string state and two static-light meson state is

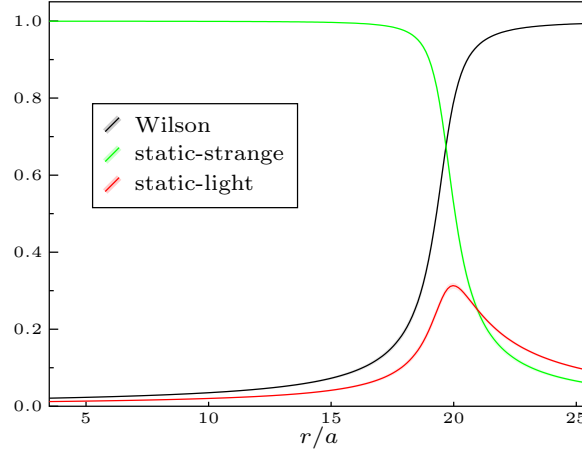


FIGURE 5.13: Overlap of interpolators onto second excited state. The error-band indicating  $1\sigma$  bootstrap errors is not visible.

larger than  $\Delta E_2$ , induced by the mixing of the string state and the heavier two static-strange meson state. Furthermore, we observe a narrowed mixing region for the second avoided level crossing in comparison with the first crossing, which can be seen in figure 5.8, but also by comparing the slope of the overlaps in figures 5.12 and 5.13. This behaviour is expected and was predicted in [76].

As mentioned before, only one previous study [76] of string breaking for  $N_f = 2$  QCD on the lattice exists with  $m_\pi \approx 640\text{MeV}$ . For the two state system, a different definition of the string breaking distance was used, so it is not straightforward to compare the result to our findings. In [76], agreement is found between two definitions of the string breaking distance. The first definition  $r_{c_1}$  gives the distance at which the energy gap between the two states assumes its smallest value and the second definition  $r_{c_2}$  denotes the distance of perfect mixing between the two states, in terms of a mixing angle of the two state system. They find

$$r_{c_1} \approx 1.248(13)\text{fm} \quad (5.8)$$

$$r_{c_2} \approx 1.244(16)\text{fm}, \quad (5.9)$$

where the quoted error is purely statistical and does not include the 5% uncertainty of the Sommer parameter  $r_0$  that was used to convert the result into physical units. The definition of  $r_{c_2}$  is similar to our definition applied to the three state system. A comparison of our results for the static-light and static-strange breaking distance with the results of Bali et al [76] shows that the string breaking distances are of the same order of magnitude. Their result  $r_{c_2} \approx 1.244(16)\text{fm}$ , even though in this study the pion mass  $m_\pi = 640\text{MeV}$  was relatively heavy, falls between our values  $r_c$  and  $r_{c_s}$ . However, due to differing definitions of the string breaking distance, it is not possible to make a statement on quark mass dependence. In the



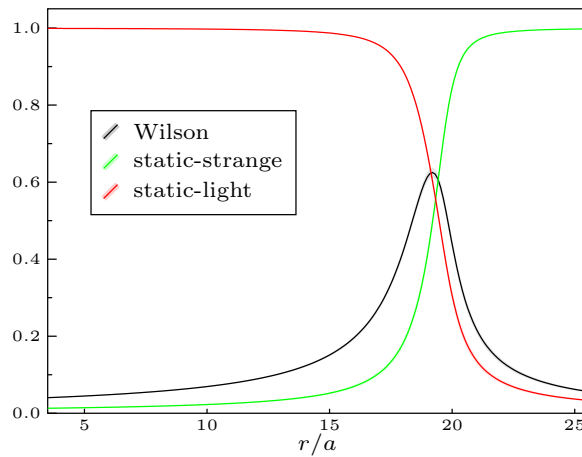


FIGURE 5.14: Overlap of interpolators onto first excited state. The errorband indicating  $1\sigma$  bootstrap errors.

case of the three state system, mixing occurs between three states, even though we define the string breaking distances by looking at the admixture of only two operators at the same time. To this account, it is interesting to look at the overlap of all operators onto the first state in Fig. 5.14, which shows sizable mixing of all operators in the string breaking region.

In order to investigate the dependence of the string breaking distance on the sea quark mass, calculations on  $N_f = 2 + 1$  ensembles with different quark masses need to be performed. We intend to do so in the future.



## Chapter 6

# Discussion and outlook

In this work, we have explored string breaking in QCD on the lattice using  $N_f = 2+1$  flavors of dynamical quarks. We identified a suitable method for string breaking on large lattices with small quark masses and to investigate the effect of the inclusion of third, heavier, sea quark flavor.

The stochastic LapH method yields practical all-to-all propagators and we find it facilitates accurate determinations of temporal correlation functions involving static quarks. We construct a  $4 \times 4$  correlation matrix in order to properly treat the mixing phenomenon and use a GEVP to extract the ground state and two excited states of the system containing a static quark and antiquark.

An exploratory study was carried out for the CLS N200 ensemble. We found that we are able to observe two avoided level crossings corresponding to the formation of two static-light and two static-strange mesons. Figure 5.11 displays the three extracted energy levels in the string breaking region and shows that we can resolve the small energy gap between the first and second excited state.

We provide a simple model for the mixing scenario that describes the string breaking data very well. Within the model we provide a definition of the string breaking distance  $r_c$  corresponding to the transition of the string into two static-light mesons and  $r_{c_s}$  the distance corresponding to the transition of the string into two static-strange mesons. Furthermore, the energy gaps between the respective states at  $r_c$  and  $r_{c_s}$  can be calculated. We find the following values

$$\begin{aligned} r_c &= 1.218(14)fm, & \Delta E_1 &= 84(1)\text{MeV} \\ r_{c_s} &= 1.265(15)fm, & \Delta E_2 &= 42(2)\text{MeV}. \end{aligned} \tag{6.1}$$

As a next step towards fully quantifying string breaking, the computation has to be repeated on a suitable set of ensembles, varying lattice size, lattice spacing and quark masses. Ideally, this will allow for an extrapolation to the continuum and a determination of finite volume errors as well as shed light on the quark mass dependence. Evidence suggests that the stochastic LapH method facilitates practical all-to-all propagation even in large physical volumes with spatial extent exceeding 5fm [102], which allows us to consider larger lattices for the string breaking analysis in the future. As previously mentioned, the landscape of ensembles generated by the CLS effort [24] covers a broad range of parameters and is therefore ideally suited for a continued investigation of string breaking on the lattice.

The next ensemble we will perform the calculations on is the D200, the computations are already underway.

id	$N_t \times N_s^3$	a[fm]	$m_\pi$ [MeV]	$m_K$ [MeV]	$m_\pi L$
N200	$128 \times 48^3$	0.064	280	460	4.4
D200	$128 \times 64^3$	0.064	200	480	4.2

TABLE 6.1

The N200 analyzed in this work and the D200 have the same lattice spacing, but different  $m_\pi$  and  $m_K$ , so the comparison of the two ensembles given in table 6.1 will allow us to explore the quark mass dependence.

# Appendix

## A1 Gamma matrices

We will use the conventions of [53], also used in the stochastic LapH codebase, which employs the Dirac-Pauli representation for the gamma matrices

$$\gamma_k = \begin{pmatrix} 0 & -i\sigma_k \\ -\sigma_k & 0 \end{pmatrix} \quad \gamma_4 = \begin{pmatrix} I & 0 \\ 0 & -I \end{pmatrix} \quad \gamma_5 = \begin{pmatrix} 0 & I \\ I & 0 \end{pmatrix}, \quad (6.2)$$

where the  $\sigma_i$  are the Pauli matrices. The Euclidean space gamma matrices are related to the Minkowski gamma matrices by

$$\gamma_1 = -i\gamma_1^M, \quad \gamma_2 = -i\gamma_2^M, \quad \gamma_3 = -i\gamma_3^M, \quad \gamma_4 = \gamma_0^M. \quad (6.3)$$

where  $\gamma_\mu^M$  are the Minkowski matrices. The Euclidean gamma matrices are hermitian and obey the anti-commutation relation

$$\{\gamma_\mu, \gamma_\nu\} = 2\delta_{\mu\nu}. \quad (6.4)$$

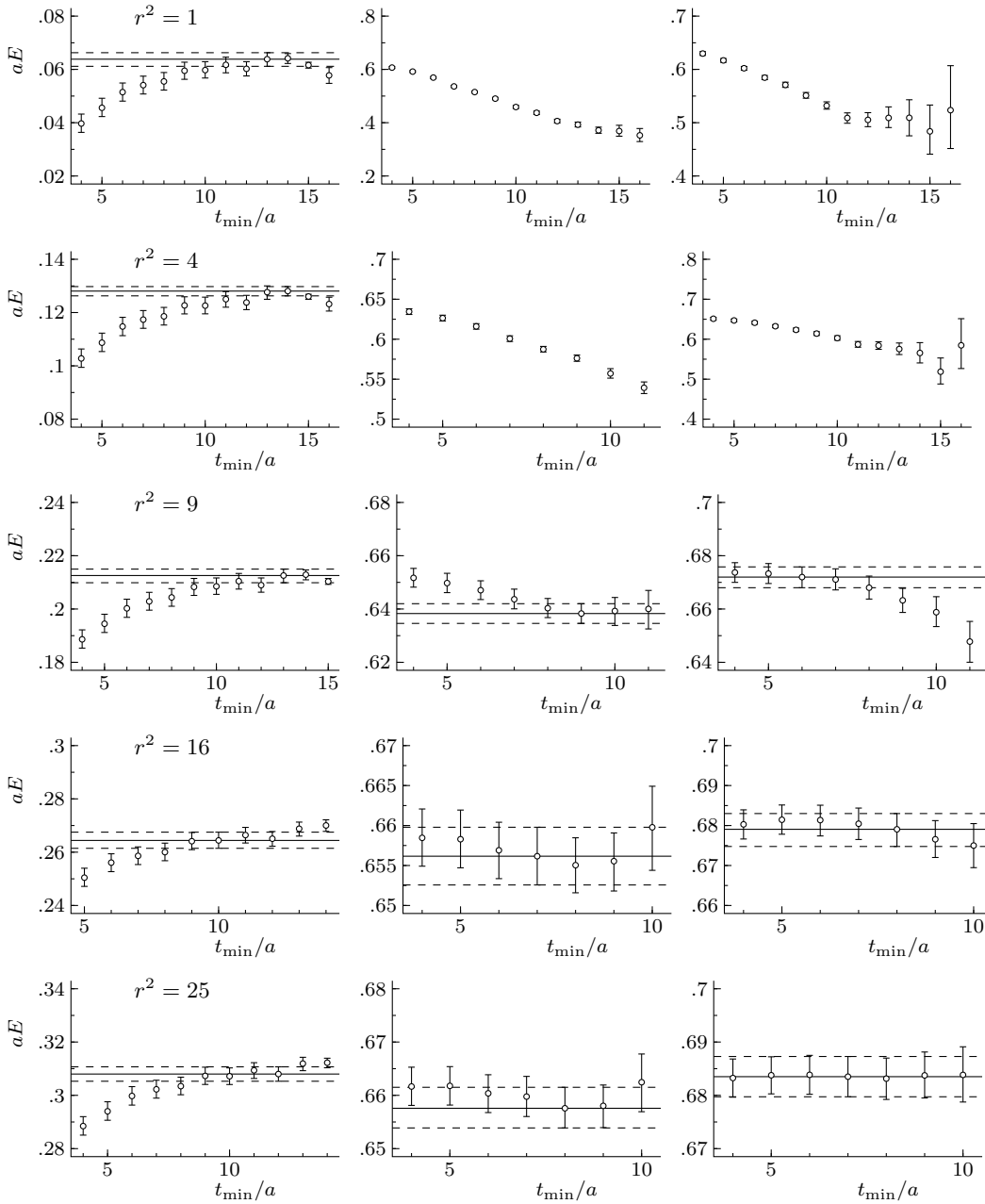
The fifth gamma matrix is given by

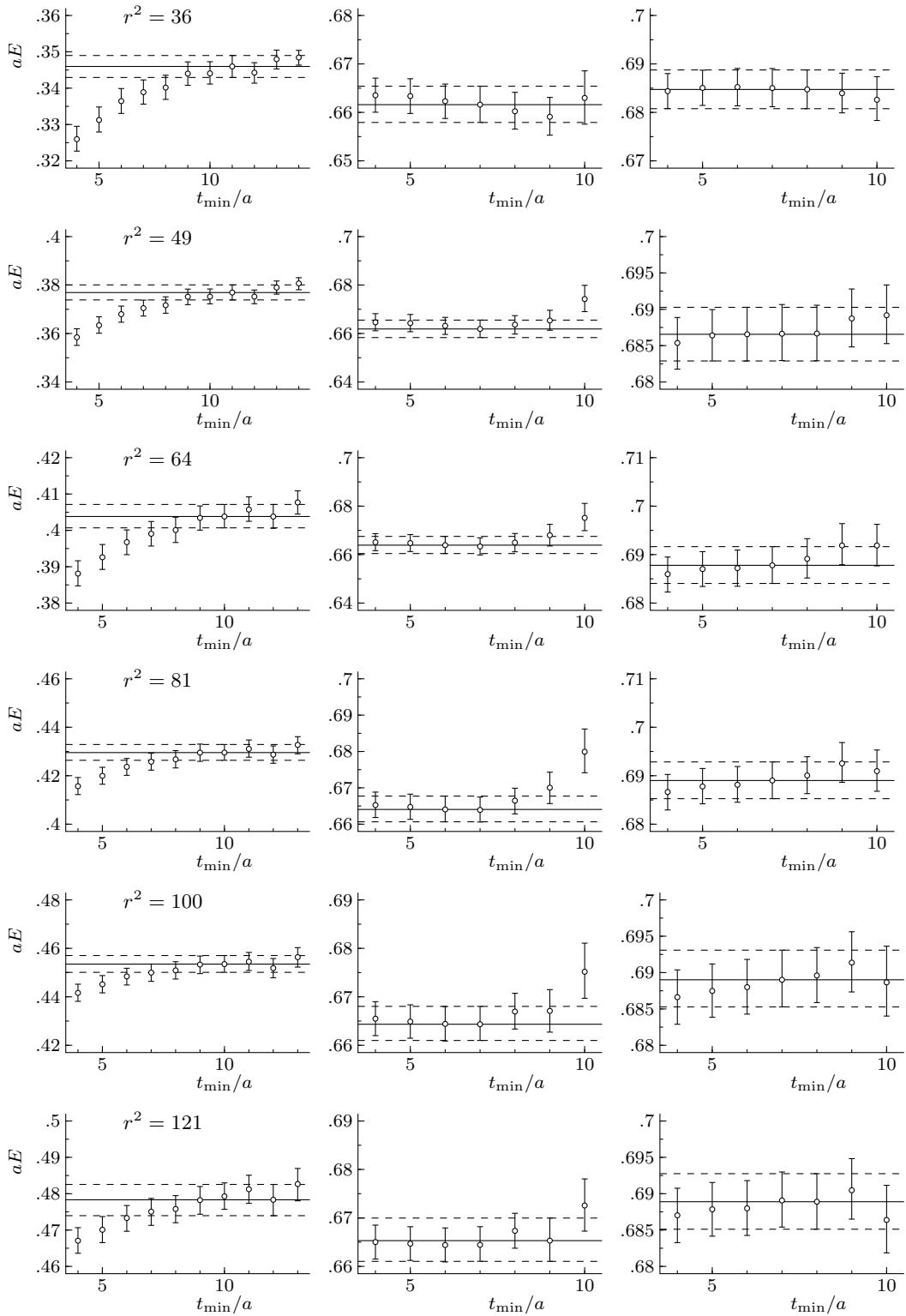
$$\gamma_5 = \gamma_4\gamma_1\gamma_2\gamma_3, \quad (6.5)$$

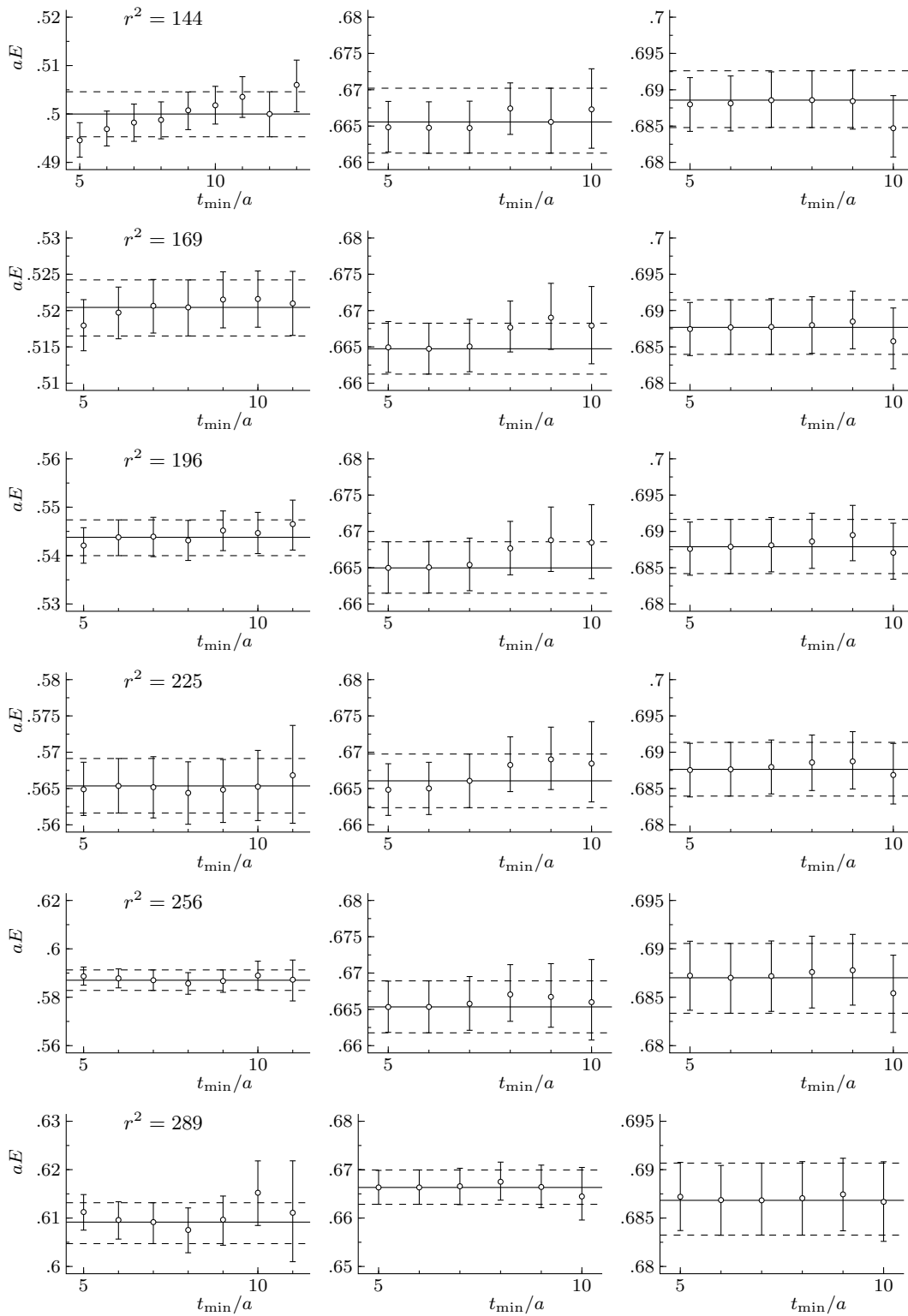
so  $\gamma_5$  anti-commutes with all the other gamma matrices and is hermitian.

## A2 $t_{\min}$ -plots for all energy levels

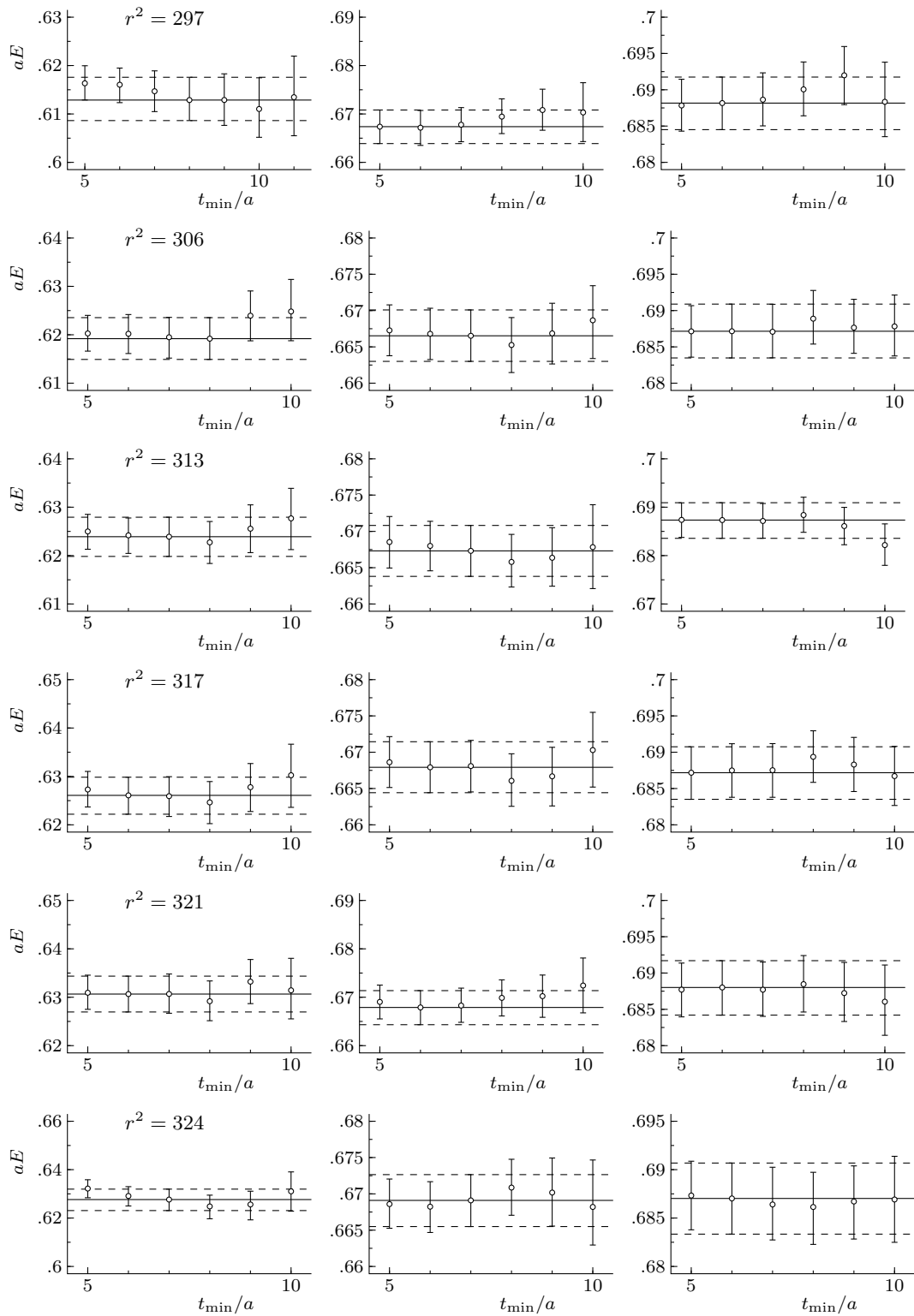
In this appendix all plots used in the extraction of the three energy levels in section 5.3 are shown. The corresponding extracted energies and fit parameters are listed in table 5.2. The solid horizontal line indicates the plateau average and the gray dashed lines display the  $1\sigma$  bootstrap error. The left plot corresponds to the ground state, the middle plot to the first excited state and the right plot shows the second excited state of the system.

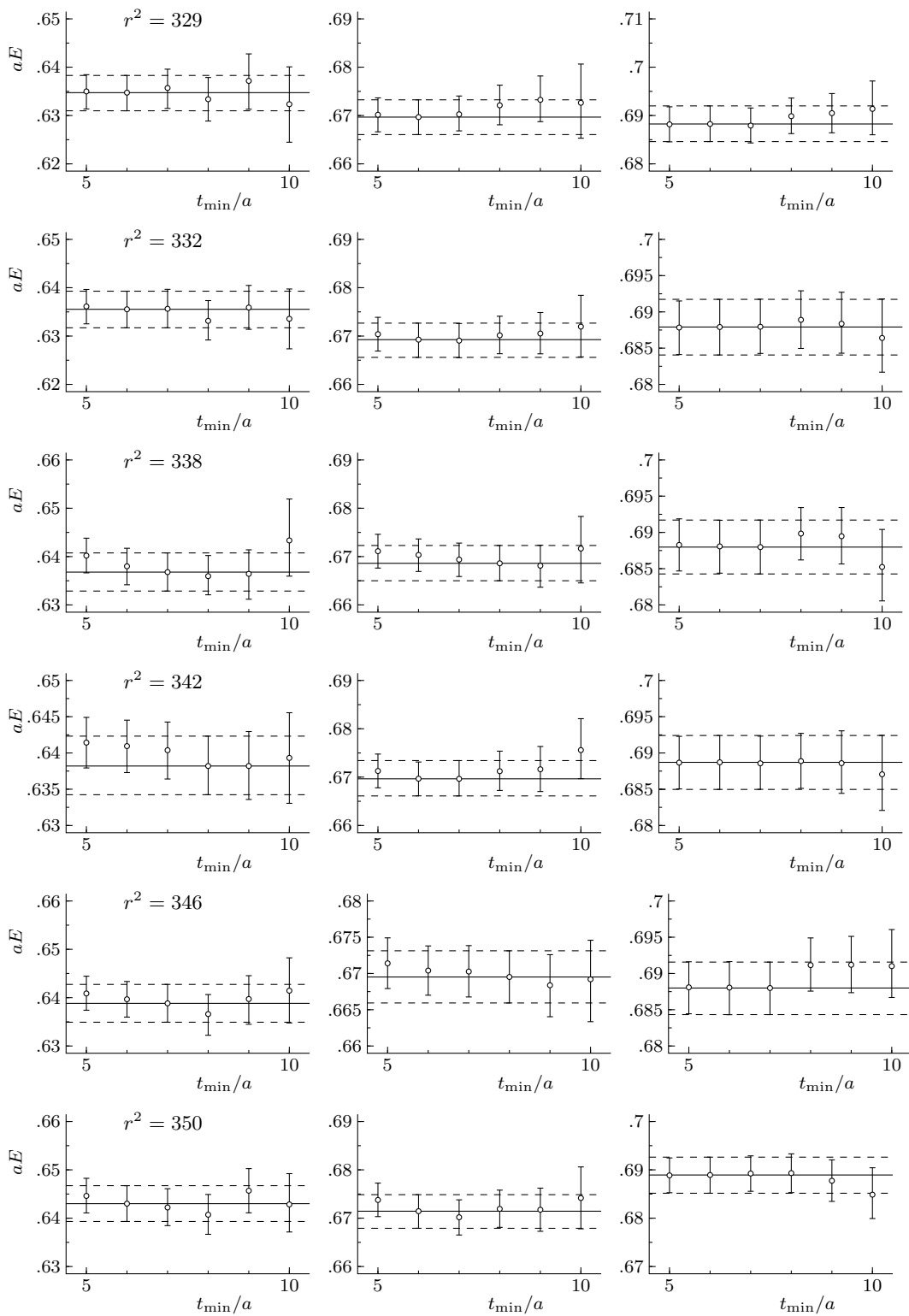


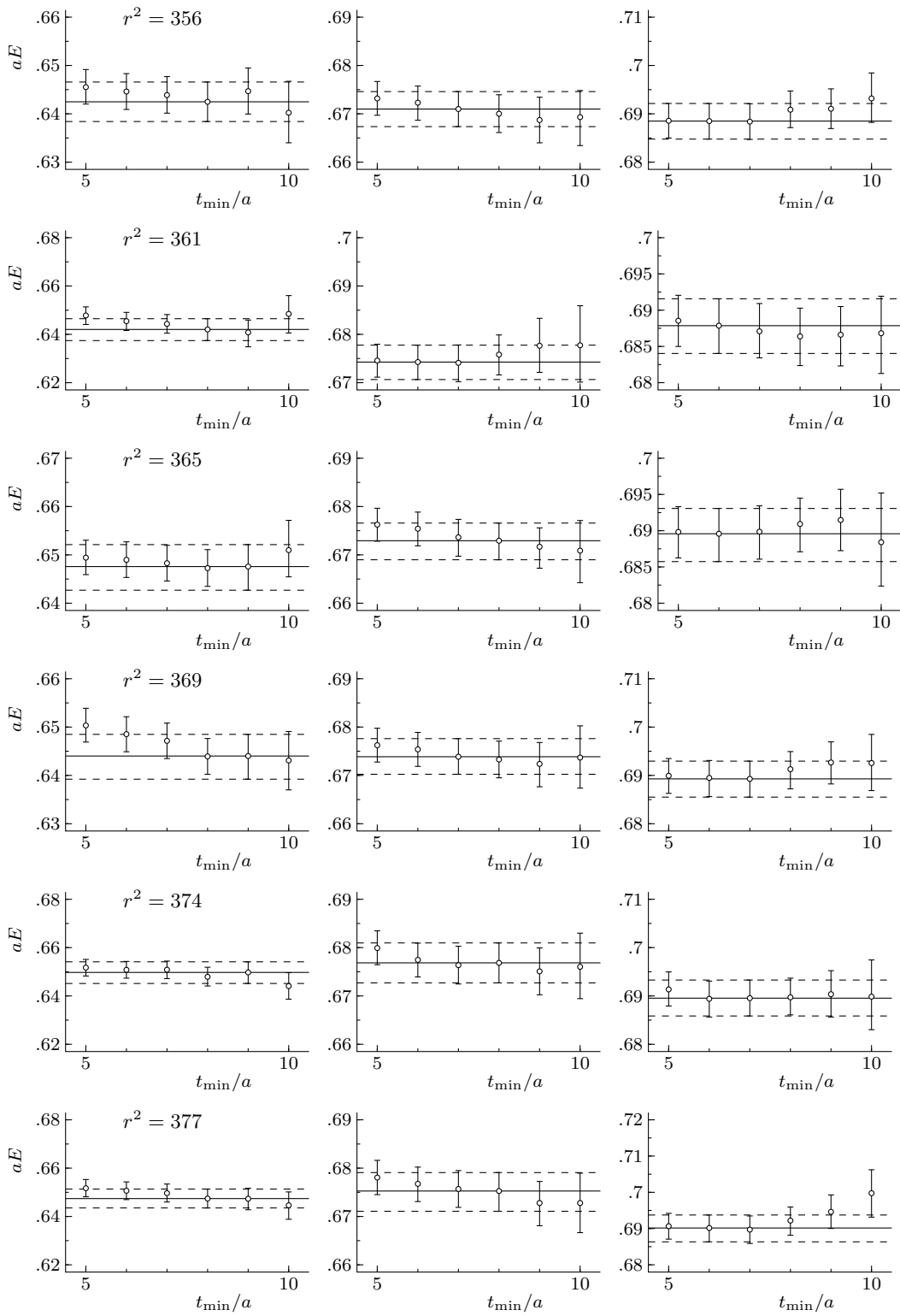


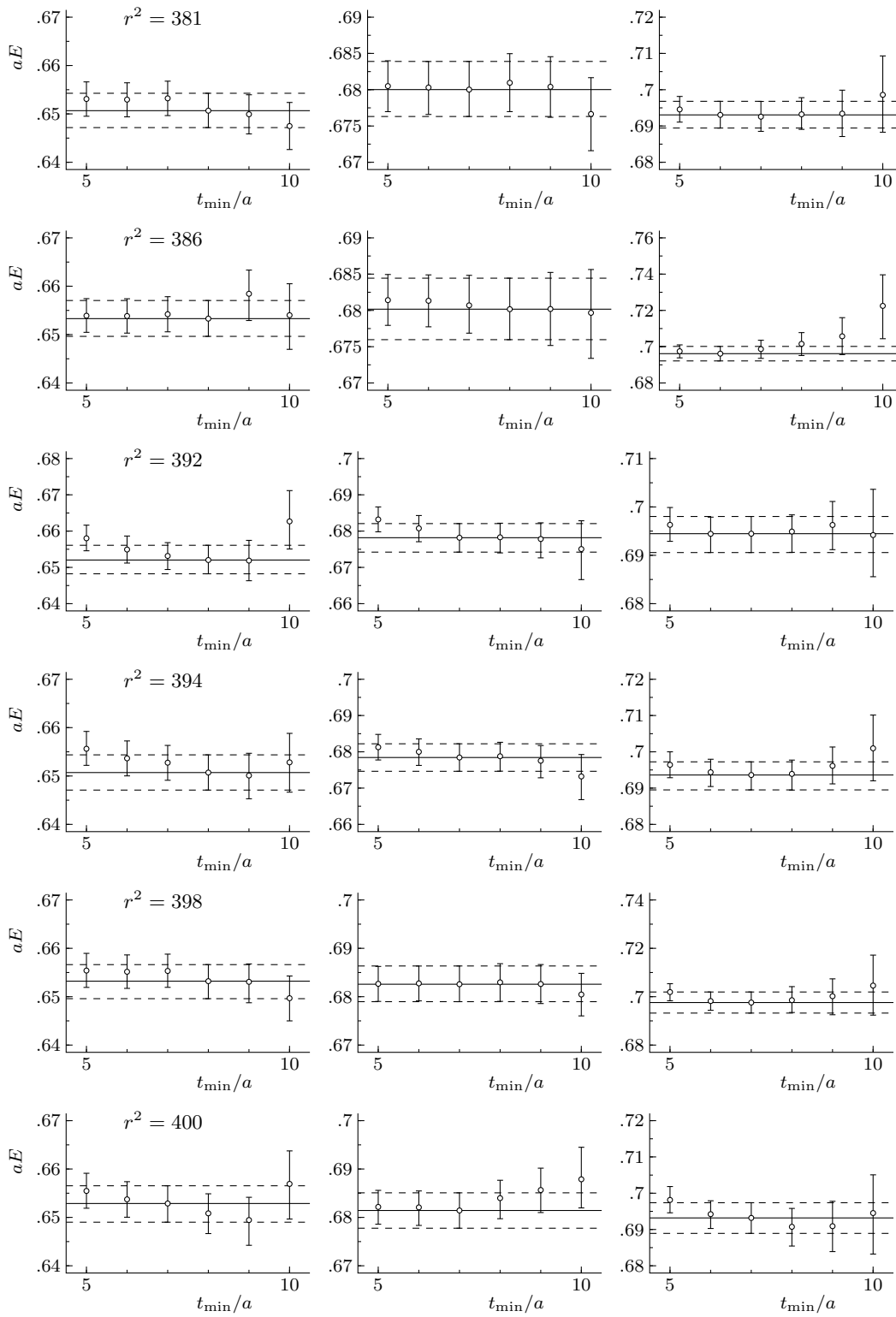


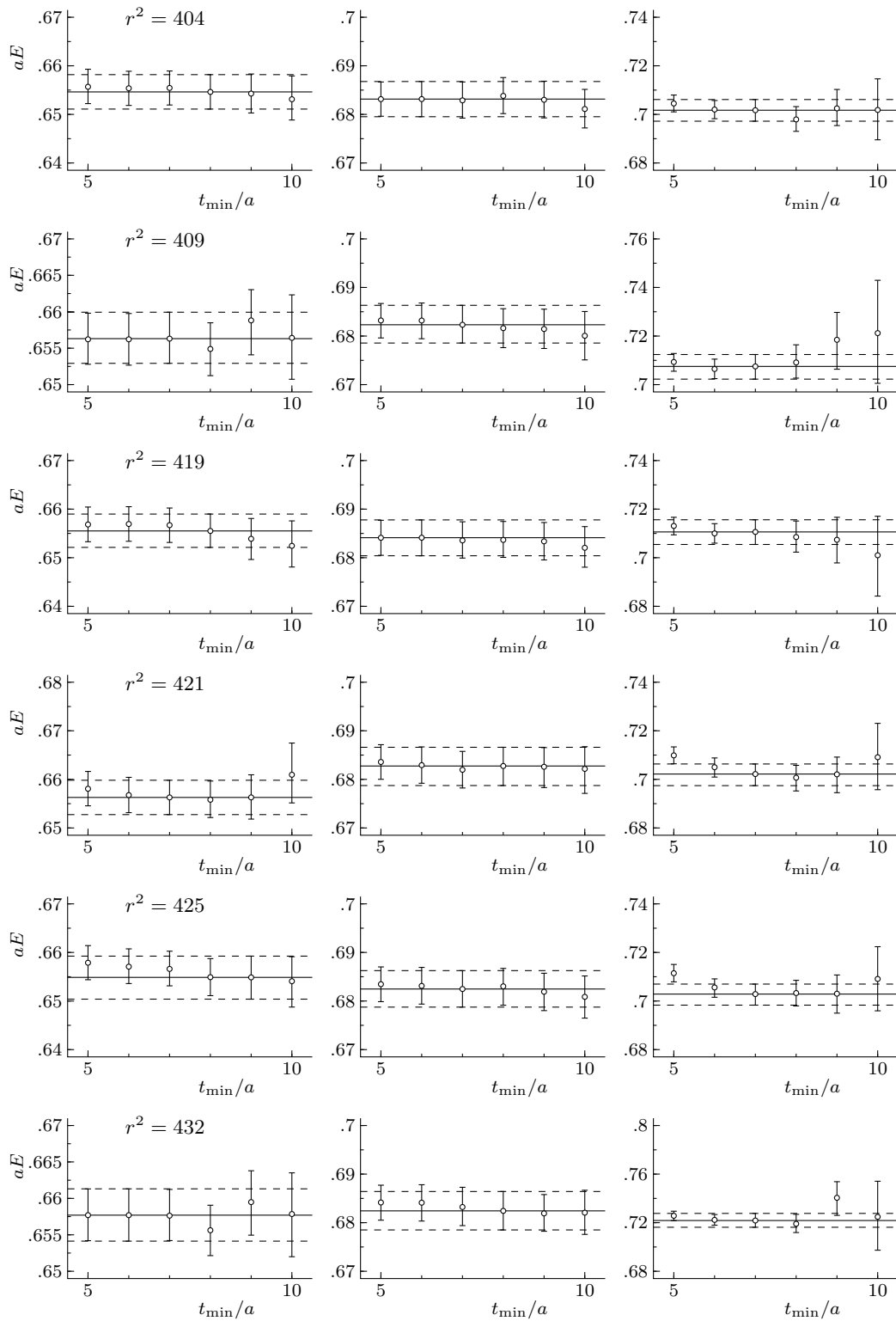


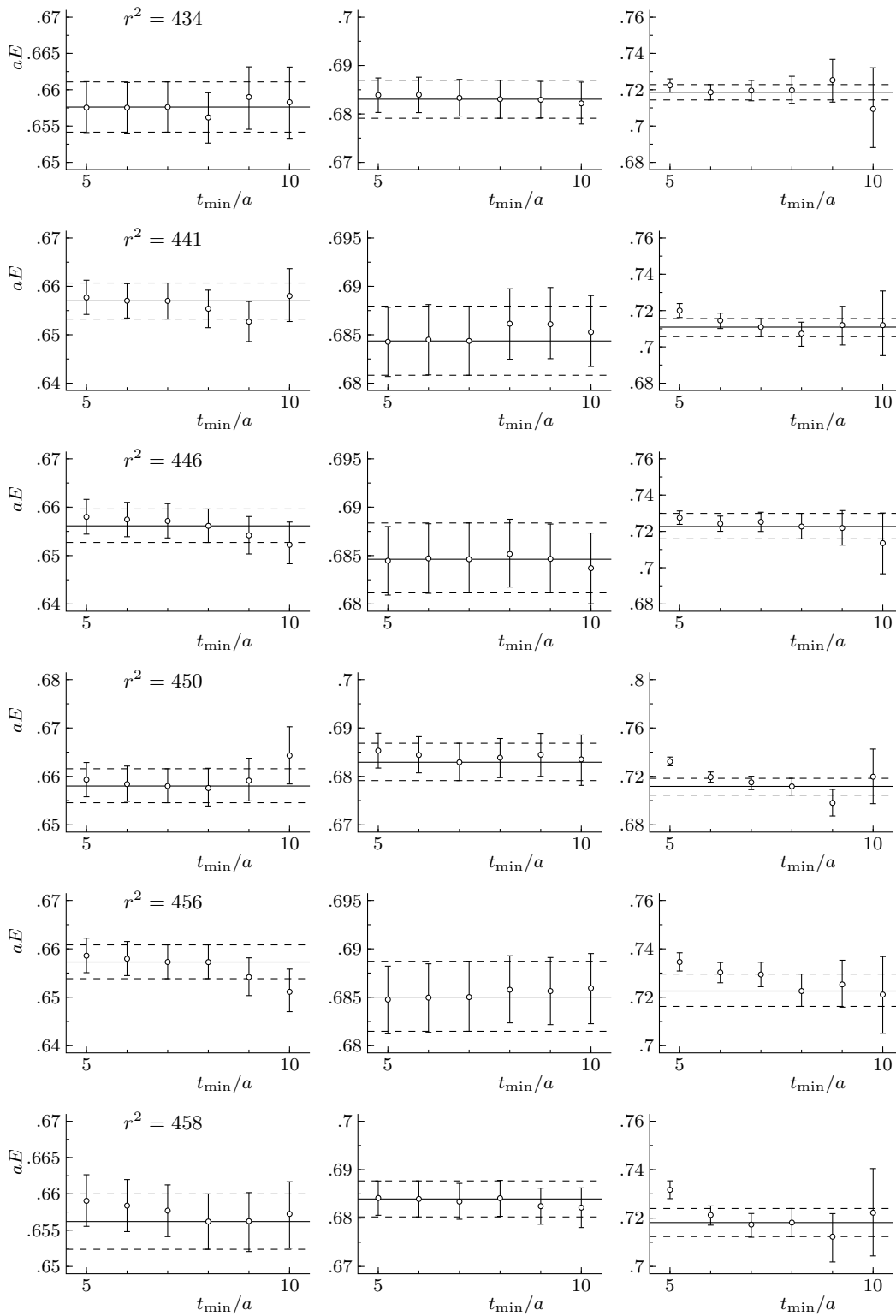


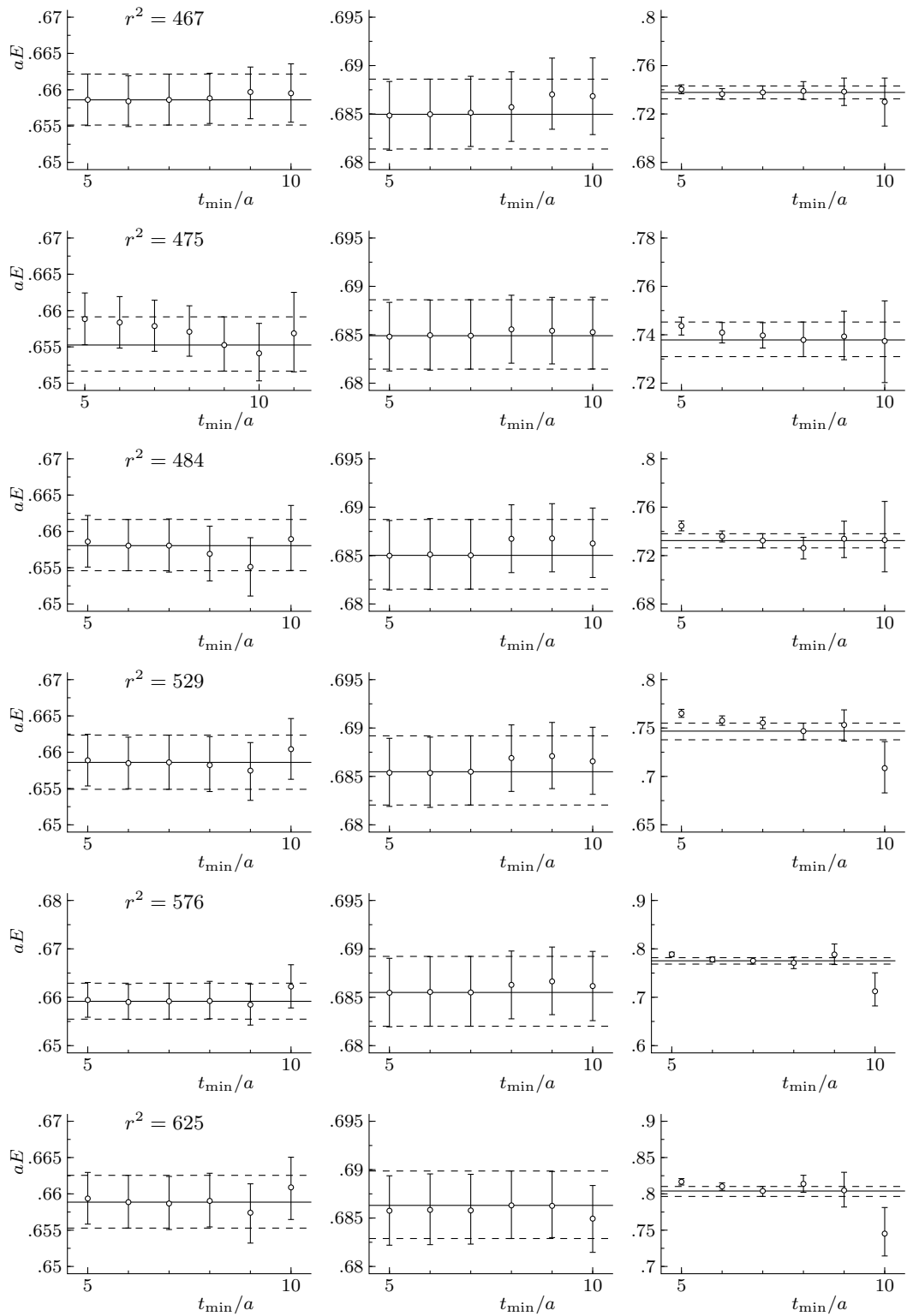
















# Bibliography

- [1] Gerard 't Hooft. The Evolution of Quantum Field Theory, From QED to Grand Unification. 2015.
- [2] David Griffiths. *Introduction to elementary particles*. wiley-VCH, 2008.
- [3] W.N. Cottingham and D.A. Greenwood. *An introduction to the Standard Model of Particle Physics*. Cambridge University Press, 2007.
- [4] K. A. Olive et al. Review of Particle Physics. *Chin. Phys.*, C38:090001, 2014.
- [5] Serguei Chatrchyan et al. Observation of a new boson at a mass of 125 GeV with the CMS experiment at the LHC. *Phys. Lett.*, B716:30–61, 2012.
- [6] Hideo Suganuma, Takahiro M. Doi, Krzysztof Redlich, and Chihiro Sasaki. Relating Quark Confinement and Chiral Symmetry Breaking in QCD. *J. Phys.*, G44:124001, 2017.
- [7] Francesco Giacosa. Modelling glueballs. *EPJ Web Conf.*, 130:01009, 2016.
- [8] C. A. Meyer and E. S. Swanson. Hybrid Mesons. *Prog. Part. Nucl. Phys.*, 82:21–58, 2015.
- [9] Roel Aaij et al. Observation of  $J/\psi p$  Resonances Consistent with Pentaquark States in  $\Lambda_b^0 \rightarrow J/\psi K^- p$  Decays. *Phys. Rev. Lett.*, 115:072001, 2015.
- [10] Roel Aaij et al. Observation of  $J/\psi \phi$  structures consistent with exotic states from amplitude analysis of  $B^+ \rightarrow J/\psi \phi K^+$  decays. 2016.
- [11] J. Greensite. The Confinement problem in lattice gauge theory. *Prog. Part. Nucl. Phys.*, 51:1, 2003.
- [12] Rajan Gupta. Introduction to lattice QCD: Course. In *Probing the standard model of particle interactions. Proceedings, Summer School in Theoretical Physics, NATO Advanced Study Institute, 68th session, Les Houches, France, July 28-September 5, 1997. Pt. 1, 2*, pages 83–219, 1997.
- [13] Zoltan Fodor and Christian Hoelbling. Light Hadron Masses from Lattice QCD. *Rev. Mod. Phys.*, 84:449, 2012.

- [14] Christof Gattringer and Christian B Lang. *Quantum chromodynamics on the lattice: an introductory presentation*. Springer, 2009.
- [15] Francesco Knechtli, Michael Günther, and Michael Peardon. *Lattice Quantum Chromodynamics*. 06 2017.
- [16] S.Schaefer. PoS LATTICE2012. 2012.
- [17] Kenneth G. Wilson. Confinement of quarks. *Phys. Rev. D*, 10:2445–2459, Oct 1974.
- [18] Joseph Polchinski. *String Theory*, volume 1 of *Cambridge Monographs on Mathematical Physics*. Cambridge University Press, 1998.
- [19] Mike Peardon. *Monte Carlo Simulations of Lattice QCD*, pages 41–54. Springer Berlin Heidelberg, Berlin, Heidelberg, 2005.
- [20] Robert G. Edwards, Jozef J. Dudek, David G. Richards, and Stephen J. Wallace. Excited state baryon spectroscopy from lattice QCD. *Phys. Rev.*, D84:074508, 2011.
- [21] Philippe de Forcrand, Wolfgang Unger, and Helvio Vairinhos. Strong-Coupling Lattice QCD on Anisotropic Lattices. *Phys. Rev.*, D97(3):034512, 2018.
- [22] Jeffrey E. Mandula, George Zweig, and Jan Govaerts. Representations of the rotation reflection symmetry group of the four-dimensional cubic lattice. *Nuclear Physics B*, 228(1):91 – 108, 1983.
- [23] H.B. Nielsen and M. Ninomiya. A no-go theorem for regularizing chiral fermions. *Physics Letters B*, 105(2):219 – 223, 1981.
- [24] Mattia Bruno, Dalibor Djukanovic, Georg P. Engel, Anthony Francis, Gregorio Herdoiza, et al. Simulation of QCD with  $N_f=2+1$  flavors of non-perturbatively improved Wilson fermions. 2014.
- [25] John Bulava and Stefan Schaefer. Improvement of  $N_f = 3$  lattice QCD with Wilson fermions and tree-level improved gauge action. *Nucl. Phys.*, B874:188–197, 2013.
- [26] B. Sheikholeslami and R. Wohlert. Improved continuum limit lattice action for qcd with wilson fermions. *Nuclear Physics B*, 259(4):572 – 596, 1985.
- [27] M. Lüscher and P. Weisz. On-shell improved lattice gauge theories. *Comm. Math. Phys.*, 97(1-2):59–77, 1985.
- [28] Martin Lüscher and Stefan Schaefer. Lattice QCD without topology barriers. *JHEP*, 07:036, 2011.

- [29] Simon Duane, A.D. Kennedy, Brian J. Pendleton, and Duncan Roweth. Hybrid monte carlo. *Physics Letters B*, 195(2):216 – 222, 1987.
- [30] Martin Lüscher and Filippo Palombi. Fluctuations and reweighting of the quark determinant on large lattices. *PoS, LATTICE2008:049*, 2008.
- [31] Martin Lüscher and Stefan Schaefer. Lattice QCD with open boundary conditions and twisted-mass reweighting. *Comput. Phys. Commun.*, 184:519–528, 2013.
- [32] M. A. Clark and A. D. Kennedy. Accelerating dynamical fermion computations using the rational hybrid Monte Carlo (RHMC) algorithm with multiple pseudofermion fields. *Phys. Rev. Lett.*, 98:051601, 2007.
- [33] E. I. Zolotarev. *Application of elliptic functions to the questions of functions deviating least and most from zero*. Zap. Imp. Akad. Nauk. St.Petersburg, reprinted in his Collected works, Vol. 2, Akad. Nauk SSSR, Moscow, 1932, p. 1-59, 1877.
- [34] M. Lüscher. Construction of a selfadjoint, strictly positive transfer matrix for euclidean lattice gauge theories. *Comm. Math. Phys.*, 54(3):283–292, 1977.
- [35] K Osterwalder and E Seiler. Gauge field theories on a lattice. *Annals of Physics*, 110(2):440 – 471, 1978.
- [36] S.S. R and K.G. Weston. *Phenomenology And Lattice Qcd - Proceedings Of The 1993 Uehling Summer School*. Proceedings From The Institute For Nuclear Theory. World Scientific Publishing Company, 1995.
- [37] In J.F. Cornwell, editor, *Group Theory in Physics*, Techniques of Physics. Academic Press, San Diego, 1997.
- [38] Sinéad M. Ryan. Lattice Methods for Hadron Spectroscopy. *Lect. Notes Phys.*, 889:35–67, 2015.
- [39] S. Basak, R. G. Edwards, G. T. Fleming, U. M. Heller, C. Morningstar, D. Richards, I. Sato, and S. Wallace. Group-theoretical construction of extended baryon operators in lattice QCD. *Phys. Rev.*, D72:094506, 2005.
- [40] Justina Foley, John Bulava, You-Cyuan Jhang, Keisuke J. Juge, David Lenkner, Colin Morningstar, and Chik Him Wong. Group-theoretical construction of finite-momentum and multi-particle operators for lattice hadron spectroscopy. *PoS, LATTICE2011:120*, 2011.
- [41] David C. Moore and George Tamminga Fleming. Angular momentum on the lattice: The Case of non-zero linear momentum. *Phys. Rev.*, D73:014504, 2006. [Erratum: *Phys. Rev.* D74,079905(2006)].

- [42] Jozef J. Dudek, Robert G. Edwards, Michael J. Peardon, David G. Richards, and Christopher E. Thomas. Toward the excited meson spectrum of dynamical QCD. *Phys. Rev.*, D82:034508, 2010.
- [43] Tommy Burch, Christof Gattringer, Leonid Ya. Glozman, Christian Hagen, C. B. Lang, and Andreas Schafer. Excited hadrons on the lattice: Mesons. *Phys. Rev.*, D73:094505, 2006.
- [44] Jozef J. Dudek, Robert G. Edwards, Michael J. Peardon, David G. Richards, and Christopher E. Thomas. Highly excited and exotic meson spectrum from dynamical lattice QCD. *Phys. Rev. Lett.*, 103:262001, 2009.
- [45] R.C. Johnson. Angular momentum on a lattice. *Physics Letters B*, 114(2):147 – 151, 1982.
- [46] S.Gusken et al. et al. *Phys.Lett.*, B277:266, 1989.
- [47] Subhasish Basak, Ikuro Sato, Stephen Wallace, Robert Edwards, David Richards, et al. Combining quark and link smearing to improve extended baryon operators. *PoS, LAT2005:076*, 2006.
- [48] Colin Morningstar and Mike J. Peardon. Analytic smearing of SU(3) link variables in lattice QCD. *Phys.Rev.*, D69:054501, 2004.
- [49] Anna Hasenfratz and Francesco Knechtli. Flavor symmetry and the static potential with hypercubic blocking. *Phys.Rev.*, D64:034504, 2001.
- [50] M. Albanese, F. Costantini, G. Fiorentini, F. Flore, M.P. Lombardo, R. Tripiccione, P. Bacilieri, L. Fonti, P. Giacomelli, E. Remiddi, M. Bernaschi, N. Cabibbo, E. Marinari, G. Parisi, G. Salina, S. Cabasino, F. Marzano, P. Paolucci, S. Petrarca, F. Rapuano, P. Marchesini, and R. Rusack. Glueball masses and string tension in lattice qcd. *Physics Letters B*, 192(1):163 – 169, 1987.
- [51] A. Hasenfratz, R. Hoffmann, and F. Knechtli. The Static potential with hypercubic blocking. *Nucl.Phys.Proc.Suppl.*, 106:418–420, 2002.
- [52] Michael Peardon et al. A Novel quark-field creation operator construction for hadronic physics in lattice QCD. *Phys.Rev.*, D80:054506, 2009.
- [53] Colin Morningstar, John Bulava, Justin Foley, Keisuke J. Juge, David Lenkner, et al. Improved stochastic estimation of quark propagation with Laplacian Heaviside smearing in lattice QCD. *Phys.Rev.*, D83:114505, 2011.
- [54] Walter Wilcox. Noise methods for flavor singlet quantities. In *Numerical challenges in lattice quantum chromodynamics. Proceedings, Joint Interdisciplinary Workshop, Wuppertal, Germany, August 22-24, 1999*, pages 127–141, 1999.

- [55] Justin Foley, K. Jimmy Juge, Alan O’Cais, Mike Peardon, Sinead M. Ryan, et al. Practical all-to-all propagators for lattice QCD. *Comput.Phys.Commun.*, 172:145–162, 2005.
- [56] Shao-Jing Dong and Keh-Fei Liu. Stochastic estimation with z2 noise. *Physics Letters B*, 328(1):130 – 136, 1994.
- [57] J. Bulava, R. Edwards, K.J. Juge, C.J. Morningstar, and M.J. Peardon. Multi-hadron operators with all-to-all quark propagators. *PoS, LATTICE2008:100*, 2008.
- [58] Martin Lüscher. Computational Strategies in Lattice QCD. In *Modern perspectives in lattice QCD: Quantum field theory and high performance computing. Proceedings, International School, 93rd Session, Les Houches, France, August 3-28, 2009*, pages 331–399, 2010.
- [59] Christopher Michael and A. McKerrell. Fitting correlated hadron mass spectrum data. *Phys. Rev.*, D51:3745–3750, 1995.
- [60] Christopher Michael. Fitting correlated data. *Phys. Rev.*, D49:2616–2619, 1994.
- [61] P. De Groen and B. De Moor. The fit of a sum of exponentials to noisy data. *Journal of Computational and Applied Mathematics*, 20:175 – 187, 1987.
- [62] W.J. Wiscombe and J.W. Evans. Exponential-sum fitting of radiative transmission functions. *Journal of Computational Physics*, 24(4):416 – 444, 1977.
- [63] Benoit Blossier, Michele Della Morte, Georg von Hippel, Tereza Mendes, and Rainer Sommer. On the generalized eigenvalue method for energies and matrix elements in lattice field theory. *JHEP*, 0904:094, 2009.
- [64] B. Blossier, G. von Hippel, T. Mendes, R. Sommer, and M. Della Morte. Efficient use of the Generalized Eigenvalue Problem. *PoS, LATTICE2008:135*, 2008.
- [65] Martin Lüscher and Ulli Wolff. How to calculate the elastic scattering matrix in two-dimensional quantum field theories by numerical simulation. *Nuclear Physics B*, 339(1):222 – 252, 1990.
- [66] Francesco Knechtli and Rainer Sommer. String breaking as a mixing phenomenon in the SU(2) Higgs model. *Nucl.Phys.*, B590:309–328, 2000.
- [67] Francesco Knechtli and Rainer Sommer. String breaking in SU(2) gauge theory with scalar matter fields. *Phys.Lett.*, B440:345–352, 1998.
- [68] Bootstrap methods: Another look at the jackknife. *The Annals of Statistics*, 7(1):1–26, 1979.

- [69] Bradley Efron and Rob Tibshirani. Bootstrap methods for standard errors, confidence intervals, and other measures of statistical accuracy. 1, 02 1986.
- [70] Christian Andersen, John Bulava, Ben Hörz, and Colin Morningstar. The  $I = 1$  pion-pion scattering amplitude and timelike pion form factor from  $N_f = 2 + 1$  lattice QCD. 2018.
- [71] E. Eichten, K. Gottfried, T. Kinoshita, J. Kogut, K. D. Lane, and T. M. Yan. Spectrum of charmed quark-antiquark bound states. *Phys. Rev. Lett.*, 34:369–372, Feb 1975.
- [72] U. Glassner et al. First evidence of  $N(f)$  dependence in the QCD interquark potential. *Phys.Lett.*, B383:98–104, 1996.
- [73] Urs M. Heller, Khalil M. Bitar, R. G. Edwards, and A. D. Kennedy. The Heavy quark potential in QCD with two flavors of dynamical quarks. *Phys. Lett.*, B335:71–76, 1994.
- [74] I.T. Drummond. Strong coupling model for string breaking on the lattice. *Phys.Lett.*, B434:92–98, 1998.
- [75] Owe Philipsen and Hartmut Wittig. String breaking in nonAbelian gauge theories with fundamental matter fields. *Phys.Rev.Lett.*, 81:4056–4059, 1998.
- [76] Gunnar S. Bali, Hartmut Neff, Thomas Duessel, Thomas Lippert, and Klaus Schilling. Observation of string breaking in QCD. *Phys.Rev.*, D71:114513, 2005.
- [77] Jochen Heitger and Rainer Sommer. Nonperturbative heavy quark effective theory. *JHEP*, 02:022, 2004.
- [78] Rainer Sommer. Introduction to Non-perturbative Heavy Quark Effective Theory. In *Modern perspectives in lattice QCD: Quantum field theory and high performance computing. Proceedings, International School, 93rd Session, Les Houches, France, August 3-28, 2009*, pages 517–590, 2010.
- [79] Estia Eichten and Brian Russell Hill. An Effective Field Theory for the Calculation of Matrix Elements Involving Heavy Quarks. *Phys.Lett.*, B234:511, 1990.
- [80] Michele Della Morte, Andrea Shindler, and Rainer Sommer. On lattice actions for static quarks. *JHEP*, 0508:051, 2005.
- [81] Piotr Korcyl, Christoph Lehner, and Tomomi Ishikawa. Non-perturbative renormalization of the static quark theory in a large volume. *PoS, LATTICE2015:254*, 2016.
- [82] G. Martinelli and Christopher T. Sachrajda. Renormalons and the heavy quark effective theory. *Phys. Lett.*, B354:423–434, 1995.

- [83] Silvia Necco and Rainer Sommer. The  $N(f) = 0$  heavy quark potential from short to intermediate distances. *Nucl. Phys.*, B622:328–346, 2002.
- [84] Martin Kurth and Rainer Sommer. Renormalization and  $O(a)$  improvement of the static axial current. *Nucl. Phys.*, B597:488–518, 2001.
- [85] Marc Wagner. Forces between static-light mesons. *PoS, LATTICE2010*:162, 2010.
- [86] Gunnar Bali and Martin Hetzenegger. Static-light meson-meson potentials. *PoS, LATTICE2010*:142, 2010.
- [87] Karl Jansen, Chris Michael, Andrea Shindler, and Marc Wagner. The Static-light meson spectrum from twisted mass lattice QCD. *JHEP*, 0812:058, 2008.
- [88] Gunnar S. Bali. The  $D^+(s)(2317)$ : What can the lattice say? *Phys. Rev.*, D68:071501, 2003.
- [89] Mattia Bruno, Tomasz Korzec, and Stefan Schaefer. Setting the scale for the CLS 2 + 1 flavor ensembles. *Phys. Rev.*, D95(7):074504, 2017.
- [90] Martin Lüscher and Stefan Schaefer. Lattice QCD with open boundary conditions and twisted-mass reweighting. *Comput. Phys. Commun.*, 184:519–528, 2013.
- [91] Ben Hörz. *Pion-pion scattering amplitudes and the timelike pion form factor from  $N_f = 2 + 1$  Lattice QCD*. PhD thesis, Trinity College Dublin, 2017.
- [92] Martin Lüscher. Solution of the Dirac equation in lattice QCD using a domain decomposition method. *Comput. Phys. Commun.*, 156:209–220, 2004.
- [93] Martin Lüscher. Local coherence and deflation of the low quark modes in lattice QCD. *JHEP*, 07:081, 2007.
- [94] Andreas Frommer, Karsten Kahl, Stefan Krieg, Björn Leder, and Matthias Rottmann. Adaptive Aggregation Based Domain Decomposition Multigrid for the Lattice Wilson Dirac Operator. *SIAM J. Sci. Comput.*, 36:A1581–A1608, 2014.
- [95] Robert G. Edwards and Balint Joo. The Chroma software system for lattice QCD. *Nucl. Phys. Proc. Suppl.*, 140:832, 2005. [832(2004)].
- [96] Vanessa Koch, John Bulava, Ben Hörz, Francesco Knechtli, Graham Moir, Colin Morningstar, and Mike Peardon. Towards string breaking with 2+1 dynamical fermions using the stochastic LapH method. *PoS, LATTICE2015*:100, 2016.
- [97] Michael Donnellan, Francesco Knechtli, Björn Leder, and Rainer Sommer. Determination of the Static Potential with Dynamical Fermions. *Nucl. Phys.*, B849:45–63, 2011.

- [98] Frederic D. R. Bonnet, Derek B. Leinweber, Anthony G. Williams, and James M. Zanotti. Towards string breaking in the static quark potential. *Submitted to: Phys. Rev. D*, 1999.
- [99] J.D. Foley et al. *Computer graphics: Principles and practice*. 1996.
- [100] Bram Bolder, Thorsten Struckmann, Gunnar S. Bali, Norbert Eicker, Thomas Lippert, Boris Orth, Klaus Schilling, and Peer Ueberholz. A High precision study of the Q anti-Q potential from Wilson loops in the regime of string breaking. *Phys. Rev.*, D63:074504, 2001.
- [101] Charles-Alban Deledalle, Loic Denis, Sonia Tabti, and Florence Tupin. Closed-form expressions of the eigen decomposition of  $2 \times 2$  and  $3 \times 3$  Hermitian matrices. Research report, Université de Lyon, 2017.
- [102] John Bulava, Ben Hörz, and Colin Morningstar. Multi-hadron spectroscopy in a large physical volume. *EPJ Web Conf.*, 175:05026, 2018.